

UNIVERSITÉ DU QUÉBEC À MONTRÉAL

ÉTUDE DU CLIMAT DE L'AFRIQUE DE L'OUEST PAR UNE APPROCHE
D'ÉNERGÉTIQUE DE L'ATMOSPHÈRE

THÈSE
PRÉSENTÉE
COMME EXIGENCE PARTIELLE
DU DOCTORAT EN SCIENCES DE LA TERRE ET DE L'ATMOSPHÈRE

PAR
YVES FRANKLIN NGUÉTO

DÉCEMBRE 2023

UNIVERSITÉ DU QUÉBEC À MONTRÉAL
Service des bibliothèques

Avertissement

La diffusion de cette thèse se fait dans le respect des droits de son auteur, qui a signé le formulaire *Autorisation de reproduire et de diffuser un travail de recherche de cycles supérieurs* (SDU-522 – Rév.04-2020). Cette autorisation stipule que «conformément à l'article 11 du Règlement no 8 des études de cycles supérieurs, [l'auteur] concède à l'Université du Québec à Montréal une licence non exclusive d'utilisation et de publication de la totalité ou d'une partie importante de [son] travail de recherche pour des fins pédagogiques et non commerciales. Plus précisément, [l'auteur] autorise l'Université du Québec à Montréal à reproduire, diffuser, prêter, distribuer ou vendre des copies de [son] travail de recherche à des fins non commerciales sur quelque support que ce soit, y compris l'Internet. Cette licence et cette autorisation n'entraînent pas une renonciation de [la] part [de l'auteur] à [ses] droits moraux ni à [ses] droits de propriété intellectuelle. Sauf entente contraire, [l'auteur] conserve la liberté de diffuser et de commercialiser ou non ce travail dont [il] possède un exemplaire.»

REMERCIEMENTS

Je tiens à dire un merci particulier à mon directeur de thèse, René Laprise qui m'a donné toutes les clés nécessaires pour mener à bien ce projet. Par sa pédagogie, il m'a tout d'abord permis de prendre le temps de maîtriser les grandes avancées faites par mes prédecesseurs du département sur le sujet, avant de m'accompagner plus tard dans le développement de mes propres théories. Son style d'encadrement qui me faisait me sentir à la fois libre d'explorer beaucoup de pistes et en même temps balisé vers les objectifs de ma thèse, me procurait un grand sentiment de sécurité durant toute cette thèse.

Je remercie également mon co-directeur Oumarou Nikiéma, pour m'avoir donné tous les outils techniques dans la prise en main du projet, ce qui m'a permis de gagner un temps considérable.

Je souligne également ma grande reconnaissance à tout le personnel du département qui travaillent en arrière pour que nous puissions être dans les meilleures conditions, à tous ses collègues pour la collaboration et l'esprit d'équipe.

Je ne peux finir sans dire un merci particulier à ma chère et tendre épouse, Nadège Madjoukouo, la mère de mes merveilleux garçons, pour son amour inconditionnel et l'équilibre qu'elle a apporté dans ma vie; à ma maman, mon défunt papa et mes frères qui ont toujours cru en moi.

Merci.

DÉDICACE

À Dieu, par qui et pour qui je suis.

TABLE DES MATIÈRES

REMERCIEMENTS	ii
DÉDICACE.....	iii
LISTE DES FIGURES	vii
LISTE DES ABRÉVIATIONS, DES SIGLES ET DES ACRONYMES	xi
RÉSUMÉ.....	xiii
ABSTRACT.....	xvi
INTRODUCTION.....	1
CHAPITRE 1 A detailed limited-area energy cycle for climate and weather studies: application over the West African climate during three summers 1997 (dry), 1999 (wet) and 2006 (normal)	22
1.1 Introduction.....	23
1.2 Methodology for the computation of an atmospheric energy cycle suitable for both climate and weather studies	25
1.2.1 Decomposition rule of quadratic quantities	26
1.2.2 Energy equations.....	28
1.2.3 Energy budget equations for climate studies	29
1.2.4 Energy budget equations for transient eddies studies	33
1.2.5 Verification of energy budget equations for climate and storms studies	36
1.2.5.1 Total kinetic energy equation retrieval.....	37
1.2.5.2 Total enthalpy energy equation retrieval.....	38
1.2.6 Summary of the climate energy budget	39
1.2.7 Summary of storms energy budget	39
1.3 MODEL CONFIGURATION	40
1.3.1 Simulation condition and domain	40
1.3.2 West African climate overview.....	41
1.4 APPLICATION OF THE CLIMATE CYCLE THE WEST AFRICAN MONSOON	44
1.4.1 Energy reservoirs	46
1.4.2 Energy generation and dissipation terms	51
1.4.3 Boundaries fluxes terms	53
1.4.4 Vertical profiles.....	53
1.5 SUMMARY AND CONCLUSIONS	55
1.6 Appendix.....	58
1.6.1 Appendix A1: Kinetic energy equation.....	58
1.6.2 Appendix A2: Alternative decompositions of quadratic terms	59
1.6.3 Appendix A3: Effective thermodynamics equation	61

1.6.4 Appendix A4: Time-mean kinetic energy equation associated with time-mean wind ...	64
1.6.5 Appendix A5: Time-mean kinetic energy associated with time-variability of the wind	66
1.6.6 Appendix A6: Time-mean available enthalpy equation associated with time-mean temperature	68
1.6.7 Appendix A7: Time-mean available enthalpy equation associated with time-variability of temperature.....	69
1.6.8 Appendix A8: Instantaneous kinetic energy equation associated with variance of wind fluctuations	71
1.6.9 Appendix A9: Instantaneous kinetic energy equation associated with covariance of wind fluctuations and wind time-average.....	73
1.6.10 Appendix A10: Instantaneous available enthalpy associated with variance of temperature fluctuations	75
1.6.11 Appendix A11: Instantaneous available enthalpy associated with covariance of temperature fluctuations and wind time-average	77
1.6.12 Appendix A12: Total kinetic energy retrieval	80
1.6.13 Appendix A13: Total kinetic energy retrieval	82
1.6.14 Appendix A14: Link between C_E and C_A 's vertical component.....	84
 CHAPITRE 2 Energetic study of an African wave simulated by the CRCM6 using regional transient-eddy budget equations.....	103
2.1 Introduction.....	103
2.2 Methodology.....	105
2.2.1 Detection of African Easterly Waves.....	105
2.2.2 Choice of the wave.....	108
2.2.3 Presence of the wave in the reanalysis dataset ERA5	109
2.2.4 Transient-eddy energy cycle equations	109
2.2.5 Wave energy budget computation and representation	111
2.2.6 Energy reservoirs	112
2.2.7 Conversion terms	114
2.2.8 Generation, dissipation and boundary flux terms	116
2.3 Summary and Conclusion.....	117
2.4 Appendix.....	120
2.4.1 Appendix B1: Link between c_a 's vertical component and c_{x1a}	120
 CONCLUSION	136
1. Rappel de l'objectif et de l'approche empruntée	136
2. Principaux résultats de la recherche empruntée	137
3. Limitations et nouvelles pistes de recherche.....	139
4. Retombées scientifiques et mot de fin.....	140
 ANNEXE A Résultats complémentaire de l'introduction	142
ANNEXE B Matériel supplémentaire du chapitre 1	143

ANNEXE C Matériel supplémentaire du chapitre 2	145
BIBLIOGRAPHIE	146

LISTE DES FIGURES

Figure 0-1: Évolution temporelle de la moyenne journalière de la température en surface dans le Golfe de Guinée et le Sahara (pour deux mailles choisies au hasard) du 1er Avril au 30 Juin 2009, à l'aide des réanalyses ERA5.....	14
Figure 0-2: Coupe tri-dimensionnelle de la WAM, Source : (Lafore <i>et al.</i> , 2011).....	15
Figure 0-3: Gradient méridien de température sur le flanc Nord de l'Afrique à 600 hPa (figure du dessus) et à 950 hPa (figure en-dessous) moyennés de Juin à Septembre 2009. L'unité est le Kelvin/m.....	16
Figure 0-4: Profil vertical de la température pour deux points choisis au hasard dans le Golfe de Guinée (en bleu) et le Sahara (en rouge) moyennés entre les mois de Juillet et Septembre 2009. Le niveau de L'AEJ est indiqué par la flèche noir.....	17
Figure 0-5: Coupe verticale de q_y entre 20°W et 30°E, moyennée de Juillet à Septembre 2009 en K.m/Kg/s entre les latitudes 0 et 30°N.	18
Figure 0-6: Profils horizontaux des gradients de température potentielle (à la surface i.e 950 hPa , en °K/m) (a) et de tourbillon potentiel (au niveau du Jet, en K.m/Kg/s) (b).....	19
Figure 1-1: Climate energy cycle. Boxes represent the different energy reservoirs and arrows the various sources/sinks of energy acting on them.....	85
Figure 1-2: Storm energy cycle. Boxes represent the different energy reservoirs and arrows the various sources/sinks of energy acting on them.....	86
Figure 1-3: Free domain excluding, 10 grid-point-wide semi-Lagrangian halo and 10 grid-point-wide lateral Davies' sponge zone, contains 620*340 grid points. The red band delimits our main West Africa study domain [20°W–20°E; 0–20°N].....	87
Figure 1-4: Mean (May to September) precipitation for 1997 (dry year), 1999 (humid year) and 2006 (normal year) from CRCM6, ERA5, CRU and UDEL in mm/day.....	88
Figure 1-5: May to September mean surface temperature (colors, in °C) and mean sea level pressure (white contour, in hPa) for 1997 (dry year), 1999 (humid year) and 2006 (normal year) from ERA5, CRCM6, CRU and UDEL.....	89
Figure 1-6: Vertical latitude cross-section of May to September averaged vertical velocity, negative (positive) values are upward (downward) motion (colors, in Pa/s) and relative humidity (black contour, in %) averaged in the longitude 10°W - 10°E, from CRCM6 (top) and ERA5 (bottom).	90
Figure 1-7: Vertical latitude cross-section of May to September averaged zonal wind (colors, in m/s), averaged in the longitude 10°W - 10°E, from CRCM6 (top) and ERA5 (bottom).	91

Figure 1-8: Vertical latitude cross-section of May to September averaged meridional wind (colors, in m/s), averaged in the longitude 10°W - 10°E, from CRCM6 (top) and ERA5 (bottom) ...	92
Figure 1-9: Vertically integrated time- and domain-averaged climate energy cycle for 1997 (dry-year, blue values, up), 1999 (wet-year, red values, middle) and 2006 (normal-year, black values, down). Energy reservoirs (boxes) are shown in 10^5 Jm^{-2} and energy fluxes (arrows) in W.m^{-2}	93
Figure 1-10: Vertical latitude cross-section of a) A_M (divided by 50 for uniformity), b) A_E , c) K_E and d) K_M averaged in the longitude 10°W – 10°E. Values are in J.kg^{-1}	94
Figure 1-11: Maps of vertically integrated of a) A_M (divided by 20 for uniformity), b) A_E , c) K_E and d) K_M . Values are in 10^5 J.m^{-2}	95
Figure 1-12: Vertical latitude cross-section of a) C_A , b) C_{EA} , c) C_{EK} , d) C_K , e) C_{MK} and f) C_{MA} (divided by 200 for uniformity) averaged in the longitude 10°W – 10°E. Values are in $10^{-4} \text{ W.kg}^{-1}$	96
Figure 1-13: Maps of vertically integrated conversion of a) C_A , b) C_{EA} , c) C_{EK} , d) C_K e) C_{MK} and f) C_{MA} (divided by 200 for uniformity) . Values are in W.m^{-2}	97
Figure 1-14: Vertical cross-section of a) G_M (divided by 10 for uniformity), b) G_E , c) D_E and d) D_M , averaged in the region between 10°W – 10°E and 10°S – 25°N. Values are in $10^{-4} \text{ W.kg}^{-1}$	98
Figure 1-15: Maps of vertically integrated a) G_M , b) G_E , c) D_E and d) D_M . Values are in W.m^{-2} .	99
Figure 1-16: Vertical latitude cross-section of a) convection contribution, b) condensation contribution, c) radiation contribution, d) vertical diffusion contribution and e) total diabatic heating rate averaged in the longitude 10°W – 10°E. Values are in K.day^{-1}	100
Figure 1-17: Maps of vertically integrated a) convection contribution, b) condensation contribution, c) radiation contribution and d) vertical diffusion contribution and e) total diabatic heating rate. Values are in K/day	101
Figure 1-18: Vertical profiles of time- and study domain (20°W–20°E; 0–20°N)-averaged fluxes acting on energy reservoirs of a) A_M , b) A_E , c) K_M and d) K_E , values are in 10^{-3} W/Kg	102
Figure 2-1: Hovmöller diagram of a) meridional wind (m.s^{-1}) and b) relative vorticity (10^6 s^{-1}) at 700 hPa, for three contrasting years 1997-dry, 1999-humid and 2006-normal, from the CRCM6.	121
Figure 2-2: a) Hovmoller diagram of AX1 and b) vertically integrated (from 950 to 200 hPa) maps for a single date of the eight most important AEWs observed, in 10^4 J.m^2 , with superimposed 700 hPa filtered winds during the dry year (1997)	122

Figure 2-3: a) Hovmoller diagram of AX1 and b) vertically integrated (from 950 to 200 hPa) maps for a single date of the eight most important AEWs observed, in 10^4 J.m^2 , with superimposed 700 hPa filtered winds during the wet year (1999)	123
Figure 2-4: a) Hovmoller diagram of AX1 and b) vertically integrated (from 950 to 200 hPa) maps for a single date of the eight most important AEWs observed, in 10^4 J.m^2 , with superimposed 700 hPa filtered winds during the normal year (2006).	124
Figure 2-5: Transient eddy kinetic energy vertically (950-200 hPa) and horizontally (over south Sudan, represented to the right) averaged in J.m^2	125
Figure 2-6: a) Hovmoller diagram of AX1 during the normal year (2006) in 10^4 J.m^2 and b) AX1 vertically integrated (from 950 to 200 hPa) and averaged over the southern Sudan in J.m^2 , using ERA5	126
Figure 2-7: Maps of filtered vertically integrated instantaneous fields of three consecutive days of a) $kx1$ (with 700 hPa filtered winds as background, m.s^{-1}) and b) $ax1$ (with 850 hPa filtered temperature vertical arrows as background, $^\circ\text{K}$), in 10^5 J/m^2	127
Figure 2-8: Vertically integrated (from 950 to 200 hPa) time- and domain-averaged storm energy cycle. Values are computed for the duration of the storm (September 05 to 10, 2006 and the units are in 10^{-3} W.m^{-2})	128
Figure 2-9: Time series of vertically integrated (from 950 to 200 hPa), a) domain-averaged and b) standard deviations terms of the energy budget in 10^4 W.m^{-2}	129
Figure 2-10 : Vertical longitude cross-section of instantaneous a) $kx1$ and b) $ax1$, averaged in the latitude $5^\circ\text{N}-15^\circ\text{N}$. The abscissa is the longitude in degrees and the ordinate is the pressure in hPa. Values are energy in J.Kg^{-1}	130
Figure 2-11:Maps of grid points time series correlation between different 3D components and the total a) ca , b) ck and c) $f\varphi x1$. Values are computed from September 05 to 15, 2006.....	131
Figure 2-12: Maps of instantaneous vertically integrated (from 950 to 200 hPa) energy fluxes of a) ca , b) $cx1a$, c) $cx1k$ and d) ck . Values are in W.Kg^{-1} with 700 hPa filtered horizontal wind (arrow, m.s^{-1}) as background.....	132
Figure 2-13: Vertical longitude cross-section of instantaneous a) ca , b) $cx1a$, c) $cx1k$ and d) ck averaged in the latitude $5^\circ\text{N}-15^\circ\text{N}$. The abscissa is the longitude in degrees and the ordinate is the pressure in hPa. Values are energy in 10^4 W.Kg^{-1}	133
Figure 2-14: Maps of instantaneous vertically integrated (from 950 to 200 hPa) energy fluxes of a) $gx1$, b) $dx1$ and c) $f\varphi x1$. Values are in W.m^{-2} with 700 hPa filtered horizontal wind (arrow, m.s^{-1}) as background.....	134
Figure 2-15: Vertical longitude cross-section of instantaneous a) $gx1$, b) $dx1$ and c) $f\varphi x1$. averaged in the latitude $5^\circ\text{N}-15^\circ\text{N}$. The abscissa is the longitude in degrees and the ordinate is the pressure in hPa. Values are in 10^4 W.Kg^{-1}	135

LISTE DES ABRÉVIATIONS, DES SIGLES ET DES ACRONYMES

Liste française :	
<i>AO</i>	<i>Afrique de l'Ouest</i>
<i>ESKER</i>	<i>Centre pour l'Étude et la Simulation du Climat à l'Échelle Régionale</i>
<i>MRCC6</i>	<i>Modèle Régional Canadien de Climat de 6^{ème} génération</i>
Liste anglaise :	
AE	Time-Variability Available Enthalpy
AEJ	African Easterly Jet
AEWs	African Easterly Waves
ALMIP	Amma Land Surface Model Intercomparison Project
AM	Time-Mean Available Enthalpy Energy
AMMA	African Monsoon Multidisciplinary Analysis
AMMA-MIP	African Monsoon Multidisciplinary Analysis – Model Intercomparaison Model
APE	Available Potential Energy
AX1	Tropical Easterly Jet
AZ	Zonal-Mean Available Enthalpy
CA	Conversion of Time-Mean into Time-Variability Available Enthalpy
CEA	Flux of Available Enthalpy offered for Conversion into Kinetic Energy
CEK	Fraction of Available Enthalpy convertible into Kinetic Energy
CGCM	Coupled Global Climate Model
CK	Conversion flux between time-mean and time-variability Kinetic Energy
CMA	Conversion of time-mean available enthalpy into Kinetic Energy
CMK	Energy Flux affecting the time-mean Kinetic Energy from Available Enthalpy
CRCM6	Sixth-generation of the Canadian Regional Climate Model
CX1A	Conversion of AX1 towards baroclinic production of KX1
CX1K	Fraction of cx1a convertible into transient-eddy Kinetic Energy
DE	Dissipation of time-variability Kinetic Energy
DM	Dissipation of time-mean Kinetic Energy
DX1	Dissipation of transient-eddy Kinetic Energy
ECMWF	European Centre for Medium Range Weather Forecasting
ERA5	Fifth generation ECMWF atmospheric reanalysis of the global climate
FAE	Flux of time-variability Available Enthalpy
FAM	Flux of time-mean Available Enthalpy

FAX1	Flux of transient-eddy Available Enthalpy
FKE	Flux of time-variability Kinetic Energy
FKM	Flux of time-mean Kinetic Energy
FKX1	Flux of transient-eddy Kinetic Energy
F ϕ E	Flux of time-variability Geopotential Heights
F ϕ M	Flux of time-mean Geopotential Heights
F ϕ X1	Flux of transient-eddy Geopotential Heights
GCM	General Circulation Models
GE	Generation of time-variability diabatic heating
GM	Generation of time-mean diabatic heating
GX1	Instantaneous generation of transient-eddy Available Enthalpy
IFS	Integrated Forecasting System
ITCZ	Intertropical Convergence Zone
ITD	Inter Tropical Discontinuity
ITF	Intertropical Front
JA	Available Enthalpy third order term
JK	Kinetic Energy third order term
KE	Time-variability Kinetic Energy
KEn	Kinetic Energy
KM	Time-mean Kinetic Energy
KX1	Transient-eddy Kinetic Energy
KZ	Zonal-mean Kinetic Energy
LLAT	Low Level Atmospheric Thickness
MCS	Mesoscale Convective System
MSC	Meteorological Service of Canada
NL13	Nikiema And Laprise (2013)
NWP	Numerical Weather Prediction
RCM	Regional Climate Model
RDPS	Regional Dynamical Prediction System
SHL	Saharian Heat Low
SST	Sea Surface Temperature
TEJ	Tropical Easterly Jet
TPE	Total Potential Energy
UPE	Unavailable Potential Energy
WAHL	West African Heat Low
WAM	West African Monsoon
WAMME	West African Monsoon Modeling and Evaluation

RÉSUMÉ

L'objectif de cette thèse est d'utiliser une approche de bilan énergétique de l'atmosphère pour comprendre le régime de précipitations et les systèmes météorologiques associés en Afrique de l'Ouest, à l'aide de la version 6 du Modèle Régional Canadien de Climat (MRCC6). Le modèle est piloté aux frontières par la 5^{ème} génération des réanalyses (ERA5) du Centre Européen pour les Prévisions Météorologiques à Moyen Terme. Le bilan d'énergie est un ensemble d'équations garantissant la conservation de la masse, de l'énergie et du moment angulaire. De plus, chaque terme du bilan d'énergie représente un processus physique, ce qui permet de quantifier la contribution relative de chacun de ces derniers et de savoir quel est le processus responsable de la génération / l'amplification / l'amortissement d'un phénomène météorologique ou climatique. Les calculs du bilan d'énergie ne sont en effet qu'une quantification sur une période et un domaine donné de tous les termes en présence. L'enjeu principal dans cette étude étant la formulation d'un bilan d'énergie régional complet qui comprend à fois des termes moyennés dans le temps (pour l'étude du climat) et des termes non moyennés disponibles à chaque pas de temps (pour l'étude de la météo), nous avons développé un ensemble complet d'équations répondant à ces deux problématiques. Suivra l'application de ce bilan sur le domaine de l'Afrique de l'Ouest qui connaît des saisons de moussons africaines contrastées en terme pluviométrie; la pluie étant un enjeu majeur pour ces populations vivant en grande partie de l'agriculture.

Le premier chapitre développe le cadre théorique de notre étude. Dans ce chapitre, nous partons des équations primitives atmosphériques pour établir les termes / processus responsables de variation de l'énergie, de la masse et de la quantité de mouvement dans notre domaine d'étude. La validation théorique de ces différentes équations est faite en sommant toutes les différentes contributions et en retombant sur les équations de départ. Ceci est la preuve qu'aucune pièce d'information n'a été oubliée et que les différentes lois de conservations initiales demeurent. Dans la suite de ce chapitre, on passe de la théorie à la pratique en appliquant les équations moyennées temporellement pour étudier le climat de l'Afrique de l'Ouest. Depuis le début des années 80, on note une grande variabilité dans la pluviométrie dans cette région du monde. Pour comprendre les raisons physiques de cette variabilité, nous avons tout d'abord à l'aide des réanalyses ERA5 classifiés les étés 1980 à 2010 en fonction de leur pluviométrie moyenne.

Ensuite, nous avons appliqué notre bilan d'énergie de climat à l'année la moins pluvieuse, la plus pluvieuse et celle la plus proche de la climatologie sur les 30 années. Les résultats suggèrent que les conversions d'énergies barotropes et baroclines qui constituent les processus de génération des ondes africaines sont plus importantes durant les années humides que les années sèches. Nous suggérons donc au terme de ce premier chapitre, le suivi de ces deux conversions d'énergie pour prévoir le climat en Afrique de l'Ouest.

Le dernier chapitre de cette thèse s'inscrit dans la continuité du premier et s'intéresse au bilan d'énergie d'un épisode important de tempête, qui a duré 5 jours et a été détecté durant une des années contrastantes. Afin de trouver l'épisode le plus important, nous avons développé notre propre méthode d'identification de tous les épisodes durant chacune de ses années. Cette méthode consiste à utiliser le diagramme de Hovmöller d'un de nos réservoirs d'énergie du bilan d'énergie des tempêtes. Ce nouveau diagramme possède à la fois les avantages des diagrammes de Hovmöller des vents méridiens et de tourbillon relatif jusqu'ici utilisés dans la littérature pour détecter les Ondes d'Est Africaines. Cette méthode nous a permis de choisir un épisode intense entre le 5 et le 10 septembre 2006. De plus, cet épisode coïncide avec une onde trouvée dans la littérature comme un cyclone tropical associé avec la genèse de l'ouragan Alberto. Une fois l'épisode choisi, nous avons appliqué une partie du bilan d'énergie de la météo sur cette même période pour étudier l'évolution des différents processus. Les résultats montrent que les conversions baroclines sont largement dominantes par rapport aux conversions barotropes lors des épisodes importants et constituent la principale source de génération des Ondes d'Est Africaines.

Cette thèse a permis de présenter une approche détaillée et complète permettant l'étude des bilans d'énergie pour le climat et les tempêtes sur des domaines régionaux. Par rapport aux bilans d'énergie du climat que l'on retrouve dans la littérature, nous avons innové en rajoutant des nœuds entre les réservoirs d'enthalpie disponible et d'énergie cinétique. Ces nœuds ont l'avantage d'expliquer pourquoi toute l'enthalpie disponible à l'échelle régionale n'est pas complètement convertible en énergie cinétique comme c'est le cas à l'échelle globale. L'application du bilan d'énergie du climat sur le domaine Afrique de l'ouest confirme que le mécanisme d'instabilité mixte barotrope barocline est à l'origine des ondes d'Est africaines, que les gradients de température et d'humidité sont des sources d'instabilités baroclines, et met en évidence que les

réservoirs d'énergie de variabilité temporelle sont plus importants les années pluvieuses. Nous recommandons d'ailleurs fortement l'analyse de ces deux derniers réservoirs d'énergie pour les études sur le climat de l'Afrique de l'ouest. De plus, l'application du bilan d'énergie des perturbations transitoires sur le même domaine nous a permis de ressortir une variable plus adaptée pour la détection des ondes d'Est africaines, et de montrer la prééminence de l'instabilité barocline sur la composante barotrope pour le développement d'intenses ondes d'Est africaines.

Mots-clés : modèle régional de climat, bilan d'énergie, Afrique de l'Ouest, climat, météo, ondes d'Est Africaines.

ABSTRACT

The objective of this thesis is to use an atmospheric energy budget approach to understand the West African monsoon variability, using the 6th version of the Canadian Regional Climate Model (CRCM6). The model is driven at the lateral boundaries by the 5th generation of reanalyses (ERA5) of the European Centre for Medium-Range Weather Forecasts. The energy balance is a set of equations ensuring the conservation of mass, energy and angular momentum. Moreover, each term of the energy budget represents a physical process, and their possible computation at each time step, will allow us to detect processes responsible of the generation / amplification / dampening of the weather or the climate. The computation of the energy budget could be seen as the quantification over a period and a given domain of sources and sinks terms. The main issue in this thesis being the formulation of a complete regional energy budget including both time-average (for the study of the climate) and instantaneous terms available at each time step (for the study of the weather), we have developed a full set of atmospheric energetics equations to address these two issues. This report will then be applied to the West African domain, which experiences contrasting African monsoon seasons in terms of rainfall, rain being a major issue for these populations living mostly from agriculture.

The first chapter develops the theoretical framework of our study. In this chapter, we start from the primitive atmospheric equations to establish the terms / processes responsible for the variation of heat, mass and momentum in our study domain. The theoretical validation of these different equations is made by summing all the different contributions to come back to the former primitive equations. This proves that no piece of information has been forgotten and that the various conservation laws remain valid. In the second part of this chapter, we move from theory to practice by applying the time-averaged equations to study the West African climate. Since the beginning of the 1980s, there has been a great variability in rainfall in this region of the world. To understand the physical reasons for this variability, we first classified the summers of 1980 to 2010 according to their average rainfall using ERA5 reanalyses. Then, we applied our climate energy balance to the least rainy year, the雨iest year and the one closest to the climatology. The results suggest that barotropic and baroclinic energy conversions, which constitute processes generating African waves, are more important in wet years than in dry years. We therefore

suggest at the end of this study, the monitoring of these two energy conversions to predict the West African climate.

The last chapter of this thesis is an extension of the first and focuses on the energy budget of a major storm observed during one of the former contrasting years. In order to find the most important storm, we developed a method to identify all storms during each year. This method consists of using the Hovmöller diagram of one term of our storm energy budget. This new diagram has both the advantages of the Hovmöller diagrams for both meridional winds and relative vorticity generally used in the literature to detect African Easterly waves. This method allowed us to choose an intense case between September 5th and 10th 2006. Moreover, this storm coincides with a wave found in the literature as a tropical cyclone associated with the genesis of Hurricane Alberto. Once the storm chosen, we applied a portion of the energy budget equations of the weather to follow the evolution of different processes. The results show that baroclinic conversions are largely dominant compared to barotropic conversions during storms and constitute the main source of generation of East African waves.

This thesis allowed us to present a complete and detailed approach for climate and weather studies at the regional scale. Compared to other climate energy budget, we added a node between available enthalpy and kinetic energy reservoirs. These nodes have the advantage to explain why all the available enthalpy is not convertible into kinetic energy as this is the case at the global scale. Using the climate energy budget on west Africa confirm that African easterly waves arise through a mixed barotropic/baroclinic instability mechanism, that temperature and humidity gradients feed the baroclinic instability, and that time-variability climate energy reservoirs are more important during rainy years. We highly recommend the analysis of these transient-energy reservoir for west African climate studies. Moreover, applying the transient-eddy energy cycle on the same domain revealed a new variable suitable for African easterly waves detection, and showed the dominance of the baroclinic instability over the barotropic during the development of intense African waves.

Key-Words: regional climate model, energy budget, West Africa, climate, weather, African Easterly waves.

INTRODUCTION

L'étude du climat courant en Afrique de l'Ouest (AO) constitue un défi étant donné l'absence d'un réseau de données d'observations dense. Les modèles numériques ont également de la difficulté à capturer la variabilité spatiale et temporelle de la mousson d'Afrique de l'Ouest (WAM, West African Monsoon en anglais) (Cook et Vizy, 2006). Une des raisons de cette lacune est la complexité et la diversité des processus en jeu durant la WAM (Hernández-Díaz *et al.*, 2013). De plus, les températures de surface de la mer (SST, *Sea Surface Temperature* en anglais) simulées à l'aide des modèles globaux couplés atmosphère-océan (CGCM, *Coupled Global Climate Model* en anglais) nécessaires pour effectuer des projections de changements climatiques ont des grands biais (Taylor *et al.*, 2012), ce qui contribue à réduire le degré de confiance des projections effectuées. L'étude de (Hernández-Díaz *et al.*, 2017) a récemment permis d'améliorer l'habileté du Modèle Régional Canadien du Climat (MRCC) à reproduire les caractéristiques principales de la WAM en utilisant une technique de correction récurrente des biais de SST en amont. Ces améliorations nous permettent de disposer de simulations à hautes résolutions et de meilleure qualité pour nos études climatiques. De plus, l'approche énergétique qui va constituer notre principal outil méthodologique a déjà été testée avec succès sur des simulations du MRCC5 grâce aux travaux de (Nikiéma et Laprise, 2013) et (Clément *et al.*, 2017).

Aperçu du climat de l'Afrique de l'Ouest

Contrairement aux quatre saisons observées au cours de l'année dans les latitudes moyennes, la zone tropicale de l'Afrique de l'ouest comprend deux principales saisons: une pluvieuse et une sèche. C'est pour cette raison que la précipitation est généralement considérée comme le principal indice climatique dans cette région avec la température. Durant l'été boréal, on observe une importante pluviométrie associée à la mousson d'Afrique de l'Ouest (WAM, *West African Monsoon*, en anglais), qui est une des principales caractéristiques du climat de cette région. De façon simplifiée, le WAM peut être décrite comme une grande brise entre les masses d'eau relativement froides du Golfe de Guinée et l'air chaud au-dessus du continent Africain durant l'été boréal (Lafore *et al.*, 2011). C'est surtout l'important apport en humidité lié à la migration vers le nord des alizées du secteur Sud à partir du printemps boréal, qui est à l'origine de ces

quantités importantes de précipitations observées. Dès lors, des processus dynamiques, qui résultent d'interactions complexes entre différentes composantes de la WAM, s'enclenchent (Lafore *et al.*, 2011).

La Fig. 0-1 montre l'évolution temporelle de la moyenne journalière de la température en surface dans ces deux lieux du 1^{er} avril au 30 juin 2009 à l'aide de la réanalyses ERA5. Elle suggère que l'élément déclencheur dans la WAM est le gradient de température entre le golfe de Guinée et le Sahara. En effet, on note que le gradient de température entre les deux régions augmente relativement de manière graduelle pour atteindre un premier maximum autour du 18 mai (noté 1), puis il baisse légèrement jusqu'au milieu du mois de juin, avant de reprendre sa croissance et atteindre un second maximum autour du 24 juin (noté 2).

Cette situation observée est caractéristique des phases de déclenchement de la WAM. En effet, la dynamique des précipitations près du golfe de Guinée suit deux phases distinctes (Sultan et Janicot, 2000, 2003; Sultan *et al.*, 2003) :

La première est la *présaison* (*pre-onset* en anglais) qui se déclenche lorsque la zone de convergence intertropicale (ITCZ, *Intertropical Convergence Zone* en anglais) s'établit autour de 5° N (autour du 14 mai).

La seconde qui est la principale « *saison des pluies* » (*onset* en anglais) qui est effective lorsque la ITCZ quitte 5° N pour migrer de manière abrupte vers le nord (autour du 24 juin) en atteignant une latitude maximale de 10° N pendant le mois d'août (Laux *et al.*, 2008).

On distingue aisément ces deux phases sur la Fig. 0-1 en cherchant les maxima des écarts de température entre les deux régions vers le 20 mai (numéro 1) et le 24 juin (numéro 2 sur la figure).

Selon (Lafore *et al.*, 2011), la WAM est dominée par cinq composantes principales (Fig. 0-2) : le courant jet d'Est Africain (AEJ, *African Easterly Jet* en anglais), les ondes d'Est Africaines (AEWs, *African Easterly Waves* en anglais), le courant jet d'Est Tropical d'altitude (TEJ, *Tropical Easterly Jet* en anglais), le front intertropical (ITD, *Inter Tropical Discontinuity* en anglais), la dépression saharienne (SHL, *Saharian Heat Low* en anglais), et la bande de

précipitation. Il est important de comprendre la variabilité de ces processus physiques associés à la WAM pour pouvoir la prévoir afin de permettre aux décideurs des pays concernés de mettre en place des stratégies d’adaptation dans une perspective de changements climatiques :

- L'**AEJ** est un courant jet de bas niveau se propageant vers l’Ouest. Son altitude moyenne est comprise entre 600 et 700 hPa, avec des vents d’Est de maximum 15 m/s (Kuo, 1998). Nous avons recensé dans la littérature, trois principales théories sur l’origine de ce courant jet qui n’est observé que durant l’été boréal.
- D’après l’étude de (Burpee, 1972) : Une des particularités du Sahel est la variation brutale de température méridienne en surface. La Fig. 0-3 présente le gradient méridien de température moyen temporellement du 1^{er} juillet au 30 septembre 2009 près de la surface (950 hPa) et près de la moyenne troposphère (600 hPa) à l’aide des données de réanalyse. On observe que le gradient de température méridien près de la surface est relativement faible au sud du Sahel (à cause de l’influence modérée de l’océan Atlantique) et sur le Sahara (à cause de la présence du désert et de l’absence de sources d’humidité en surface). Par contre, sur le Sahel, on observe une zone barocline dont la réponse sur la structure verticale de l’atmosphère est la production d’un vent d’Est maximal près de 600 hPa. En effet, le vent thermique u_T (qui représente le cisaillement vertical subi par le vent entre la base p_1 et le sommet p_2 de la couche barocline) est proportionnel à l’épaisseur de la couche et au gradient horizontal de température T :

$$u_T = -\frac{R}{f} \cdot \frac{\partial \bar{T}}{\partial y} \ln\left(\frac{p_1}{p_2}\right) \quad (0-1)$$

en supposant un équilibre géostrophique. R et f représentent respectivement la constante spécifique des gaz parfaits pour l’air sec et le paramètre de Coriolis. En Afrique de l’Ouest, la variation méridienne de température devient faible au-dessus de 600 hPa, ce qui limite la

couche barocline entre la surface et 600 hPa. On devrait donc avoir un vent d'Est (vers l'Ouest) maximal autour de 600 hPa.

- D'après l'étude de (Cook, 1999) : Le gradient de température positif en surface lui seul ne peut expliquer l'existence du courant jet de bas niveau. (Cook, 1999) a permis de réaliser un ensemble de simulations avec différentes conditions initiales dans le but de localiser la (ou les) caractéristique(s) de surface responsable(s) de la présence de l'AEJ à l'aide d'un modèle global. Les résultats ont montré que des différences dans les conditions en surface sur la mer et sur la terre influencent la position et/ou l'intensité de l'AEJ dans des proportions relativement modestes. Cependant, pour que le modèle global utilisé lors de ces simulations capture la présence de l'AEJ, il nécessite des gradients réalistes de température de surface et d'humidité du sol. En effet, sans un gradient méridien négatif d'humidité du sol, le gradient méridien de température de surface serait toujours positif, mais pas assez fort pour produire le mouvement vers l'Est des vents au-dessus des vents d'Ouest de mousson en surface.
- D'après l'étude de (Thorncroft, CD et Blackburn, 1999): En considérant les températures de surface et les gradients d'humidités en été boréal, on s'aperçoit que les masses d'air sur le Sahel suivent un profil vertical selon une adiabatique sèche tandis que les masses d'air sur le golfe de Guinée suivent plutôt un profil selon une pseudo-adiabatique mouillée. Or, comme nous l'avons observé sur la Fig. 0-3, le gradient méridien de température positif de surface diminue en altitude pour s'annuler au niveau du jet et changer de signe au-dessus de ce niveau. Le niveau du courant jet africain correspond au niveau où l'équilibre est rétabli en altitude (en principe, les températures les plus froides sont en direction du pôle et les plus chaudes en direction de l'équateur). C'est la raison pour laquelle la cellule thermique allant de la surface jusqu'au niveau de l'AEJ est appelée cellule de renversement méridienne (meridional overturning cell en anglais). La Fig. 0-4 montre les profils verticaux de température moyennée temporellement (de juin à septembre 2009) de deux points choisis au hasard dans le golfe de Guinée et dans le Sahara et se trouvant à la même longitude (comme dans le cas de Fig. 0-1). La Fig. A 1 (voir le matériel supplémentaire), nous rapportons les données de la réanalyse de nos deux mailles choisies précédemment sur un téphigramme. En effet, en dessous du niveau du jet, le profil vertical de température suit le profil de la pseudo-adiabatique dans le golfe et celui de l'adiabatique sèche dans le Sahel. Les deux profils se

croisent au niveau de l'AEJ (~ 610 hPa) et poursuivent un même profil dans l'atmosphère libre à cause du rétablissement de l'équilibre thermique.

En résumé, les trois études sur l'origine de l'AEJ convergent vers la même théorie selon laquelle l'AEJ est une réponse à la forte baroclinicité en surface sur le Sahel. Le gradient d'humidité négatif suggéré par (Cook, 1999) n'est que la conséquence des conditions en surface au Sahara et dans le Golfe. De plus, l'étude de (Thorncroft, CD et Blackburn, 1999) contenait déjà des éléments se trouvant dans (Burpee, 1972), car ce dernier affirmait déjà que « *le maximum de l'AEJ apparaît au niveau de pression où le gradient méridien de température positif de surface est remplacé par le gradient négatif en atmosphère libre* » (traduction libre).

- **Les AEWs :** Ce sont des ondes qui expriment l'instabilité hydrodynamique du courant jet de bas niveau sur le continent. Avant de regarder l'effet de ses ondes sur la WAM, il faudrait tout d'abord s'assurer que l'atmosphère étudiée est favorable à leur développement. D'après le critère de stabilité hydrodynamique de Charney-Stern, pour qu'un écoulement soit instable, il faut que soit le gradient du tourbillon potentiel quasi-géostrophique :

$$q_y = \frac{\partial}{\partial y} \left[\left(\left(\frac{\partial v}{\partial x} \right)_\theta - \left(\frac{\partial u}{\partial y} \right)_\theta + f \right) g \frac{\partial \theta}{\partial p} \right] \quad (0-2)$$

sur un niveau de pression constant *change de signe à l'intérieur du fluide* (a) ou *ait un signe opposé au gradient de température potentielle en surface* (b) (Thorncroft, CD et Hoskins, 1994a). Dans cette équation, u et v sont les vents horizontaux, g l'accélération gravitationnelle et p la pression. Nous avons vérifié à l'aide de la réanalyse que l'atmosphère de l'Afrique de l'Ouest satisfaisait ces conditions.

- **Hypothèse (a) - Changement de signe de q_y à l'intérieur du fluide :** La Fig. 0-5 montre la coupe verticale de q_y entre les longitudes 20°W et 30°E , moyennés de juin à septembre 2009. Les valeurs les plus faibles (négatives) de q_y se trouvent au cœur du courant jet. Au nord du cœur du courant jet (au-delà de 10°N), les valeurs deviennent positives. Il en est de même sur le flanc sud (au sud de 10°N). La frontière entre les valeurs positives et négatives (en blanc)

circonscrit les zones géographiques où l'atmosphère est la plus instable et par conséquent la plus propice au développement des AEWs.

- **Hypothèse (b) - Signes de q_y (au niveau du jet) et de θ_y (en surface) opposés :** La Fig. 0-6 montre la distribution horizontale de \bar{q}_y (à 700 hPa) et de $\bar{\theta}_y$ (à 950 hPa, près de la surface).

On observe effectivement que les valeurs des gradients de température potentielle en surface et de tourbillon potentiel (au niveau de l'AEJ) sont de signes opposés. Les deux critères d'instabilités de Charney-Stern étant vérifiés, on peut conclure que l'atmosphère de l'Afrique de l'ouest est favorable au développement des ondes d'Est Africaines durant l'été boréal. Dans les années 1970s, la vérification de ces critères d'instabilité sur les données d'observation de l'AEJ de (Burpee, 1972; Reed *et al.*, 1977), a abouti à un consensus selon lequel les ondes d'Est Africaines se développent à cause du mécanisme d'instabilité mixte barotrope-barocline (Thorncroft, C. D. *et al.*, 2008). Ce consensus a été renforcé par des simulations idéalisées démontrant que l'on pourrait voir se développer des ondes d'Est réalisables à partir de faibles variations d'amplitudes de l'AEJ (Paradis *et al.*, 1995; Rennick, 1976; Simmons, 1977; Thorncroft, CD et Hoskins, 1994a, 1994b).

De manière générale, les ondes d'Est Africaines sont les principales perturbations d'échelles synoptiques se développant le long de l'AEJ et sont fortement couplées à la convection. Elles sont souvent séparées en deux groupes dont le premier a une période de 3 à 5 jours et le second une période comprise entre 6 et 9 jours (Diedhiou, Arona *et al.*, 1998). Les AEWs constituent le mode de variabilité dominant en AO et jouent un rôle dans la formation des cyclones tropicaux. Près de 85% des ouragans intenses (ou majeurs) sur l'Atlantique tropical ont pour origine les ondes d'Est Africaines et il est suggéré que presque tous les cyclones tropicaux qui se produisent dans l'océan Pacifique oriental ont également pour origine ces ondes Africaines (Avila et Pasch, 1995).

- **La dépression Saharienne :** La dépression saharienne a été identifiée comme une des composantes majeures de la WAM (Lavaysse *et al.*, 2009; Parker, D. *et al.*, 2005; Peyrillé *et al.*, 2007; Sultan *et al.*, 2003) et comme un moteur de la précipitation sur le Sahel (Evan *et al.*, 2015; Lavaysse *et al.*, 2010). Elle est caractérisée par un minimum de pression et un maximum de température au-dessus du Sahara. D'un point de vue dynamique, la dépression saharienne est une réponse thermique de la basse troposphère au réchauffement saisonnier en

surface au-dessus du Sahara, là où les températures de surface sont les plus élevées. Le minimum de pression en surface et les températures les plus élevées qui y sont associées apparaissent durant l'après-midi, lorsque la couche limite planétaire est profonde et bien mélangée (Lavaysse *et al.*, 2009). La dépression saharienne n'est pas toujours facile à détecter. (Knippertz et Fink, 2008) a relevé qu'elle prend souvent la forme d'une élongation zonale plutôt que celle circulaire, dépendamment de la saison. (Lavaysse *et al.*, 2009) a permis de mettre point une méthode robuste pour détecter sa position au cours des saisons. Elle est basée sur l'analyse d'une variable appelée épaisseur atmosphérique dans les basses couches (LLAT, *Low Level Atmospheric Thickness*), définie comme la différence des hauteurs géopotentielles à 700 et 925 hPa respectivement. Ils montrent que la dépression Saharienne n'existe qu'en été et que durant cette saison elle n'est que le résultat de la migration saisonnière de la dépression thermique d'Afrique de l'Ouest (WAHL, *West African Heat Low*). En d'autres termes la WAHL change de position au cours des saisons et est appelée SHL durant l'été boréal en Afrique de l'ouest. Dans la troposphère moyenne par exemple, la circulation anticyclonique associée avec l'écoulement divergent au-dessus de la dépression saharienne contribue à maintenir le courant jet de bas niveau (AEJ) et module son intensité (Thorncroft, CD et Blackburn, 1999). À l'échelle intra saisonnière, les variations de la dépression saharienne en particulier et de la WAM en général sont associées à la propagation vers l'Ouest des AEWs, contribuant ainsi à une augmentation de l'activité convective sur le Sahel (Lavaysse *et al.*, 2010). (Evan *et al.*, 2015) ont trouvé une corrélation positive entre les précipitations dans le Sahel et les températures de surface sur le Sahara. Ils ont également démontré que le retour des précipitations sur le Sahara (après la sécheresse des années 70-80) est lié à une intensification de la dépression saharienne (SHL, *Sahara Heat Low* en anglais). Malgré la connaissance de ces interactions entre la SHL et les autres branches de la WAM, il manque toujours dans la littérature une étude détaillée du lien entre la dépression Saharienne et la WAM à l'échelle régionale (Lavaysse *et al.*, 2009). Les outils de l'énergétique atmosphérique sur des domaines à aire limitée devraient permettre de rendre cette étude possible.

- ***Le front intertropical*** : D'un point de vue dynamique, on définit le front intertropical comme le lieu de rencontre des masses d'air chaudes et sèches provenant du Nord du Sahara (entrainées par l'Harmattan) et des masses maritimes en provenance du golfe de Guinée

(entrainées par les vents de mousson en surface). En pratique, le front intertropical (ITD, Intertropical Discontinuity en anglais) se détecte par une approche thermodynamique. Celle-ci consiste à rechercher les points proches de la surface où la température du point de rosée est égale à 14°C (Roberts *et al.*, 2015) ou 15°C (Olaniyan *et al.*, 2015). L'ITD est une région de fortes activités convectives et par conséquent favorise la production des systèmes convectifs méso-échelles (MCS, *Mesoscale Convective System* en anglais). Ces derniers sont particulièrement importants au Sahel parce qu'ils apportent approximativement 80% des précipitations (Mohr *et al.*, 1999). La détection de l'ITD est donc un enjeu si l'on veut comprendre la distribution spatio-temporelle des précipitations sur l'Ouest de l'Afrique durant la saison de mousson.

- ***Le courant jet d'Est tropical*** : Le courant jet d'Est tropical est un vent fort d'altitude (200-150 hPa) observé habituellement le long du golfe de Guinée. Son rôle est plus déterminant dans le cadre de la mousson asiatique (Mishra et Tandon, 1983). De plus, sa position latitudinale moyenne varie peu comparativement à celle de l'AEJ. C'est la raison pour laquelle peu d'études se sont intéressées au lien entre le TEJ et les précipitations sur l'AO. Tout de même, (Nicholson, 2008) a démontré que les positions latitudinales moyennes de l'AEJ et du TEJ constituaient respectivement les limites supérieures et inférieures de la bande de précipitation. Par conséquent, la position moyenne de l'AEJ nous informe sur le degré d'occurrence des pluies dans le Sahel tandis que celle du TEJ n'est pas vraiment utile étant donné que le golfe de Guinée connaît toujours les deux phases de la WAM (Nicholson et Klotter, 2021). Dans cette étude nous allons intégrer les colonnes atmosphériques dans la verticale au-delà de 150 hPa pour que l'étude énergétique puisse prendre en compte le TEJ même si, à première vue, son influence sur la variabilité interannuelle de la WAM semble peu évidente.

Pour mieux comprendre chacune de ses composantes du climat de l'Afrique de l'Ouest et comment elles interagissent entre elles, nous avons choisi d'appliquer une approche d'énergétique atmosphérique présentée dans la suite.

Le concept d'énergétique de l'atmosphère

L'étude de l'énergétique atmosphérique permet de quantifier les processus physiques durant les phases de transformation d'énergie au sein du fluide atmosphérique. (Margules, 1903) fut l'un des premiers à s'intéresser à l'énergétique atmosphérique. Son principal objectif était de trouver une variable permettant d'estimer la quantité maximale d'énergie disponible dans une colonne atmosphérique pour produire une tempête. Il démontra que les énergies potentielles et internes sont proportionnelles à l'intérieur d'une colonne s'étendant jusqu'au sommet de l'atmosphère si l'on tient compte de l'approximation hydrostatique. Ce qui lui permit alors d'introduire « *sa* » nouvelle variable appelée Énergie Potentielle Totale (TPE, *Total Potential Energy* en anglais) qui est la somme des énergies potentielles et internes. Malheureusement, dans la pratique TPE n'est pas une bonne mesure de la quantité d'énergie disponible pour produire de l'énergie cinétique sous un procédé adiabatique car l'énergie potentielle n'est pas toute convertible en énergie cinétique. De plus, (Spar, 1949) argumenta au moyen de cartes synoptiques que la théorie énergétique de Margules n'est pas vérifiée par les observations. En effet, dans son étude sur les conversions d'énergie dans les cyclones en développement, il démontra que l'augmentation de l'énergie cinétique des systèmes ouverts n'est pas nécessairement accompagnés par une diminution d'énergie potentielle à cause des flux aux frontières (Smith, 1973).

C'est en considérant la circulation générale atmosphérique que (Lorenz, 1955) démontre l'application de la théorie de Margules. En effet, lorsque l'on considère toute l'atmosphère, il est possible d'obtenir une variable responsable de la production des tempêtes. Elle s'obtient en faisant la différence entre l'énergie potentielle totale de toute l'atmosphère et l'énergie potentielle totale qui existerait si la masse atmosphérique était redistribuée en conservant sa température potentielle entraînant une stratification horizontale stable. Cette énergie est appelée énergie potentielle disponible (APE, *Available Potential Energy* en anglais). À contrario, il existe une énergie non accessible par le système (UPE, *Unavailable Potential Energy* en anglais) ou énergie minimale du système qui ne peut pas être transformée en énergie cinétique, car la stratification horizontale de l'atmosphère ne produit aucun gradient horizontal de pression pour générer les vents. Il n'y a donc que l'excédent par rapport à cette énergie minimale qui est virtuellement convertible en énergie cinétique (KE, *Kinetic Energy* en anglais). Lorenz démontre aussi dans cette même publication que l'APE est du même ordre de grandeur que l'énergie cinétique et beaucoup plus faible que l'énergie potentielle totale (TPE, *Total Potential Energy* en anglais); le

rapport APE/TPE est inférieur à 1%. Ce concept novateur a permis entre autres de comprendre pourquoi les mesures de vent observées sur tout le globe étaient très inférieures à celles auxquelles on devrait s'attendre si l'on considère toute l'énergie solaire incidente absorbée par l'atmosphère.

Dans la pratique, ce modèle de Lorenz permet de définir un cycle d'énergie applicable à l'échelle globale permettant de comprendre les conversions d'énergie au sein du fluide atmosphérique. Ce cycle s'obtient en séparant l'énergie potentielle disponible A et l'énergie cinétique K en moyennes zonales (notées respectivement \overline{A}_z et \overline{K}_z) et déviations par rapport à celles-ci (\overline{A}_E et \overline{K}_E). Les deux premiers termes sont respectivement proportionnels aux variances de température et de vent moyennés zonalement, tandis que les deux derniers sont respectivement proportionnels aux variances de température et de vent à l'intérieur des cercles de latitude. L'établissement des équations pronostiques de ces quatre termes permet d'obtenir un cycle énergétique complet applicable à l'échelle globale. Sur cette base, (Oort, 1964) présenta un premier estimé numérique des termes du bilan d'énergie. Les résultats montrent que les échanges d'énergie entre les réservoirs suivent un chemin barocline. En d'autres termes, l'énergie disponible dans le réservoir \overline{A}_z permet d'alimenter \overline{A}_E , qui à son tour sert de source d'énergie pour \overline{K}_E , et qui à son tour alimente \overline{K}_z . Le cycle se ferme lorsque l'énergie cinétique de moyenne zonale \overline{K}_z réalimente l'énergie potentielle disponible de moyenne zonale \overline{A}_z .

Dans la continuité, (Pearce, 1978) a développé un autre cycle d'énergie permettant de tenir compte de la stratification verticale de l'atmosphère. Son idée était de définir l'APE comme un état de référence dans lequel prévaut un équilibre isotherme et non isentropique, tel que suggéré par Lorenz (1955). Cette nouvelle formulation a pour conséquence théorique d'introduire un terme supplémentaire lors de la décomposition de la variable A :

$$A = A_S + A_Z + A_E \quad (0-3)$$

La nouvelle variable A_S est dite la composante « *de stabilité statique* » de l'énergie potentielle disponible, car elle conserve toute l'information sur la structure verticale de la température de

l'atmosphère. La décomposition des réservoirs en moyenne zonale et les déviations par rapport à celle-ci reste inchangée par rapport au cycle de Lorenz. L'avantage de ce nouveau cycle est que les composantes zonales et de perturbation de l'enthalpie disponible ne dépendent que des variations horizontales de température. Les calculs de ces termes peuvent par conséquent être effectués pour différents niveaux de pression ou différentes couches atmosphériques. Ce formalisme augmente la précision des calculs des termes du bilan d'énergie et rend leur interprétation physique plus aisée. La théorie de (Pearce, 1978) est conceptuellement plus avancée que celle de Lorenz, mais l'emploi d'intégrations par parties associées à des conditions aux limites globales (colonnes verticales infinies et extension horizontale à toute l'atmosphère) restreint son application uniquement à l'échelle globale (Marquet, 1990).

Marquet (Marquet, 1991, 1994, 2003a) a poursuivi les travaux de (Pearce, 1978) dans le but d'arriver à une définition locale du cycle d'enthalpie utilisable. Il considère que chaque point de l'atmosphère contient une fraction d'enthalpie spécifique utilisable a_h pouvant être séparée en contributions indépendantes de température ($a_T(T)$, bleu) et de pression ($a_p(p)$, rouge) comme suit :

$$a_h(T, p) = (h - T_r s) - (h_r - T_r s_r) = \textcolor{blue}{C_p T_r} \left[\left(\frac{T - T_r}{T_r} \right) - \ln \left(\frac{T}{T_r} \right) \right] + \textcolor{red}{R T_r} \ln \left(\frac{P}{P_r} \right) = \textcolor{blue}{a_T(T)} + \textcolor{red}{a_p(p)} \quad (0-4)$$

Grâce à cette décomposition mathématique '*exacte*', on peut étudier l'énergétique d'un ensemble de points de grille. Par conséquent, il est possible d'utiliser des modèles régionaux à haute résolution pour étudier l'énergétique des domaines à aire limitée dans le but de comprendre comment naissent, se développent et se dissipent les systèmes météorologiques se développant à fine échelle.

La fonction d'enthalpie spécifique de (Marquet, 1991) est une généralisation de la fonction d'énergie potentielle globale disponible ($h - T_r s$) de (Pearce, 1978):

$$\frac{dAPE}{dt} = \frac{d(h - T_r s)}{dt} \quad (0-5)$$

qui est une solution de (0-5), au même titre qu'*APE*. De plus, une autre innovation de Marquet est la décomposition du terme d'énergie cinétique en trois composantes comme c'est le cas avec la composante APE dans le cycle de (Pearce, 1978) (équation (0-3)). Cette décomposition ajoute à nouveau un réservoir d'énergie supplémentaire (K_S) qui tient également compte de la stabilité statique de l'atmosphère. Des termes de flux représentant les échanges de matière entre le domaine choisi et les masses d'air environnantes s'ajoutent naturellement pour résoudre « *le problème de fermeture* ».

Plus récemment, (Nikiéma et Laprise, 2013) ont remarqué le parallèle qui existait entre les conversions d'énergie associées avec la fluctuation temporelle de la variabilité interne dans des simulations d'ensemble effectuées sur les modèles régionaux de climat (RCM, *regional climate model*) et les conversions d'énergie qui prennent place dans les systèmes météorologiques. Les auteurs se sont donc inspirés des travaux de Marquet pour développer un ensemble d'équations (ou cycle d'énergie) permettant d'étudier la variabilité interne dans des simulations d'ensemble effectuées sur les RCM. Plutôt que de regarder les moyennes zonales et les perturbations autour de celles-ci à l'horizontale, (Nikiéma et Laprise, 2013) ont décomposé les équations pronostiques développées en moyenne d'ensemble des membres de la simulation et déviations par rapport à celle-ci. Puis, (Clément *et al.*, 2017) ont fait un premier essai pour développer le bilan d'énergie des perturbations transitoires.

Objectifs et présentation de la thèse

Pour comprendre les alternances entre les années sèches et humides en Afrique de l'Ouest, ainsi que les extrêmes météorologiques observés, nous proposons une approche de bilan d'énergie de l'atmosphère. Cette méthode se distingue des méthodes traditionnelles par son approche quantitative permettant d'adosser des valeurs numériques sur les processus physiques, ce qui permet de distinguer aisément les processus dominants de ceux qui le sont moins.

Les trois principaux objectifs de cette thèse sont : 1) de s'inspirer des récentes avancées sur l'énergétique des domaines régionaux pour former un cycle complet d'équations permettant à la fois l'étude des petites et des grandes échelles, 2) d'appliquer l'énergétique des grandes échelles

au climat Ouest Africain pour comprendre les écarts de pluviométrie entre les saisons de mousson, et 3) d'appliquer l'énergétique des petites échelles à une importante onde de l'Est Africaine pour comprendre les processus physiques responsables de sa génération, sa croissance et sa dissipation. La thèse est présentée sous forme d'articles scientifiques rédigés en anglais pour faciliter leur publication dans des revues spécialisées.

Le Chapitre 1 s'intitule « *Un cycle d'énergie détaillé des domaines à aire limitée pour les études météorologiques et climatiques : application sur l'Afrique de l'Ouest durant trois saisons de moussons contrastantes 1997 (sèche), 1999 (humide) et 2006 (normale)* ». Ce chapitre répond à nos deux premiers objectifs. Pour établir un cycle d'énergie complet, il faut partir de la décomposition de Reynolds pour séparer l'énergie cinétique et l'enthalpie disponible en petites et grandes échelles. Une formulation du bilan d'énergie des grandes échelles a déjà été proposée par (Nikiéma et Laprise, 2013). Il suffira donc d'y ajouter notre formulation du bilan d'énergie des petites échelles. Cependant, pour s'assurer de la véracité et de la concordance des bilans que nous allons présenter, il faudra s'assurer qu'en additionnant toutes les équations des petites et des grandes échelles, nous retombions sur les équations d'énergie cinétique et d'enthalpie qui sont issues directement des équations primitives atmosphériques. Ensuite, l'étude de cas en Afrique de l'Ouest se fera en appliquant le bilan des grandes échelles aux simulations du MRCC6 pilotées par la réanalyse ERA5 sur les 3 saisons de mousson contrastées 1997 (sèche), 1999 (humide) et 2006 (normale). L'analyse des différences entre les termes du bilan d'énergie des grandes échelles pour les trois années, nous permettra d'identifier et d'évaluer les processus physiques responsables de la variabilité des précipitations.

Le Chapitre II s'intitule « *Étude énergétique d'une onde d'Est Africaine simulée par le MRCC6 en utilisant les équations du bilan d'énergie des perturbations transitoires* ». Afin d'appliquer les équations du bilan des petites échelles sur une importante onde de l'Est, nous commencerons par identifier tous les AEWs qui ont traversé le continent durant nos trois saisons contrastées, puis nous choisirons celui le plus intéressant selon nos critères. En prenant le bilan des grandes échelles comme référence, nous verrons les termes qui s'écartent le plus de la climatologie. Ces termes nous indiqueront les processus qui contribuent le plus au développement des systèmes météorologiques importants.

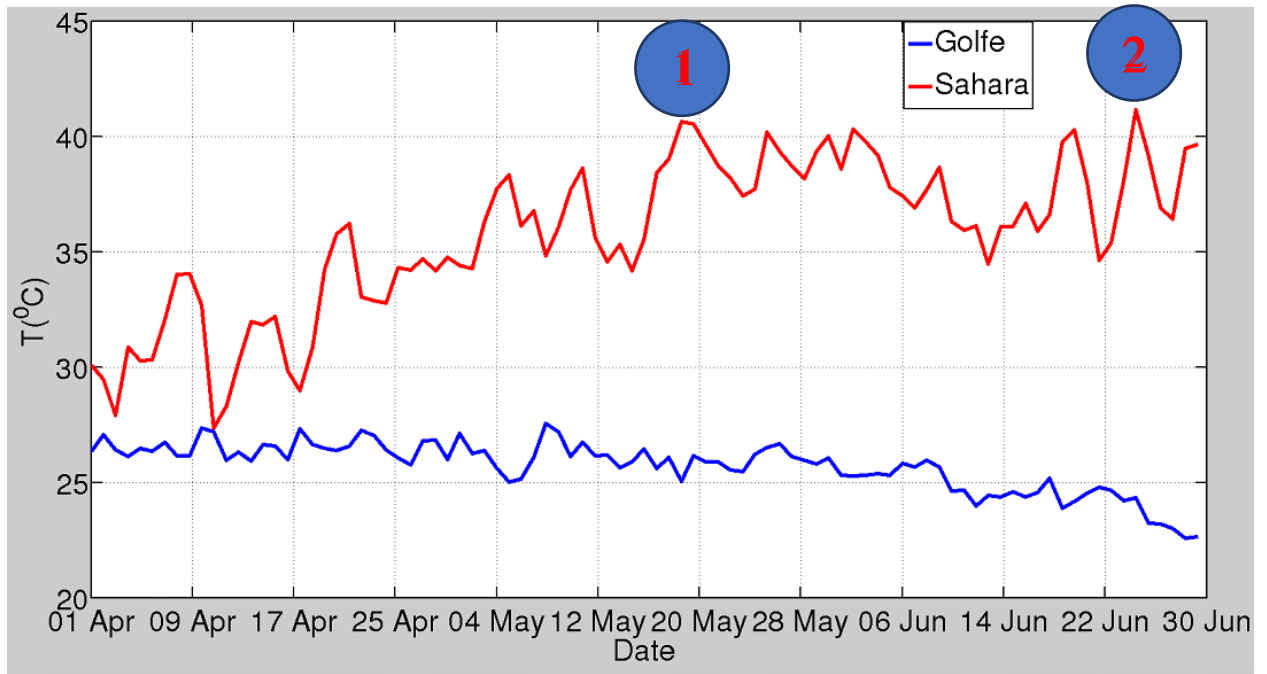


Figure 0 - 1: Évolution temporelle de la moyenne journalière de la température en surface dans le Golfe de Guinée et le Sahara (pour deux mailles choisies au hasard) du 1er avril au 30 juin 2009, à l'aide des réanalyses ERA5.

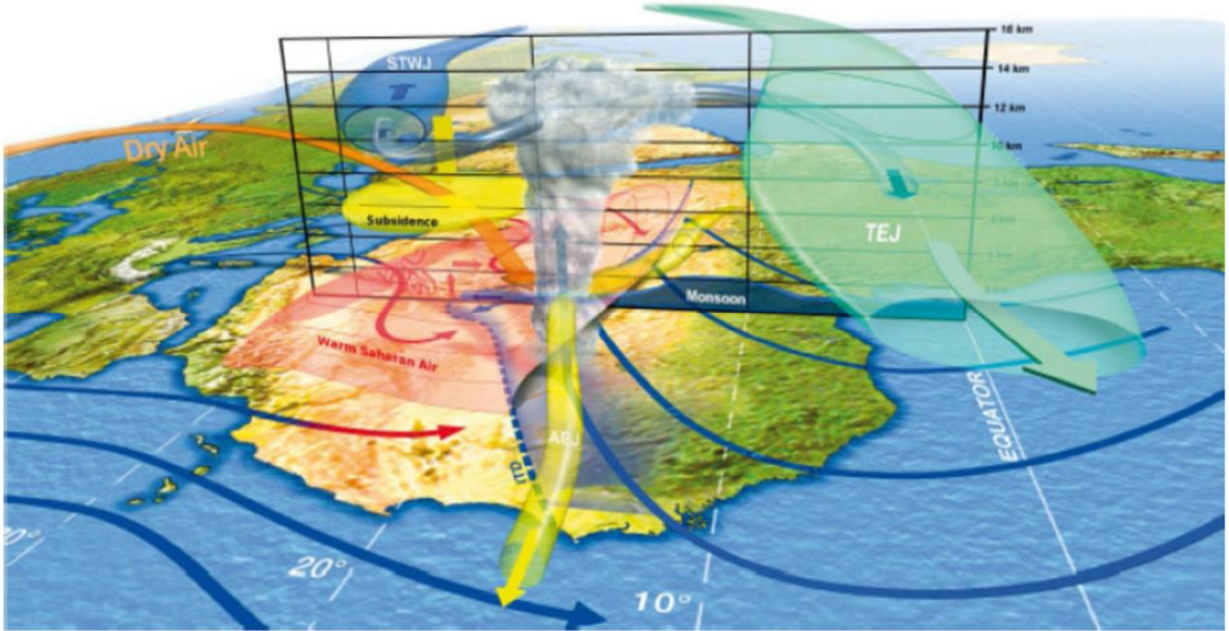


Figure 0 - 2: : Coupe tri-dimensionnelle de la WAM, Source : (Lafore *et al.*, 2011).

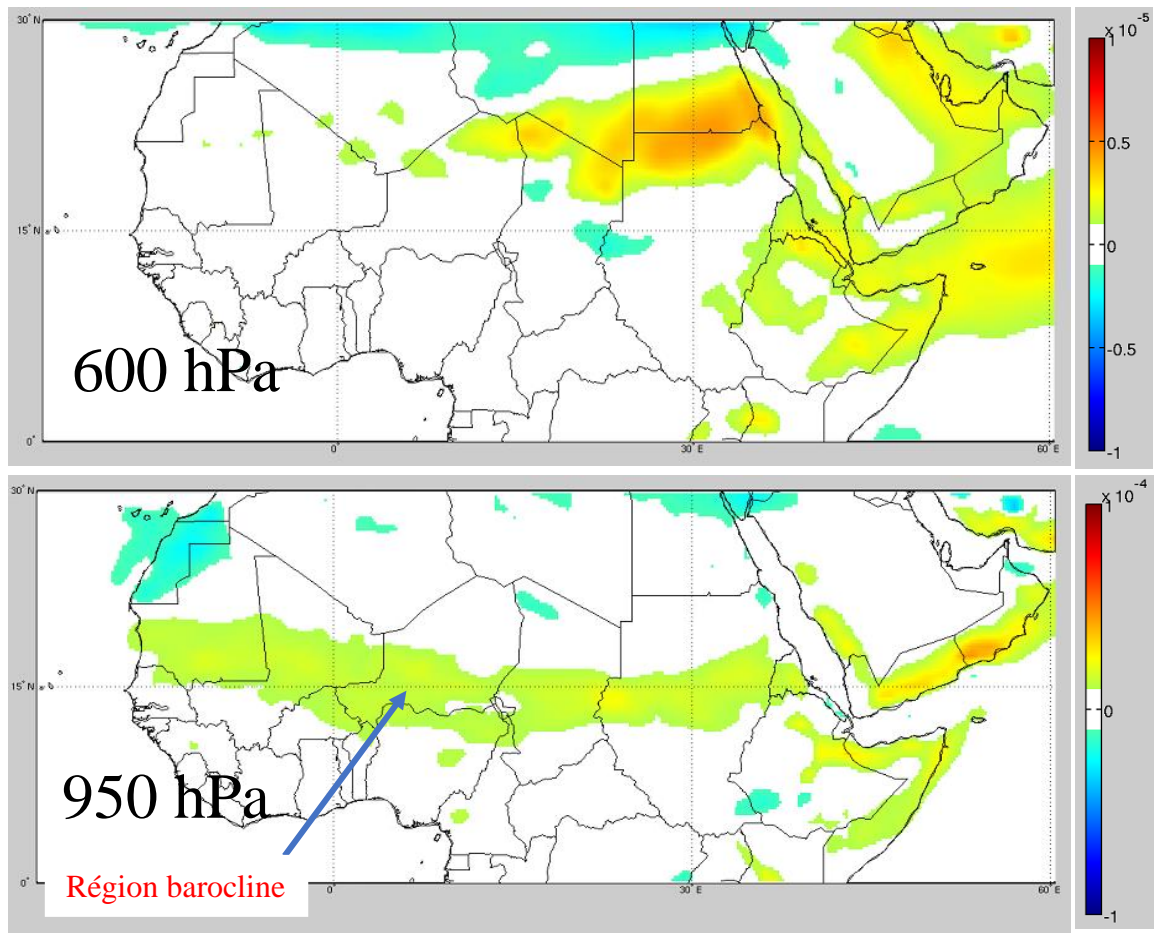


Figure 0 - 3: Gradient méridien de température sur la zone sahélienne de l'Afrique à 600 hPa (panneau du haut) et à 950 hPa (panneau du bas) moyennés de Juin à septembre 2009 à l'aide des réanalyses ERA Intérim. L'unité est le Kelvin/m.

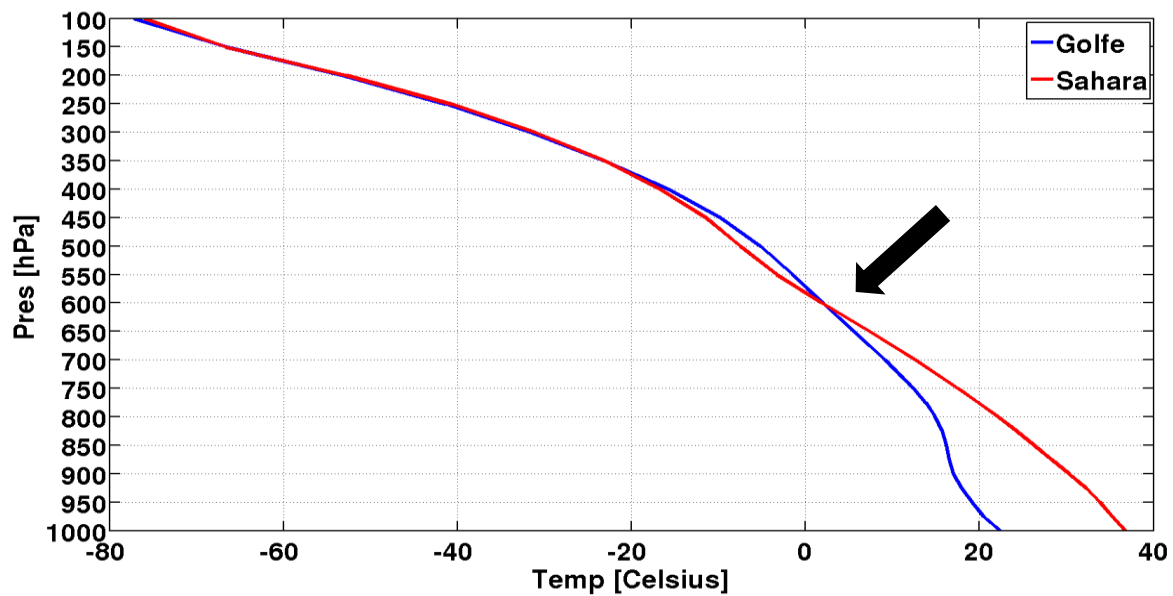


Figure 0 - 4: Profil vertical de la température pour deux points choisis au hasard dans le Golfe de Guinée (en bleu) et le Sahara (en rouge) moyennés entre les mois de juillet et septembre 2009 à l'aide des réanalyses ERA Intérim. Le niveau de l'AEJ est indiqué par la flèche noir.

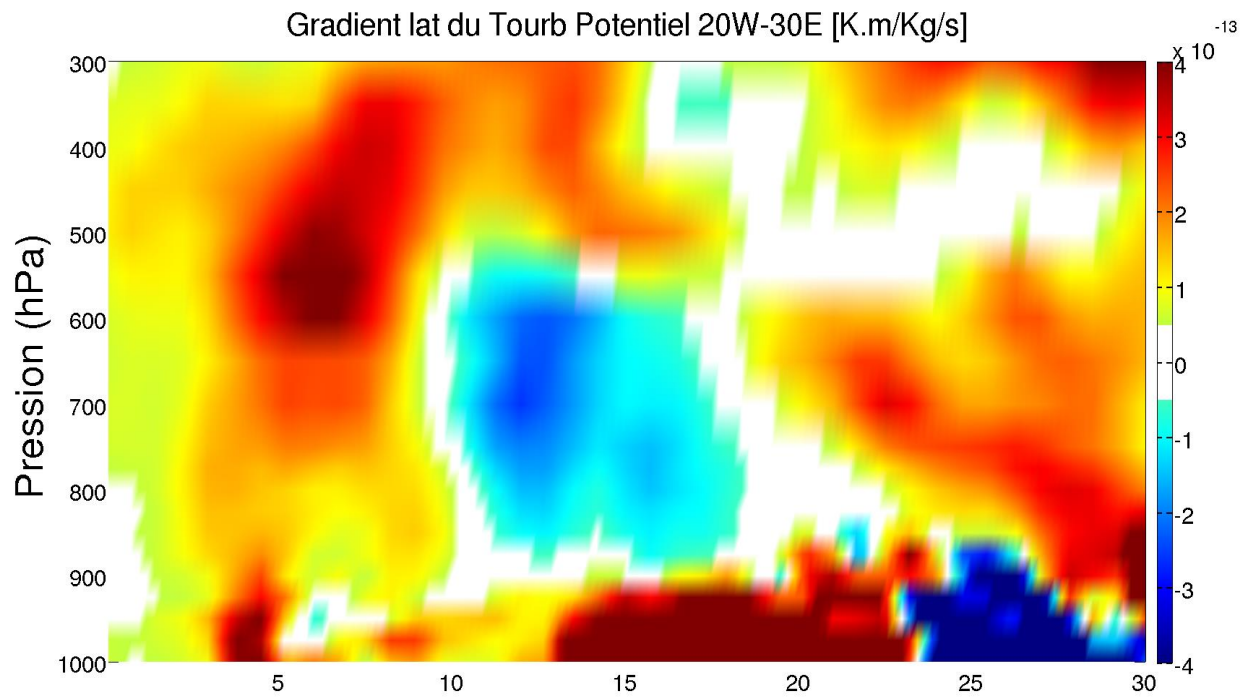


Figure 0 - 5: : Coupe verticale de q_y entre 20°O et 30°E , moyennée de juillet à septembre 2009 en K.m/kg/s entre les latitudes 0 et 30°N à l'aide des réanalyses ERA Intérim.

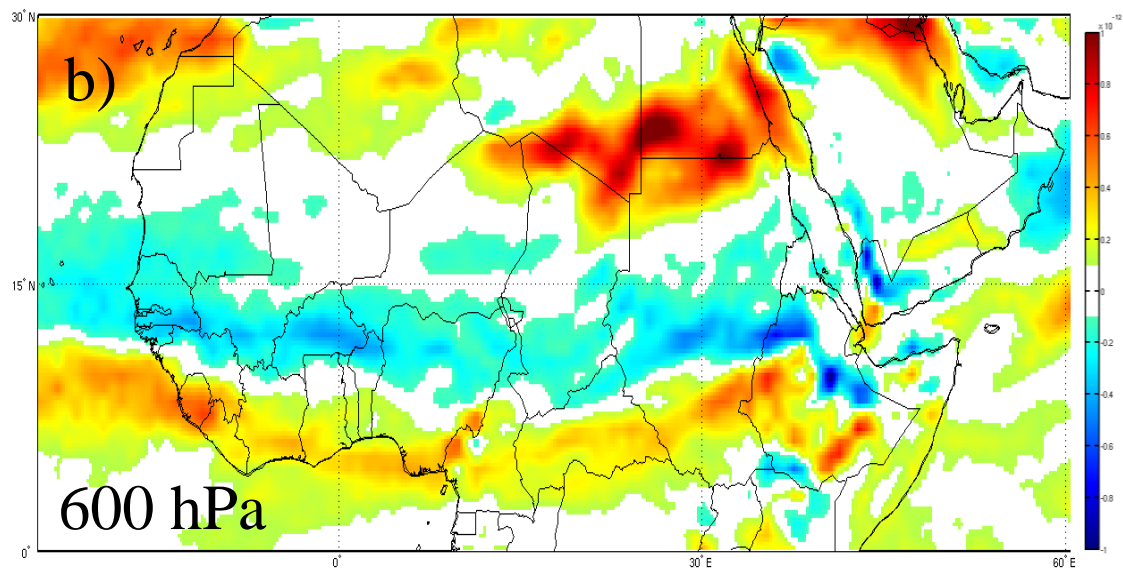
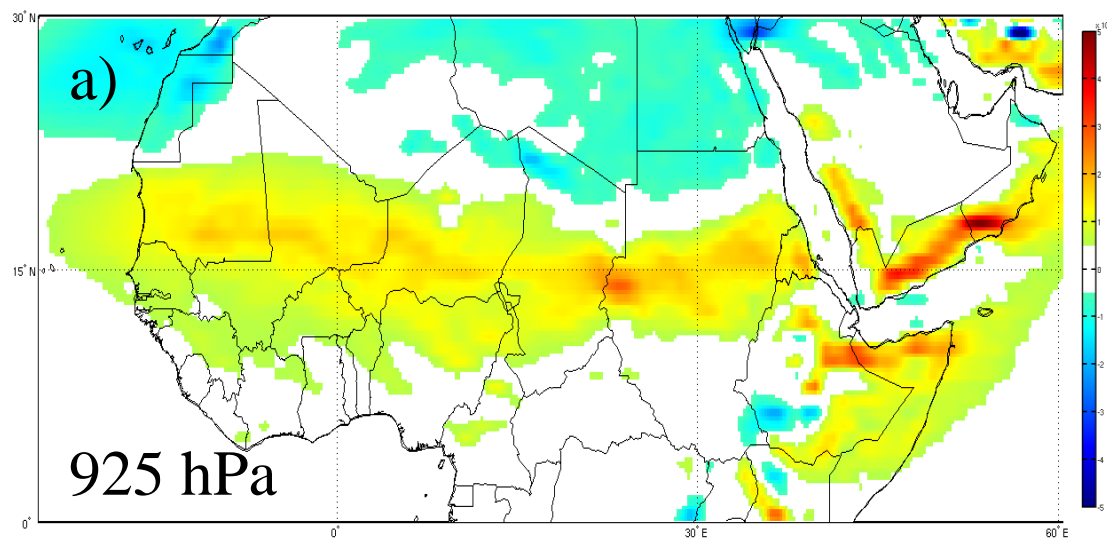


Figure 0 - 6: Profils horizontaux des gradients de température potentielle (à la surface i.e 925 hPa , en K/m) (a) et de tourbillon potentiel (au niveau du Jet à 700hPa, en K.m/kg/s) (b), à l'aide des réanalyses ERA Intérim.

CHAPITRE 1

A detailed limited-area energy cycle for climate and weather studies: application over the West African climate during three summers 1997 (dry), 1999 (wet) and 2006 (normal)

This work has been submitted for publication in the peer-reviewed journal Climate Dynamics. The detailed reference is:

Y. Ngueto, R. Laprise and O. Nikiéma. 2023. “A detailed limited-area energy cycle for climate and weather studies: application over the West African climate during three contrasting summers 1997 (dry), 1999 (wet) and 2006 (normal)”. *In review in Climate Dynamics*.

Abstract

The West African Monsoon (WAM) is a climate system that involves a complex chain of interacting physical processes ranging from small to large temporal and spatial scales. In this work, a detailed atmospheric energy cycle is formulated for limited-area domains in order to understand the WAM intra-seasonal and interannual variability. The energy cycle is cast in terms of available enthalpy and kinetic energy reservoirs. According to the employed definition, the time-averaged (climate) energy reservoirs are decomposed in a component associated with the time-averaged atmospheric state and a component due to the time-averaged statistics of transient-eddies. With this approach, a storm energy is defined as the deviation of instantaneous energy from its climate value. The application of energy cycle on the simulated WAM climatology reveals that the available enthalpy of the time-averaged state (A_M) is the largest energy reservoir, while the transient-eddy component (A_E) is the smallest. On the other hand, the time-averaged and the time-variability kinetic energy reservoirs (K_M and K_E) have the same order of magnitude, confirming previous studies linking the African Easterly Waves with a mixed barotropic/baroclinic mechanism. A detailed analysis reveals that, in the time-mean state, there is a huge loss of energy flux due to time-averaged pressure work in boundary fluxes, with the result that only a little fraction of A_M associated with the ageostrophic circulation contributes to the generation of K_M . On the other hand, the loss of A_E contributes almost entirely to the gain in K_E , indicating negligible loss due to transient-eddy pressure work.

Keywords: Atmospheric energetics; Limited area; West African Monsoon; African Easterly Waves

1.1 Introduction

During the boreal summer, the northward shift of monsoon flow brings a huge amount of humidity over the West African hot continental surface, producing the only rainy period of the year in the southern belt of the Sahara Desert, the Sahel. This phenomenon, known as the West African Monsoon (WAM), is the most important feature of the West African climate. The WAM exhibits large interannual variability in terms of rainfall occurrence and geographic distribution. During wetter years, damaging rainfall and rain-induced flooding occur from time to time in the drought-prone Sahel savanna zone, but official records of these events and their socioeconomic impacts are meager (Tarlule, 2005). On the other hand, during dryer years, precipitation deficit leads to food insecurity and a decline in water resources for West African populations (Gowing, 2003).

Over the last two decades, many efforts have been made to improve understanding of the physical mechanisms responsible for the WAM variability. The African Monsoon Multidisciplinary Analysis (AMMA; (Redelsperger *et al.*, 2006))program was dedicated to providing a better understanding of the West African monsoon and its influence on the physical, chemical and biological environment, as well as relating variability of this monsoon system to issues of health, water resources, food security and demography for West African nations (Lebel *et al.*, 2010). The AMMA Model Intercomparison Project (AMMA-MIP; (Hourdin *et al.*, 2010)) is an intercomparison and evaluation exercise of both global and regional atmospheric models, focused on the study of the seasonal and intraseasonal variations of the climate and rainfall over the Sahel. The AMMA Land Surface Model Intercomparison Project (ALMIP; (Boone *et al.*, 2009)) currently provides the best estimate of the land-surface processes over West Africa from 2004 to 2007. The West African Monsoon Modeling and Evaluation (WAMME; (Xue *et al.*, 2010)) evaluated the general circulation models (GCM) performances in simulating variability of WAM precipitation, surface temperature, and major circulation features at seasonal and

intraseasonal scales. Major progress has been achieved through these projects in the understanding of individual key features of the WAM: the atmospheric boundary layer (ABL), the mid-level African easterly jet (AEJ) and the African easterly waves (AEWs) (Lafore *et al.*, 2011). However, tools are required to further our understanding of interactions taking place between these individual features.

In this context, we develop and apply an atmospheric energetic cycle over a limited-area domain in the WAM. The seminal work of (Lorenz, 1955) on the global atmospheric energetics allowed understanding energy transformation within the atmosphere; this approach has also been useful for the evaluation of GCMs simulations skill at replicating the atmospheric behaviour (Li *et al.*, 2007). Atmospheric energy cycle formulations suitable for limited area have also been developed. (Marquet, 2003a) established a local energy cycle formulation, useful to understand the transformations of energy occurring locally in the atmosphere. noted NL13 hereafter, applied a variant of this formalism toward understanding of internal variability in regional climate model (RCM) simulations. (Clément *et al.*, 2017) attempted to apply this formalism to study mid-latitude storm energetics. However, the transient-eddy energetics failed to converge to towards zero in the limit of long time.

The first objective of this paper is to redevelop a coherent set of locally applicable atmospheric energetic equations for the energy budgets of both the climate (time-mean structure and transient-eddy average statistics) and the time evolution of transient eddies. To avoid having a whole paper on the theory of atmospheric energetics, the second objective is to apply the developed climate energetics formalism to understand intraseasonal and interannual variability of the WAM. In a companion paper, the full potential of the revised energetics formalism will be exploited to study the time evolution of transient eddies.

The paper is organised as follows. In section 2, we develop a methodology for the computation of an atmospheric energy cycle suitable for both the climate and the time evolution of transient eddies. Section 3 will describe the model used for the simulations and the region of interest, where the climate energy cycle will be assessed. Section 4 will present results of the West Africa energy budget in three contrasting years to reveal the interannual variability. Finally, section 5 will summarise the findings and conclude.

1.2 Methodology for the computation of an atmospheric energy cycle suitable for both climate and weather studies

Atmospheric energetics identifies the different reservoirs (potential or kinetic) of energy in the atmosphere and according to conservation laws, describe the conversion flow from one reservoir to another. In this context, mechanisms responsible of those conversions are physical processes. Therefore, an atmospheric energy cycle identifies different physical processes responsible of the growth or the decay of the mechanical energies. Lorenz provided the first modern picture of the mechanical energies and their conversions for the global atmosphere, which is called the *Lorenz energy cycle*. Such an energy cycle can help diagnose the atmospheric dynamics and general circulation, which is widely used in the studies of the atmospheres (Pan *et al.*, 2017).

The interpretation of the physical mechanisms responsible for the maintenance of the atmospheric general circulation and the life cycle of weather systems is facilitated by the decomposition of atmospheric variables and energies into their time-mean and transient-eddy components. (Lorenz, 1955, 1957) has shown that casting the thermodynamic energy equation in the form of a quadratic quantity – Available Potential Energy (APE) –has the advantage of focussing on the active component of thermodynamic energy available to produce storms. APE is a positive definite quantity that is much smaller in magnitude than total thermodynamic energy. The quadratic formulation of APE parallels that of kinetic energy, which facilitates the decomposition in time-mean and transient-eddy components. The APE approach has been widely used for global atmospheric energetic studies.

Regional energetic studies however require a somewhat different approach as “APE is a global concept defined for a system as a whole, not for a portion of it” (van Mieghem 1973, section 14.8). (Marquet, 1991, 1994, 2003a, 2003b) proposed a locally defined approach based on Available Enthalpy, a positive-definite quantity that can be split into contributions depending solely on temperature and pressure. For the moderate range of temperatures encountered in the atmosphere, a quadratic approximation to the temperature-dependent component of Available Enthalpy (henceforth noted as A) can be used.

$$A = \frac{C_p}{2T_r} (T - T_r)^2 \quad (1.1)$$

where T_r , the reference temperature and C_p , the specific heat at constant pressure for dry air, are constant (Marquet, 1991; Pearce, 1978). With this approximation, the expression for available enthalpy parallels the quadratic form of the kinetic energy:

$$K = \frac{1}{2} \overrightarrow{V_H} \cdot \overrightarrow{V_H} \quad (1.2)$$

which can be used advantageously for energetic studies over limited-area domains.

1.2.1 Decomposition rule of quadratic quantities

The quadratic form of the kinetic energy K and available enthalpy A is very convenient for their decomposition in time-mean and time-deviation contributions. Consider a quadratic quantity $E = \psi^2$ decomposed as $\psi = \langle \psi \rangle + \psi'$ where $\langle \rangle$ denotes the time mean and $(\cdot)'$ the departure thereof. Then $E = \langle \psi \rangle^2 + \psi'^2 + 2\langle \psi \rangle \psi'$ and hence

$$E = E_C + E_x \quad (1.3)$$

where

$$E_C = \langle E \rangle = \langle \psi \rangle^2 + \langle \psi'^2 \rangle \quad (1.4)$$

is the climatological (time-mean) part and

$$E_x = E - E_C = \left(\psi'^2 - \langle \psi'^2 \rangle \right) + 2\langle \psi \rangle \psi' \quad (1.5)$$

reflects the departures thereof (energy fluctuations). We note in passing that $\langle E_x \rangle = 0$.

The climatological energy E_C can further be split as follows:

$$E_C = E_M + E_E \quad (1.6)$$

where $E_M = \langle \psi' \rangle^2$ is the contribution associated with the time-mean variables and $E_E = \langle \psi'^2 \rangle$ is the contribution associated with variance of time deviations (transient eddies); both contributions are relevant for climate studies.

Energy fluctuations also can be split as follows:

$$E_X = E_{X1} + E_{X2} \quad (1.7)$$

where $E_{X1} = \psi'^2 - \langle \psi' \rangle^2$ and $E_{X2} = 2\langle \psi' \rangle \psi'$ involve quadratic and linear contributions of transient eddies, respectively (see “Appendix 2” for details).

We note that while time deviations of variables ψ' contribute to both E_E and E_X , only E_E contributes to the time-mean energy since $\langle E_X \rangle = 0$, and only E_X contributes to the time variation of E , as $d_t E_E = 0$.

Hence to summarise

$$E = E_M + E_E + E_X \quad (1.8)$$

In an earlier study of the energetics of the life cycle of a storm, (Clément *et al.*, 2017) considered the quantity $E_{TV} = \psi'^2$ to characterize the time variations of a storm energetics. It appears in retrospect that E_X is the more appropriate variable, as it is the one contributing to the time variation of E : $d_t E = d_t E_X$.

Using this approach, the kinetic energy K and potential enthalpy A can be decomposed as follows:

$$\begin{aligned} K &= \frac{1}{2} \vec{V}_h \cdot \vec{V}_h \\ &= K_M + K_E + K_X \end{aligned} \quad (1.9)$$

where

$$\begin{aligned}
K_M &= \frac{1}{2} \langle \vec{V}_h \rangle \cdot \langle \vec{V}_h \rangle \\
K_E &= \frac{1}{2} \left[\langle \vec{V}_h \cdot \vec{V}_h \rangle - \langle \vec{V}_h \rangle \cdot \langle \vec{V}_h \rangle \right] = \frac{1}{2} \langle \vec{V}_h \cdot \vec{V}_h \rangle \\
K_X &= \frac{1}{2} \left[\vec{V}_h \cdot \vec{V}_h - \langle \vec{V}_h \cdot \vec{V}_h \rangle \right] = \frac{1}{2} \left(\langle \vec{V}_h \cdot \vec{V}_h \rangle - \langle \vec{V}_h \cdot \vec{V}_h \rangle \right) + \langle \vec{V}_h \rangle \cdot \vec{V}_h
\end{aligned}$$

and

$$\begin{aligned}
A &= \frac{C_p}{2T_r} (T - T_r)^2 \\
&= A_M + A_E + A_X
\end{aligned} \tag{1.10}$$

Where

$$\begin{aligned}
A_M &= \frac{C_p}{2T_r} \langle T - T_r \rangle^2 \\
A_E &= \frac{C_p}{2T_r} \left[\langle (T - T_r)^2 \rangle - \langle T - T_r \rangle^2 \right] = \frac{C_p}{2T_r} \langle T^2 \rangle \\
A_X &= \frac{C_p}{2T_r} \left[(T - T_r)^2 - \langle (T - T_r)^2 \rangle \right]
\end{aligned}$$

In the following sections, we establish the relevant equations for the time-mean climate ($E_C = E_M + E_E$) and for the time variations associated with weather systems ($E_X = E_{X1} + E_{X2}$).

1.2.2 Energy equations

Under hydrostatic equilibrium, the field equations can be expressed in pressure coordinate as follows:

$$\frac{\partial \vec{V}_h}{\partial t} + (\vec{V} \cdot \vec{\nabla}) \cdot \vec{V}_h + f \vec{k} \times \vec{V}_h + \vec{\nabla}_h \phi - \vec{F}_h = \vec{0} \tag{1.11}$$

$$\frac{\partial T}{\partial t} + (\vec{V} \cdot \vec{\nabla}) T - \frac{\omega \alpha_r}{C_p} - \frac{Q}{C_p} \simeq 0 \tag{1.12}$$

$$\vec{\nabla} \cdot \vec{V} = 0 \tag{1.13}$$

$$\frac{\partial \phi}{\partial p} + \alpha = 0 \quad (1.14)$$

$$\alpha - \frac{RT}{p} = 0 \quad (1.15)$$

Eq. (11) is the horizontal momentum equation where $\vec{V}_h(u,v)$ is the horizontal wind vector, $\vec{V}(u,v,\omega)$ is the three-dimensional wind vector with $\omega=dp/dt$ the vertical motion in pressure coordinate, f is the Coriolis parameter, Φ is the geopotential, and \vec{F}_h is the external horizontal force. Eq. (12) is an approximate form of the enthalpy equation where C_p is the specific heat at a constant pressure, α is the specific volume and Q is the total diabatic heating rate. Eq. (13) is the mass continuity equation, eq. (14) is the hydrostatic equilibrium equation, and eq. (15) is the equation of state for an ideal gas. In these equations $\overline{\nabla}_h = \left(\frac{\partial}{\partial x}, \frac{\partial}{\partial y} \right)$ and $\overrightarrow{\nabla} = \left(\frac{\partial}{\partial x}, \frac{\partial}{\partial y}, \frac{\partial}{\partial p} \right)$. In models, these equations are completed by equations describing the evolution of water vapour and liquid and ice clouds and precipitations, the phase conversions of which contributing to the diabatic heating rate.

One should note the use of α_r instead of α in (12); this represents the approximate form of the thermodynamic equation that is consistent with the approximate quadratic form of the available enthalpy (NL13; eq. 65). It differs however of their equation by the absence of the factor of order unity $\frac{T_r}{T}$ affecting the diabatic heating term; eq. (12) is a better approximation in the sense that no further approximation will have to be invoked in the ensuing algebraic manipulations (see “Appendix 3” for details).

1.2.3 Energy budget equations for climate studies

Equations of energy budget come from primitive atmospheric equations (11) to (15). An example of how to obtain the kinetic energy tendency equation is shown in *Appendix 1*. An equation for the climatological mean kinetic energy associated with the time-mean wind, K_M , is obtained by taking the dot product of the time-mean horizontal winds with the time-mean horizontal momentum equation as follows

$$\begin{aligned}\frac{\partial K_M}{\partial t} &= \langle \vec{V}_H \rangle \cdot \frac{\partial \langle \vec{V}_H \rangle}{\partial t} \\ &= -(F_{KM} + H_{KM} + C_K) + C_{MK} - D_M\end{aligned}\quad (1.16)$$

where

$$\begin{aligned}F_{KM} &= \vec{\nabla} \cdot (\langle \vec{V} \rangle K_M) \\ H_{KM} &= \vec{\nabla} \cdot \langle \vec{V}' \left(\vec{V}_h' \cdot \langle \vec{V}_h \rangle \right) \rangle \\ C_K &= -\langle \vec{V}_h' \cdot (\vec{V}' \cdot \vec{\nabla}) \cdot \langle \vec{V}_h \rangle \rangle \\ C_{MK} &= -\langle \vec{V}_h \rangle \cdot \vec{\nabla}_h \langle \phi \rangle \\ D_M &= -\langle \vec{V}_h \rangle \cdot \langle \vec{F}_h \rangle\end{aligned}$$

(see “Appendix 4” for details)

The easiest way to obtain the time-mean kinetic energy associated with time variability of the wind is by subtracting the time-mean kinetic energy equation and the kinetic energy equation associated with time-mean wind as follows:

$$\begin{aligned}\frac{\partial K_E}{\partial t} &= \left\langle \frac{\partial K}{\partial t} \right\rangle - \frac{\partial K_M}{\partial t} = \left\langle \vec{V}_h \cdot \frac{\partial \vec{V}_h}{\partial t} \right\rangle - \langle \vec{V}_h \rangle \cdot \frac{\partial \langle \vec{V}_h \rangle}{\partial t} \\ &= -(F_{KE} + H_{KE} - C_K) + C_{EK} - D_E\end{aligned}\quad (1.17)$$

where

$$\begin{aligned}F_{KE} &= \vec{\nabla} \cdot (\langle \vec{V} \rangle K_E) \\ H_{KE} &= \vec{\nabla} \cdot \left\langle \vec{V}' \left(\frac{\vec{V}_h' \cdot \vec{V}_h'}{2} \right) \right\rangle \\ C_K &= -\langle \vec{V}_h' \cdot (\vec{V}' \cdot \vec{\nabla}) \cdot \langle \vec{V}_h \rangle \rangle \\ C_{EK} &= \langle \vec{V}_h' \cdot \vec{\nabla}_h \phi' \rangle \\ D_E &= -\langle \vec{V}_h' \cdot \vec{F}_h' \rangle\end{aligned}$$

(see “Appendix 5” for details)

An equation for the climatological mean available enthalpy associated with the time-mean temperature, A_M , is obtained by multiplying with $\frac{C_p}{T_r} \langle T - T_r \rangle$ the time-mean thermodynamics equation as follows:

$$\begin{aligned}\frac{\partial A_M}{\partial t} &= \frac{C_p}{T_r} \langle T - T_r \rangle \left\langle \frac{\partial T}{\partial t} \right\rangle \\ &= - (F_{AM} + H_{AM} + C_A) - (C_{MA} - I_{AB}) + G_M\end{aligned}\quad (1.18)$$

where

$$\begin{aligned}C_A &= - \frac{C_p}{T_r} \left(\langle T' \cdot \vec{V}' \rangle \cdot \vec{\nabla} \right) \langle T \rangle \\ F_{AM} &= \vec{\nabla} \cdot \left(\langle \vec{V} \rangle A_M \right) \\ H_{AM} &= \vec{\nabla} \cdot \left\langle \vec{V}' \left(\frac{C_p}{T_r} \langle T - T_r \rangle T' \right) \right\rangle \\ C_{MA} &= - \langle \omega \rangle \langle \alpha \rangle \\ I_{AB} &= - \langle \omega \rangle \alpha_r \\ G_M &= \left\langle \left(\frac{T}{T_r} - 1 \right) \right\rangle \langle Q \rangle\end{aligned}$$

(see “Appendix 6” for details)

An equation for the time-mean available enthalpy associated with time variability of the temperature, A_E , is obtained by subtracting the time-mean available enthalpy equation by the time-mean available enthalpy equation associated with time-mean temperature as follows:

$$\begin{aligned}\frac{\partial A_E}{\partial t} &= \left\langle \frac{\partial A}{\partial t} \right\rangle - \frac{\partial A_M}{\partial t} = \frac{C_p}{T_r} \left\{ \left\langle (T - T_r) \frac{\partial T}{\partial t} \right\rangle - \langle T - T_r \rangle \left\langle \frac{\partial T}{\partial t} \right\rangle \right\} \\ &= - (F_{AE} + H_{AE} - C_A) - C_{EA} + G_E\end{aligned}\quad (1.19)$$

where

$$C_A = -\frac{C_p}{T_r} \left(\langle T' \vec{V}' \rangle \cdot \vec{\nabla} \right) \langle T \rangle$$

$$F_{AE} = \vec{\nabla} \cdot \left(\langle \vec{V} \rangle A_E \right)$$

$$H_{AE} = \vec{\nabla} \cdot \left(\vec{V}' \left(\frac{C_p}{2T_r} T'^2 \right) \right)$$

$$C_{EA} = -\langle \omega' \alpha' \rangle$$

$$G_E = \left\langle \frac{T' Q'}{T_r} \right\rangle$$

(see “Appendix 7” for details)

The equations for K_M (16) and A_M (18) can be linked by making use of the continuity equation (13), hydrostatic equation (14) and state law (15), to get

$$C_{MK} = C_{MA} - F_{\phi M} \quad (1.20)$$

where

$$F_{\phi M} = \vec{\nabla} \cdot \left(\langle \vec{V} \rangle \langle \phi \rangle \right)$$

(see the last section of “Appendix 4” for details)

And similarly for K_E (17) and A_E (19):

$$C_{EK} = C_{EA} - F_{\phi E} \quad (1.21)$$

where

$$F_{\phi E} = \vec{\nabla} \cdot \left(\vec{V}' \phi' \right)$$

(see the last section of “Appendix 5” for details)

We note in passing that $F_{\phi M}$ and $F_{\phi E}$ vanish when integrated over the entire atmosphere (Lorenz, 1955).

1.2.4 Energy budget equations for transient eddies studies

Unlike the earlier study by (Clément *et al.*, 2017) who limited themselves to consider only one term contributing to the time evolution of a storm energetics, here we develop the full transient-eddy equations accounting for all conversions and sources and sinks of energy acting on storms. We reiterate that the advantage of this approach is that all terms appearing in the transient-eddy energy budget vanish when averaged in time.

$$K_x = K_{x1} + K_{x2} \quad (1.22)$$

where

$$\begin{aligned} K_{x1} &= \frac{1}{2} \left(\overrightarrow{V_h'} \cdot \overrightarrow{V_h'} - \langle \overrightarrow{V_h'} \cdot \overrightarrow{V_h'} \rangle \right) \\ K_{x2} &= \langle \overrightarrow{V_h'} \rangle \cdot \overrightarrow{V_h'} \end{aligned}$$

and

$$A_x = A_{x1} + A_{x2} \quad (1.23)$$

where

$$\begin{aligned} A_{x1} &= \frac{C_p}{2T_r} \left(T'^2 - \langle T'^2 \rangle \right) \\ A_{x2} &= \frac{C_p}{T_r} T' \langle T - T_r \rangle \end{aligned}$$

As shown in “Appendix 8”, a prognostic equation for the instantaneous kinetic energy associated with quadratic contributions of wind fluctuations is obtained as follows:

$$\begin{aligned} \frac{\partial K_{x1}}{\partial t} &= \overrightarrow{V_h'} \cdot \frac{\partial \overrightarrow{V_h'}}{\partial t} - \left\langle \overrightarrow{V_h'} \cdot \frac{\partial \overrightarrow{V_h'}}{\partial t} \right\rangle \\ &= -(-c_k + j_k + f_{kx1}) + c_{x1k} - d_{x1} \end{aligned} \quad (1.24)$$

where

$$c_k = -\left\{ \overrightarrow{V_h} \cdot (\overrightarrow{V} \cdot \vec{\nabla}) \cdot \overrightarrow{V_h} - \left\langle \overrightarrow{V_h} \cdot (\overrightarrow{V} \cdot \vec{\nabla}) \cdot \overrightarrow{V_h} \right\rangle \right\}$$

$$j_k = -\overrightarrow{V_h} \cdot \left\langle (\overrightarrow{V} \cdot \vec{\nabla}) \cdot \overrightarrow{V_h} \right\rangle$$

$$f_{kx_1} = \vec{\nabla} \cdot \left\{ \vec{V} \left(\frac{1}{2} V_h'^2 \right) - \left\langle \vec{V} \left(\frac{1}{2} V_h'^2 \right) \right\rangle \right\}$$

$$c_{x1k} = -\left(\overrightarrow{V_h} \cdot \overrightarrow{\nabla_h \phi} - \left\langle \overrightarrow{V_h} \cdot \overrightarrow{\nabla_h \phi} \right\rangle \right)$$

$$d_{x1} = -\left\{ \overrightarrow{V_h} \cdot \overrightarrow{F_h} - \left\langle \overrightarrow{V_h} \cdot \overrightarrow{F_h} \right\rangle \right\}$$

“Appendix 9” shows that the prognostic equation of the instantaneous kinetic energy associated with linear contributions of wind fluctuations a is obtained as follows:

$$\begin{aligned} \frac{\partial K_{x2}}{\partial t} &= \overrightarrow{V_h} \cdot \frac{\partial \langle \overrightarrow{V_h} \rangle}{\partial t} + \langle \overrightarrow{V_h} \rangle \cdot \frac{\partial \overrightarrow{V_h}}{\partial t} \\ &= -(f_{kx2} - j_k + c_k) + c_{x2k} - d_{x2} \end{aligned} \quad (1.25)$$

where

$$c_k = -\left\{ \overrightarrow{V_h} \cdot (\overrightarrow{V} \cdot \vec{\nabla}) \cdot \overrightarrow{V_h} - \left\langle \overrightarrow{V_h} \cdot (\overrightarrow{V} \cdot \vec{\nabla}) \cdot \overrightarrow{V_h} \right\rangle \right\}$$

$$j_k = -\overrightarrow{V_h} \cdot \left\langle (\overrightarrow{V} \cdot \vec{\nabla}) \cdot \overrightarrow{V_h} \right\rangle$$

$$f_{kx2} = \vec{\nabla} \cdot \left\{ \vec{V} \left(K - \frac{1}{2} V_h'^2 \right) - \left\langle \vec{V} \left(K - \frac{1}{2} V_h'^2 \right) \right\rangle \right\}$$

$$c_{x2k} = -\left(\overrightarrow{V_h} \cdot \overrightarrow{\nabla_h \langle \phi \rangle} - \left\langle \overrightarrow{V_h} \cdot \overrightarrow{\nabla_h \phi} \right\rangle \right)$$

$$d_{x2} = -\left\{ \overrightarrow{V_h} \cdot \langle \overrightarrow{F_h} \rangle + \langle \overrightarrow{V_h} \rangle \cdot \overrightarrow{F_H} \right\}$$

“Appendix 10” demonstrates that the prognostic equation for the instantaneous available enthalpy associated with the quadratic contribution of temperature fluctuations is obtained as follows:

$$\begin{aligned} \frac{\partial A_{x1}}{\partial t} &= \frac{C_p}{T_r} \left(T' \frac{\partial T'}{\partial t} - \left\langle T' \frac{\partial T'}{\partial t} \right\rangle \right) \\ &= -(f_{ax1} + j_a - c_a) - c_{x1a} + g_{x1} \end{aligned} \quad (1.26)$$

where

$$c_a = -\frac{C_p}{T_r} \left\{ \left(T' \vec{V}' \cdot \vec{\nabla} \right) \langle T \rangle - \left\langle \left(T' \vec{V}' \cdot \vec{\nabla} \right) \langle T \rangle \right\rangle \right\}$$

$$f_{ax1} = \vec{\nabla} \cdot \left\{ \vec{V} \left(\frac{C_p}{2T_r} T'^2 \right) - \left\langle \vec{V} \left(\frac{C_p}{2T_r} T'^2 \right) \right\rangle \right\}$$

$$j_a = -\frac{C_p}{T_r} T' \left\langle \left(\vec{V}' \cdot \vec{\nabla} \right) T' \right\rangle$$

$$c_{x1a} = -\{ \omega' \alpha' - \langle \omega' \alpha' \rangle \}$$

$$g_{x1} = \frac{1}{T_r} \{ T' Q' - \langle T' Q' \rangle \}$$

The prognostic equation for the instantaneous available enthalpy associated with the linear contribution of temperature fluctuations is obtained as follows (“Appendix 11”):

$$\begin{aligned} \frac{\partial A_{X2}}{\partial t} &= \frac{C_p}{T_r} \left(T' \frac{\partial \langle T \rangle}{\partial t} + \langle T - T_r \rangle \frac{\partial T'}{\partial t} \right) \\ &= -(f_{ax2} - j_a + c_a) - (c_{x2a} - i_{ab}) + g_{x2} \end{aligned} \quad (1.27)$$

where

$$c_a = -\frac{C_p}{T_r} \left\{ \left(T' \vec{V}' \cdot \vec{\nabla} \right) \langle T \rangle - \left\langle \left(T' \vec{V}' \cdot \vec{\nabla} \right) \langle T \rangle \right\rangle \right\}$$

$$f_{ax2} = \vec{\nabla} \cdot \left\{ \vec{V} \left(A - \frac{C_p}{2T_r} T'^2 \right) - \left\langle \vec{V} \left(A - \frac{C_p}{2T_r} T'^2 \right) \right\rangle \right\}$$

$$j_a = -\frac{C_p}{T_r} T' \left\langle \left(\vec{V}' \cdot \vec{\nabla} \right) T' \right\rangle$$

$$c_{x2a} = -\{ \langle \omega \rangle \alpha' + \omega' \langle \alpha \rangle \}$$

$$i_{ab} = -\omega' \alpha_r$$

$$g_{x2} = \frac{1}{T_r} \{ T' \langle Q \rangle + \langle T - T_r \rangle Q' \}$$

The equations for K_{X1} (24) and A_{X1} (26) can be linked by making use of the continuity equation (13), hydrostatic equation (14) and state law (15), to get:

$$f_{\phi x1} - c_{x1a} = c_{x1k} \quad (1.28)$$

where

$$f_{\phi x1} = \vec{\nabla} \cdot \left\{ \vec{V}' \phi' - \langle \vec{V}' \phi' \rangle \right\}$$

(see the last section of “Appendix 8” for details)

And similarly for K_{x2} (25) and A_{x2} (27):

$$f_{\phi x2} - c_{x2a} = c_{x2k} \quad (1.29)$$

where

$$f_{\phi x1} = \vec{\nabla} \cdot \left\{ \vec{V}' \langle \phi' \rangle - \langle \vec{V}' \rangle \phi' \right\}$$

(see the last section of “Appendix 9” for details)

1.2.5 Verification of energy budget equations for climate and storms studies

By summing time-mean and time-variability equations terms, we recover the former total kinetic energy and available enthalpy equations; demonstrating that no piece of information, from small to large scales, has been lost.

1.2.5.1 Total kinetic energy equation retrieval

$$\begin{aligned}
\frac{\partial K_M}{\partial t} &= - \left[\begin{array}{l} - \langle \vec{V}_h' \cdot (\vec{V}' \cdot \vec{\nabla}) \cdot \langle \vec{V}_h' \rangle \rangle \\ + \vec{\nabla} \cdot (\langle \vec{V}' \rangle K_M) \\ + \vec{\nabla} \cdot \langle \vec{V}' (\vec{V}_h' \cdot \langle \vec{V}_h' \rangle) \rangle \end{array} \right] - \left[\langle \vec{V}_h' \rangle \cdot \vec{\nabla}_h \langle \vec{\phi}' \rangle \right] + \langle \vec{V}_h' \rangle \cdot \langle \vec{F}_h' \rangle \\
\frac{\partial K_E}{\partial t} &= - \left[\begin{array}{l} \langle \vec{V}_h' \cdot (\vec{V}' \cdot \vec{\nabla}) \cdot \langle \vec{V}_h' \rangle \rangle \\ + \vec{\nabla} \cdot (\langle \vec{V}' \rangle K_E) \\ + \vec{\nabla} \cdot \left\langle \vec{V}' \left(\frac{\vec{V}_h' \cdot \vec{V}_h'}{2} \right) \right\rangle \end{array} \right] - \left[\langle \vec{V}_h' \cdot \vec{\nabla}_h \vec{\phi}' \rangle \right] + \left[\langle \vec{V}_h' \cdot \vec{F}_h' \rangle \right] \\
\frac{\partial K_{X1}}{\partial t} &= - \left[\begin{array}{l} \vec{\nabla} \cdot \left\{ \vec{V} \left(\frac{1}{2} V_h'^2 \right) - \left\langle \vec{V} \left(\frac{1}{2} V_h'^2 \right) \right\rangle \right\} + \left\{ \vec{V}_h' \cdot (\vec{V}' \cdot \vec{\nabla}) \cdot \langle \vec{V}_h' \rangle - \langle \vec{V}_h' \cdot (\vec{V}' \cdot \vec{\nabla}) \cdot \langle \vec{V}_h' \rangle \rangle \right\} \\ - \vec{V}_h' \cdot \left\langle (\vec{V}' \cdot \vec{\nabla}) \cdot \vec{V}_h' \right\rangle \end{array} \right] - \left[\begin{array}{l} \langle \vec{V}_h' \cdot \vec{\nabla}_h \vec{\phi}' \rangle - \left\langle \vec{V}_h' \cdot \vec{\nabla}_h \vec{\phi}' \right\rangle \end{array} \right] + \left\{ \vec{V}_h' \cdot \vec{F}_h' - \langle \vec{V}_h' \cdot \vec{F}_h' \rangle \right\} \\
\frac{\partial K_{X2}}{\partial t} &= - \left[\begin{array}{l} \vec{\nabla} \cdot \left\{ \vec{V} \left(K - \frac{1}{2} V_h'^2 \right) - \left\langle \vec{V} \left(K - \frac{1}{2} V_h'^2 \right) \right\rangle \right\} - \left\{ \vec{V}_h' \cdot (\vec{V}' \cdot \vec{\nabla}) \cdot \langle \vec{V}_h' \rangle - \langle \vec{V}_h' \cdot (\vec{V}' \cdot \vec{\nabla}) \cdot \langle \vec{V}_h' \rangle \rangle \right\} \\ + \vec{V}_h' \cdot \left\langle (\vec{V}' \cdot \vec{\nabla}) \cdot \vec{V}_h' \right\rangle \end{array} \right] - \left[\begin{array}{l} \langle \vec{V}_h' \cdot \vec{\nabla}_h \langle \vec{\phi}' \rangle \rangle + \left\langle \vec{V}_h' \cdot \vec{\nabla}_h \vec{\phi}' \right\rangle \end{array} \right] + \left\{ \vec{V}_h' \cdot \langle \vec{F}_h' \rangle + \langle \vec{V}_h' \cdot \vec{F}_h' \rangle \right\} \\
\frac{\partial K}{\partial t} &= - (\vec{V} \cdot \vec{\nabla}) K - \vec{V}_h \cdot \vec{\nabla}_h \vec{\phi} + \vec{V}_h \cdot \vec{F}_h
\end{aligned} \tag{1.30}$$

(see “Appendix 12” for details).

1.2.5.2 Total enthalpy energy equation retrieval

$$\begin{aligned}
\frac{\partial A_M}{\partial t} &= - \left[\begin{array}{l} -\frac{C_p}{T_r} \left(\langle T' \bar{V}' \rangle \cdot \vec{\nabla} \right) \langle T \rangle \\ + \vec{\nabla} \cdot \left(\langle \bar{V} \rangle A_M \right) \\ + \vec{\nabla} \cdot \left\langle \bar{V}' \left(\frac{C_p}{T_r} \langle T - T_r \rangle T' \right) \right\rangle \end{array} \right] + \left(\langle \omega \rangle \langle \alpha \rangle - \langle \omega \rangle \alpha_r \right) + \left\langle \left(\frac{T}{T_r} - 1 \right) \langle Q \rangle \right\rangle \\
\frac{\partial A_E}{\partial t} &= - \left[\begin{array}{l} \frac{C_p}{T_r} \left(\langle T' \bar{V}' \rangle \cdot \vec{\nabla} \right) \langle T \rangle \\ + \vec{\nabla} \cdot \left(\langle \bar{V} \rangle A_E \right) \\ + \vec{\nabla} \cdot \left\langle \bar{V}' \left(\frac{C_p}{2T_r} T'^2 \right) \right\rangle \end{array} \right] - \left[\langle \omega' \alpha' \rangle \right] + \left\langle \frac{T' Q'}{T_r} \right\rangle \\
\frac{\partial A_{X1}}{\partial t} &= - \left[\begin{array}{l} \vec{\nabla} \cdot \left\{ \bar{V} \left(\frac{C_p}{2T_r} T'^2 \right) - \left\langle \bar{V} \left(\frac{C_p}{2T_r} T'^2 \right) \right\rangle \right\} + \\ - \frac{C_p}{T_r} \left\{ \left(T' \bar{V}' \cdot \vec{\nabla} \right) \langle T \rangle - \left\langle \left(T' \bar{V}' \cdot \vec{\nabla} \right) \langle T \rangle \right\rangle \right\} \\ - \frac{C_p}{T_r} T' \left\langle \left(\bar{V}' \cdot \vec{\nabla} \right) T' \right\rangle \end{array} \right] - \left\{ \omega' \alpha' - \langle \omega' \alpha' \rangle \right\} + \frac{1}{T_r} \left\{ T' Q' - \langle T' Q' \rangle \right\} \\
\frac{\partial A_{X2}}{\partial t} &= - \left[\begin{array}{l} \vec{\nabla} \cdot \left\{ \bar{V} \left(A - \frac{C_p}{2T_r} T'^2 \right) - \left\langle \bar{V} \left(A - \frac{C_p}{2T_r} T'^2 \right) \right\rangle \right\} - \\ - \frac{C_p}{T_r} \left\{ \left(T' \bar{V}' \cdot \vec{\nabla} \right) \langle T \rangle - \left\langle \left(T' \bar{V}' \cdot \vec{\nabla} \right) \langle T \rangle \right\rangle \right\} \\ - \frac{C_p}{T_r} T' \left\langle \left(\bar{V}' \cdot \vec{\nabla} \right) T' \right\rangle \end{array} \right] - \left[\begin{array}{l} \left(\langle \omega \rangle \alpha' + \omega' \langle \alpha \rangle \right) \\ - \omega' \alpha_r \end{array} \right] + \frac{1}{T_r} \left(T' \langle Q \rangle + \langle T - T_r \rangle Q' \right) \\
\frac{\partial A}{\partial t} &= - \left(\bar{V} \cdot \vec{\nabla} \right) A - \omega (\alpha - \alpha_r) + \left(\frac{T}{T_r} - 1 \right) Q
\end{aligned} \tag{1.31}$$

(see “Appendix 13” for details).

With,

$$\omega \alpha = \vec{V}_h \cdot \vec{\nabla}_h \phi - \vec{V} \cdot \vec{\nabla} \phi \tag{1.32}$$

1.2.6 Summary of the climate energy budget

The set of atmospheric energetics equations suitable for climate studies is summarized in Fig. 1-1. Boxes represents reservoirs and arrows indicate conversion terms (or physical processes) acting on the corresponding reservoir as sources/sinks of energy. At this stage, the direction of the arrows is arbitrary and only reflects the choice of sign used in writing the equations (16) to (19). According to these equations, positive (negative) terms are represented by inward (outward) pointing arrows. Terms who belong to two different equations, are called conversion terms because they allow a direct energy exchange between them. This is the case of C_A and C_K connecting respectively A_M to A_E and K_M to K_E . In the Lorenz energy cycle, which is a global energy cycle, terms C_{MA} and C_{EA} connect respectively A_M to K_M and A_E to K_E . However, in a limited area domain, fluxes of geopotential heights ($F_{\phi M}$ and $F_{\phi E}$) acting on the lateral boundaries, make inroads into direct conversion from available enthalpy to kinetic energy through baroclinic processes. Therefore, C_{MK} (C_{EK}) expresses only the fraction of A_M (A_E) convertible into K_M (K_E) due to external forces; the difference being lost by geopotential heights fluxes.

According to the dynamic and thermodynamic equations (1.11) and (1.12), frictional terms dissipate kinetic energy and diabatic heating terms generate available enthalpy. Therefore, GM and GE are physically responsible of the generation of available enthalpy and DM and DE are responsible of the destruction of kinetic energy. Finally, terms starting by F and H in our cycle, named boundaries fluxes terms, exist because of our open lateral boundaries. In the cases of close atmospherics domain like Lorenz's global energy cycle, they will vanish.

To conclude, the difference between our cycle and Lorenz's only lies in the presence of boundaries fluxes terms. In a close system, there is no divergence and F and H will become 0. Therefore, our cycle will become exactly equal to Lorenz's one. This gives us most confidence to introduce our last energy cycle suitable for transient-eddies.

1.2.7 Summary of storms energy budget

The set of atmospheric energetics equations suitable for storms studies is summarized in Fig. 1-2. This diagram is a combination of Equations (1.24) to (1.27). This cycle seems quite similar to the climate cycle, only terms differ. The only exceptions lie in the presence of an extra conversion

term “ j ”. In fact, this term is a third order term (made of three time-variability variable) appearing during the theoretical development, but negligible in practice. Moreover, this cycle gives us the theoretical opportunity to combine F and H boundaries fluxes terms acting on energy reservoirs in only one term “ f ”.

1.3 MODEL CONFIGURATION

1.3.1 Simulation condition and domain

Three years exhibiting substantial difference in rainfall amounts during the West African Monsoon will be studied: 1997 (dry), 1999 (rainy) and 2006 (near normal). A regional climate model (RCM) simulation driven by reanalysis will provide high-resolution self-coherent fields required by the detailed energetic calculations.

The employed RCM is a developmental version of the sixth-generation Canadian Regional Climate Model (CRCM6), which is being currently developed at *Centre pour l'étude et la simulation du climat à l'échelle régionale* of l'Université du Québec à Montréal (ESCER Centre, UQAM). CRCM6 is based on an adapted version of the Global Environmental Multiscale model version 5 (GEM5) from the Meteorological Service of Canada (MSC-ECCC). GEM5 benefits from a major update to the package of physical parameterizations used in Canadian operational Numerical Weather Prediction (NWP), resulting in an improvement of the global energy budget and a reduced sensitivity to the vertical resolution (McTaggart - Cowan *et al.*, 2019). Of the several horizontal grid options available in GEM5, CRCM6 uses the limited-area grid with a rotated latitude-longitude projection. In the vertical, a hybrid hydrostatic pressure coordinate is used (Laprise, 1992) with a staggered Charney-Phillips grid (Milbrandt et Morrison, 2016).

The subgrid-scale physical parameterization is identical to that used in the operational Canadian NWP Regional Dynamical Prediction System (RDPS), including the ISBA land-surface scheme; the thermodynamical column Flake module was however added to account for lakes. With respect to the operational NWP RDPS version, the following additional changes were made for our African monsoon simulations. The grid mesh was coarsened from 0.09° to 0.11° and the uppermost computational level was lowered from 0.1 hPa to 10 hPa. In order to reduce what was

perceived as excessive dissipation, the off-centring coefficient of the semi-implicit scheme was reduced from 0.6 to 0.55, and the horizontal diffusion in ∇^4 was changed to a ∇^6 with a damping coefficient reduced from 0.1 to 0.04.

CRCM6 was integrated over a domain comprising the whole West Africa, with a southwest extension to capture Bermuda-Azores anticyclone effect. The domain goes from 37°W to 31°E in longitude and from 12°S to 25°N in latitude (Figure 1-3). The entire computational domain has 660*380 points, including a 10-grid-point wide semi-Lagrangian halo and a 10-grid-point wide sponge zone around the 620*340 points free domain, on a horizontal grid of 0.11°. In the vertical, 71 terrain-following levels were used, with a top level at 10 hPa. The timestep is 10 min and outputs are available hourly. CRCM6 atmospheric lateral boundaries conditions and sea surface temperatures came from the European Centre for Medium range Weather Forecasting (ECMWF) ERA5 reanalysis (Hersbach *et al.*, 2020), which is based on the Integrated Forecasting System (IFS). ERA5 data is available on hourly basis on a horizontal grid of 0.25°. In the vertical, there are 37 pressure levels with a finer resolution near the surface. To facilitate the analysis and comparison, the CRCM6 outputs have been interpolated on the same pressure levels as ERA5.

CRCM6 simulations covered three sets of six consecutive months (May to October) for 1997, 1999 and 2006. The month of April being consider as spin-up.

1.3.2 West African climate overview

Our goal in this section is not to prove the ability of our model to reproduce the main features of the geographical distribution and seasonal cycle of temperature and precipitation, the diurnal cycle of precipitation, and the WAM. This work has already been done using a hindcast RCM simulation that followed the CORDEX experimental protocol (Hernández-Díaz *et al.*, 2013) and for future projections using boundary conditions from a Coupled Global Climate Model (Hernández-Díaz *et al.*, 2017).

In the following, we here present an overview o the intra-seasonal regime over West Africa during three contrasting years (1997 / dry, 1999 / rainy and 2006 / near normal) from May to September. This description is fundamental to understand the coming energetics approach. The

CRCM6 simulated results are compared to ERA5 reanalyses and gridded analyses of observations such as CRU and UDEL. May and June have been added to the classical June to September (JAS) monsoon season to capture the pre-onset of the summer monsoon (Sultan *et al.*, 2003).

Figure 1-4 shows seasonal-mean precipitation fields for each of the three years. Precipitation is an important surface variable in West Africa because of its impact on water resources and food production. In West Africa, precipitation above 4 mm/day is confined between the equator and 15°N. CRCM6 overestimates the intensity and the northernmost position of precipitation, but in the south, the geographical representation is quite similar to ERA5. There are three precipitation maxima (above 16 mm/day) in ERA5 and CRCM6 occurring in Cameroon and Nigeria highlands, West African coast and Cape Verde islands. In 1997 (dry), the rainbelt is narrower than in other years, even if precipitation between the equator and 15°N remains high; this confirms that the width of the rainbelt is a better indicator of the monsoon intensity than the annual mean precipitation in the rainbelt. When compared to CRU and UDEL gridded analyses, the CRCM6 exhibits a smaller precipitation excess over the continent than when compared to ERA5 (Figure S.1 in Supplementary material).

Figure 1-5 shows seasonal mean 2-m surface temperature and mean sea level pressure fields. The presence of hot Sahara in the north of the domain reverses the meridional temperature gradient over West Africa, with lower temperatures located near the Gulf of Guinea and higher temperatures in the Western Sahara (close to the Saharan heat low). In the Gulf of Guinea, the temperature is highest north of the equator (because of the summer solstice season) and decreases southward. CRCM6 simulation is cooler than ERA5 over the Sahara; we note that ERA5 is warmer than the gridded analyses of observations CRU and UDEL, and hence CRCM6 is closer to the CRU and UDEL databases over Western Africa (Figure S.2 in Supplementary material).

Mean sea level pressure contours superimposed in ERA5 and CRCM6 surface temperature (Fig. 1-5) show that lower pressures (below 1012 hPa) are located over the continent, especially in the western Sahara. This West African heat low (WAHL) is a key element of the WAM system (Lavaysse *et al.*, 2009). In the lower troposphere, the cyclonic circulation associated with the WAHL tends to increase both the southwesterly monsoon flow along its eastern flank and the

north-easterly Harmattan flow along its western flank (Parker, D. J. *et al.*, 2005). Over the ocean, Bermuda-Azores and South Atlantic anticyclones dominate respectively on the northern and southern sides of the equator.

Figure 1-6 shows the seasonal-mean vertical cross section of relative humidity and vertical velocity fields. Both ERA5 reanalysis and CRCM6 simulation show more than 90% relative humidity at the surface from the Gulf of Guinea to 13°N, which coincides with the rainbelt presented in figure 1-4. The 90% isohume (line of constant relative humidity) extends further north in 1999 (wet year) than in 1997 (dry year), especially in ERA5, which is in agreement with precipitation above 4 mm/day (yellow color) in figure 1-4 south of the coast in the Gulf of Guinea. The CRCM6 simulation succeeds rather well in reproducing the vertical distribution of relative humidity in West Africa.

The upper tropospheric maximum vertical velocity near 10°N corresponds to the upward branch of the Hadley cell that transports humidity in the high troposphere. The 1999 (moist year) vertical velocity is stronger than for the other two years. The Hadley cell is distinct from the lower tropospheric vertical velocity cell over the WAHL by its vertical extension. Compared to ERA5, the CRCM6 simulation appears to overestimate the vertical velocity in both Hadley cell and WAHL, but it succeeds in distinguishing its latitudinal limits and vertical extension.

Figure 1-7 shows the seasonal-mean vertical cross section of zonal wind. The African Easterly Jet (AEJ) is an important feature of the West African climate. According to the thermal wind relationship, the AEJ is a response to the low-level meridional temperature gradient that forms over West Africa in summer as a result of strong meridional soil moisture gradients (Cook, 1999). Therefore, AEJ axis is an indicator of the strong baroclinic zone separating moist and relatively colder Gulf of Guinea regions from dry and hot Saharan regions. Figure 1-7 shows that mid-tropospheric AEJ position and intensity are well reproduced in the CRCM6 simulation. AEJ is overall less intense and located further south in 1997 (dry year) compared to 1999 and 2006. The CRCM6 simulation overestimates the upper-level Tropical Easterly Jet (TEJ) intensity. While the TEJ is significantly correlated with summer Sahel rainfall, its relationship on synoptic to intraseasonal time scales is unclear (Lemburg *et al.*, 2019); hence despite the obvious connection between AEJ and TEJ, this study will focus on the AEJ level.

Figure 1-8 shows seasonal-mean vertical cross-section of meridional wind in 1997, 1999 and 2006. Southerly monsoon flow and northerly Harmattan flow converge in the intertropical front (ITF). ITF seasonal-mean position indicates the penetration of the moist monsoonal southwesterlies onto the continent. The CRCM6 simulation reproduces quite well ITF and the penetration of the monsoon flow in the continent. During the dry year (1997), the monsoonal depth appears thinner and therefore, there is less precipitable water available in the Sahel.

These results show that the CRCM6 simulation succeeds in reproducing the overall features of the West African seasonal meteorological condition. This allows a certain level of confidence in the energetics calculations performed on the CRCM6 simulated fields in the following section.

1.4 APPLICATION OF THE CLIMATE CYCLE THE WEST AFRICAN MONSOON

We now proceed to study the energy cycle climatology, in order to study the intra-seasonal variability of the WAM to unravel the dynamical and physical processes contributing to maintaining the summer West African climate. Following (6), $E_C = E_M + E_E$, only contributions associated with the time-mean variables and with variance of time deviations (transient eddies) are relevant. The equations resulting from these contributions are linked together through an energy cycle illustrated in Fig. 1-9. Boxes represent various energy reservoirs and arrows indicate energy conversions between the reservoirs, generation and dissipations, and transfers across the domain's lateral boundaries. All terms are horizontally averaged over the sub-domain shown in Fig. 1-3 and vertically integrated from the surface to 600 hPa, and time averaged over the period from May to September, for the years of 1997, 1999 and 2006. The choice of the vertical extension (600 hPa) was made in order to focus attention on primary processes affecting the WAM. A glance at Fig. 1-9 reveals that the energy reservoir AM is two orders of magnitude larger than the other reservoirs. This is due to the effect of the mean stratification of the atmosphere contained in AM (see NL13's section 6 for details). Then to show terms containing in AM with terms of lesser magnitude order on the same plots, we will multiply them in most of coming figures by a damping factor (1/10, 1/20, 1/50 or 1/200). On the other hand, both kinetic

energy reservoirs K_E and K_M have the same magnitude, suggesting a transient-eddy activity as important as the time-mean for this region of the globe, unlike the case in mid-latitudes. Finally, AE is the smallest energy reservoir, confirming smaller temperature variations observed in the tropics compared to higher latitudes ($\sim 3 \cdot 10^5$ J/s, (Clément *et al.*, 2017)).

Flux terms (represented by arrows) can be classified in three main groups as follows:

Terms responsible of the generation of enthalpy by diabatic processes (G_M , G_E) and dissipation of kinetic energy by stress at the surface (D_M and D_E);

Terms responsible for conversion of energy between reservoirs (C_A , C_K , C_{MA} , C_{MK} , C_{EA} and C_{EK});

Terms resulting from the limited-area lateral boundaries and therefore non existing in a global energy cycle (I_{AB} , F_{AM} , H_{AM} , F_{KM} , H_{KM} , F_{AE} , H_{AE} , F_{KE} , H_{KE} , $F_{\phi M}$ and $F_{\phi E}$).

In addition to the four energy reservoirs, Fig. 1-9 also shows two nodes that correspond to the identity equations (1.20) and (1.21). As noted, when the budget is integrated over the entire atmosphere, the boundary fluxes $F_{\phi M}$ and $F_{\phi E}$ vanish, and then $C_{MA}=C_{MK}$ and $C_{EA}=C_{EK}$. This representation using nodes parallels that used by ((Marquet, 2003a); Fig. 12). It differs from the diagram of ((Arnault et Roux, 2009); Fig.13) who chose to assimilate the node within the enthalpy and (NL13; Fig. 1) who chose to assimilate the node within the kinetic energy. The advantage of the present representation is to clearly show the contribution of boundary fluxes to the node, rather than assimilate it with the boundary fluxes of enthalpy or kinetic energy.

It is important to note that terms responsible of the generation of available enthalpy by diabatic processes and dissipation of kinetic energy by stress at the surface weren't available in ERA5; these were computed as residual of primitive equations (1.11) and (1.12). These values in Fig. 1-9 are therefore for information only, but analyses will be mainly based on CRCM6 outputs.

In the following sections, we will analyse each reservoir and flux term acting on the West African climate during the summer season, in order to understand the physical meaning of all values appearing in Fig. 1-9.

1.4.1 Energy reservoirs

Vertical-latitudinal cross section and vertically integrated (from the surface to 600 hPa) maps of the four energy reservoirs will be shown and discussed in this section.

A_M

Fig. 1-10a shows seasonal- and longitudinal-mean vertical-latitudinal cross section of A_M . Values are influenced by the choice of the reference level, where it is equal to zero. In this paper, the reference level has been chosen at 600 hPa to focus on the lower troposphere. Then, there is a gradual increase of A_M away from the reference level. In low levels, there is a maximum of A_M located north of 15°N as a result of high surface temperatures over the Sahara. Fig. 1-11a shows a horizontal map of the A_M field. In the Sahara region where lies the thermal depression, large vertically integrated (from the surface to 600 hPa) A_M values are found, reflecting the high surface temperatures and large lapse rate characteristic of a dry atmosphere. The largest values of A_M over the Sahara occur during the wet year in 1999, confirming the link between high temperatures in the Saharan boundary layer and the WAM system in general (Lavaysse *et al.*, 2010). South of 10°N, A_M values are much smaller, reflecting the smaller lapse rate characteristic of a moist atmosphere. To sum up, the Sahara Desert region represents the main available enthalpy reservoir associated with the time-mean state in West Africa.

A_E

The seasonal- and longitudinal-mean vertical-latitudinal cross section of A_E is shown in Fig. 1-10b (note the different scale with A_M as mentioned above). A_E is maximum near the surface in northern latitudes, negligible in upper levels, and exhibits substantial interannual variability. It represents the atmospheric layer, where temperature variations are maximum during the season. During the dry year (1997), the maximum of A_E is located north of 20°N and A_E 's vertical penetration is weaker in the Sahel. This is confirmed in Fig. 1-9 by A_E 's lowest values in the dry year 1997 and largest values in the wet year 1999. In wetter years, the transient-eddy available enthalpy extends further south. Fig. 1-11b shows vertically integrated A_E map (note once again the different scale among compared to A_M , which is two orders of magnitude higher). There is a noteworthy land-sea contrast in the magnitude of A_E , with in general lower values over the ocean

and larger values over the continent. A_E reflects temperature fluctuations caused by low-level monsoonal winds transporting cool air northward from the Gulf of Guinea and Harmattan winds transporting hot air southward from the Sahara. Over the continent, there is a northward shift of A_E in drier years. During the wettest year (1999), there is a secondary maximum of A_E over the central Niger, probably reflecting the passage of intense AEWs. There is another maximum noted in all three years near the border between Chad and Sudan, where AEW's often originate (Mekonnen *et al.*, 2006).

K_E

Fig. 1-10c shows seasonal- and longitudinal-mean vertical-latitudinal cross section of K_E . Two maxima are located around the tropopause, corresponding to the equatorial edge of subtropical jets, and another maximum around 650 hPa and 10°N corresponding to the AEJ. The TEJ is not visible due to his lowest variance compared to subtropical jets. Both subtropical jets are strongest during the dry year and weakest during wetter year. Fig. 1-11c shows vertically integrated (from the surface to 600 hPa) K_E field. Over the continent, maximum values near 10°N corresponds to the AEJ, which is a response to the strong meridional temperature gradient at the surface. This maximum originates to South Sudan and intensifies westward off the west coast, especially during wetter years. It is interesting to note like it was the case with A_E , that maximum values in the continent start from Sudan, where AEW's often originate (Mekonnen *et al.*, 2006). In the West coast, there is a mixing between those values and systems coming from midlatitudes. This supply of energy is important to for the development of systems into tropical cyclones in the Atlantic. Close to the equator, low values characteristics of doldrums are observed.

K_M

Fig. 1-10d shows seasonal- and longitudinal-mean vertical-latitudinal cross section of K_M . Maximum time-mean energy is associates with the upper levels jet streams. At 600 hPa, there is the AEJ, which is much intense and with a larger latitudinal extend during wetter years (1999 and 2006). At 200 hPa, close to the tropopause, there is the TEJ in the center of the domain, which is clearly connected with the AEJ. The TEJ is particularly intense during the wetter year (1999) and would have obviously played a huge role in the development of the AEJ and precipitations;

however, this role has been omitted of this work and will be discussed later. The other two maxima, south of 5°S and north of 15°N , are related to southern and northern hemisphere subtropical jets. Fig. 1-11d shows maps of vertically integrated (from the surface to 600 hPa) K_M field. Maximum values in the continent are located around 15°N , in the trajectory of the AEJ and are somewhat larger during the wet year of 1999. K_M magnitude increases westward from the coast to reach a maximum over the Atlantic. In 1999, K_E maximum west of Cape Verde Islands confirms the intense Atlantic hurricane season (Lawrence *et al.*, 2001), with five Category 4 hurricanes – the 3rd largest number recorded in a single season in the Atlantic basin after 2005 and 2020.

Conversion terms

In this section, we analyse terms responsible for conversion between energy reservoirs.

C_A converts available enthalpy energy from time-mean A_M to time-variability A_E . In general, in a long time-scale, the time-mean feeds the eddies. Therefore, the conversion goes from A_M to A_E . C_A is dominated by its vertical component due the strong vertical temperature variations compared to horizontal temperature gradients in the tropical atmosphere. Fig. 1-12a showing seasonal- and longitudinal-mean vertical-latitudinal cross section of C_A , highlights two distinct maxima. One maximum is located near 12°N and extends up to the tropopause; it reflects the upward branch of the Hadley cell with deep moist convection. The other maximum extends from the surface up to 600 hPa North from the Sahel; it reflects the shallow dry convection that develops in the Sahara due to high insolation. As to be expected, the latitudinal extend and intensity of the deep convection is larger during the wetter year (1999) than in other years, confirming that in the wet years, the rainbelt is markedly more intense and its core covers a much greater latitudinal band (Nicholson, 2008). The dry convection shows low interannual variability. Fig. 1-13a shows a map of vertically integrated (from the surface to 600 hPa) C_A field. Positive values occur over most of the domain, confirming that A_M is converted to A_E (and not vice versa), with maximum conversion occurring over the Sahara. Note that the presence of stationary local hotspots for all the three years suggests a numerical artefact due to the computation of the vertical motion near the surface.

C_{EA} is the flux of A_E that is offered for conversion into K_E , through rising (sinking) of warm (cold) anomalies in the atmosphere. Fig. 1-12b shows seasonal- and longitudinal-mean vertical-latitudinal cross section of C_{EA} . This field is quite similar to C_A , which should not be surprising given that it is proportional to C_A 's vertical component (see “*Appendix 14*” for details).

In Fig. 1-9 we see that the node located between A_E and K_E exhibits a very small contribution from boundary flux $F_{\phi E}$, which means that there is little overall pressure work acting at the lateral boundaries for transient eddies; and hence C_{EA} is nearly equal to C_{EK} . This implies that the loss of A_E contributes almost entirely to the gain in K_E , when integrated over the limited-area domain.

Physically, C_{EK} represents the horizontal ageostrophic term expressing any local imbalances between time-variability pressure gradient and time-variability Coriolis force. Fig. 1-12c shows seasonal- and longitudinal-mean vertical-latitudinal cross section of C_{EK} . Despite the fact that C_{EA} is nearly equal to C_{EK} when integrated over the limited-area domain, its vertical-latitudinal cross-sections exhibit notable differences (Figs. 12 b and c). The large maximum C_{EK} located in the low levels north of 5° N reflects the fluctuations of the mass convergence toward the fluctuating SHL. Two secondary maxima are located on both sides of the Saharan desert, at around 600 hPa. This reflects the well-known structure of the Saharan circulation (Thorncroft, C. D. *et al.*, 2011), where mass converges into the near-surface low, ascends, and diverges out of the lower mid-tropospheric high in an ageostrophic overturning circulation; this shallow overturning, extends across the entire Sahara desert (Shekhar et Boos, 2017). Fig. 1-13c shows a map of vertically integrated (from the surface to 600 hPa) C_{EK} field; we can see that C_{EA} is nearly equal to C_{EK} .

C_K is the conversion flux between K_M and K_E . A positive value of C_K implies a barotropic conversion from the mean state to transient eddies. Fig. 1-12d shows seasonal- and longitudinal-mean vertical-latitudinal cross section of C_K . In the lower part of the troposphere, C_K is mostly positive with two distinct maxima. The strongest one is located near 800 hPa and 12° N, below the AEJ level; it therefore shows that the AEJ plays a key role in the development and maintenance of AEWs. The second weaker maximum is just above the Sahara's surface, north of 15° N, related to the heat low during the summer season (Lavaysse *et al.*, 2016). Other maxima occurring near the tropopause are related to transient eddies around subtropical jets in the southern and northern

hemispheres; these will not be considered in the computation of our energy budget. Fig. 1-12d shows vertically integrated (from the surface to 600 hPa) C_K map. Values are positive over almost all the domain, with maximum values in the West African coast in the trajectory of AEWs and in the Sahara, as showed in vertical cross section maps.

We note in Fig. 1-9 that the lowest values of transient-eddy energies (A_E and K_E) and conversion fluxes (C_{EK} , C_{EA} and C_K) occur in the dry year (1997), while largest values occur in the wet year (1999), as a distinct characteristic of the weaker and stronger AEW's activity during those years, respectively.

C_{MK} is the energy flux affecting the time-mean kinetic energy K_M from available enthalpy A_M . Physically, C_{MK} represents the horizontal ageostrophic term expressing any local imbalances between the time-mean pressure gradient and Coriolis force. Fig. 1-12e shows seasonal- and longitudinal-mean vertical-latitudinal cross section of C_{MK} . Positive conversions (meaning contribution to increase K_M) occur near the surface, in mid levels and upper levels. Surface maximum are related to the monsoonal flow activity, with southerlies bringing humidity in the Sahel. Midlevel and upper maximum are associated with the ageostrophic circulations around respectively the AEJ, the TEJ and midlatitudes jets. It is interesting to see the similarity between the production of the time-mean and the time variability production of kinetic through respectively C_{MK} and C_{EK} (Fig. 1-9); this confirms the relevance of the time-mean ageostrophic circulation to understand the variability of the jet and how it is maintained (Cook, 1999). Fig. 1-13e shows vertically integrated C_{MK} map; due to the vertical integration limits from the surface to 600 hPa, only the AEJ ageostrophic circulation appears. There is a maximum conversion during the wetter years, with a larger latitudinal extend around the AEJ mean position at 15°N.

We note in Fig. 1-9 that in the node between A_M and K_M , the boundary flux $F_{\phi M}$ is very large due to the increase of the geopotentials with height as a consequence of the stratification of the atmosphere. This means that only a fraction of the conversion C_{MA} from time-mean available enthalpy A_M will contribute to increase the time-mean kinetic energy K_M through C_{MK} .

C_{MA} converts A_M into K_M by upward transport of warm and humid air from the surface to the top of the troposphere. As shown in Fig. 1-12f (note the different scale of this panel as mentioned

above to fit with other terms), this phenomenon is particularly strong in the ITCZ. Positive values from 3°N to 17°N delimitate the ascending branch of the Hadley cell, while negative values indicate the subsiding branch in southern and northern boundaries of the domain. North of 17°N there is a shallow meridional overturning cell – as described in (Nicholson, 2009), with positive C_{MA} values due to the upward motion of warm and dry air in the thermal depression, and negative C_{MA} values due to the descending branch of the Hadley cell. Fig. 1-13f shows vertically integrated (from the surface to 600 hPa) C_{MA} map (note again the different scale of this panel). Over the continent, the calculation of C_{MA} is challenging, due to the presence of topography, which results in excessively large (unrealistic) fluctuations of alternating sign. Over the ocean, the Hadley cell contributes to positive values; it is narrower in 1997 compared to wetter years. We remind however that because the boundary flux $F_{\phi M}$ is very large (Fig. 1-9), only a very small fraction of the conversion C_{MA} will contribute to C_{MK} increasing K_M .

1.4.2 Energy generation and dissipation terms

We now present an overview of main diabatic heating components that contribute to the generation of available enthalpy.

Fig. 1-9 shows that, as expected, there is diabatic generation of available enthalpy (G_M into A_M for the time mean and G_E into A_E for transient eddies) and dissipation of kinetic energy (D_M out of K_M for the time mean and D_E out of K_E for transient eddies), when integrated over the diagnostic domain.

Because of the definition of G_M in (18), the diabatic generation of A_M will be of the same sign as the diabatic heating rate Q below the reference level and of different sign above. G_M will be equal to zero at the reference level. Therefore, a correct physical interpretation of G_M will depend on our knowledges of terms contributing the total diabatic heating Q . That's why Figs 1-16 and 1-17 are added to understand G_M . Fig. 1-14a shows seasonal and longitudinal mean vertical-latitudinal cross section of G_M (note the different scale of this panel as mentioned above to fit with other terms). There is generation of A_M below 800 hPa north of the equator, with a maximum over the Sahara Desert, mainly due to sensible surface heat flux and vertical diffusion (Fig. 1-16d). South of the equator and around 900 hPa, there is a dissipation of A_M as a consequence of the radiative

cooling (Fig. 1-16c). The dissipation of A_M at the tropopause near 10°N is a consequence of warming by condensation and convection (Fig. 1-16a and b). Fig. 1-15a shows vertically integrated (below 600 hPa) G_M map. Over the continent, positive values over the Sahara (and to a lesser extent in the southern hemisphere) are due to sensible surface heat flux and vertical diffusion (Fig. 1-17d), whereas positive values in the southern West Africa is the sum of deep convection and latent heat release. The maximum generation of A_M over the ocean off the West African coast is mostly the consequence of latent heat release (Fig. 1-17b) associated with precipitation (Fig. 4a).

Fig. 1-14b shows seasonal- and longitudinal-mean vertical-latitudinal cross section of G_E , the generation of A_E , which reflects the covariance of diabatic heating and temperature fluctuations. The low-level maximum G_E , north of 5°N , results from the positive covariance of perturbations of temperature and diabatic heating by radiation (Fig. 1-16c) and surface sensible heat flux and vertical diffusion of heat (Fig. 1-16d). In the upper troposphere, the maximum of G_E is located over the Sahel, where covariance of perturbations of temperature and latent heat release (Fig. 1-16b) is highest. Fig. 1-15b shows the vertically integrated (below 600 hPa) G_E map. In West Africa, the maximum of G_E is located over the Sahara, mostly as a result of the surface sensible heat flux and vertical diffusion of heat (Fig. 1-17d). Due to the integration upper limit, the deep convection observed above 600 hPa in (Fig. 1-16b) doesn't contribute.

Fig. 1-14c shows seasonal- and longitudinal-mean vertical-latitudinal cross section of D_E , the dissipation of K_E through stress at the surface. Largest energy dissipation is found north 8°N as the result of covariance of perturbations of horizontal winds and surface stress. Fig. 1-15c shows vertically integrated D_E map. D_E is particularly large north of 13°N , in the Sahara, where perturbations of surface stress and low-levels winds associated to the heat low are maximum. South of 15°N , there is another maximum of D_E in the Cameroonian and Nigerian highlands.

Fig. 1-14d shows seasonal- and longitudinal-mean vertical-latitudinal cross section of D_M , the dissipation of K_M through stress at the surface. Maximum D_M values are found in the low levels and their position coincides with low-level monsoon winds shown in Fig. 8. This suggests that friction acting upon monsoon winds contribute to the dissipation of K_M . Fig. 1-15d shows

vertically integrated D_M map. No clear maximum is noted, because of the lower magnitude of D_M compared to D_E .

1.4.3 Boundaries fluxes terms

In a regional energy budget, energy fluxes across the domain perimeter must also be taken into account. Despite the use of the 600 hPa as upper diagnostic domain limit, the boundary fluxes are dominated by horizontal transport rather than vertical one (not shown). Fig. 1-9 shows that the largest boundary fluxes are I_{AB} into A_M and $F_{\phi M}$ out of the node between A_M and K_M . In fact, these very large values are linked with similarly large C_{MA} conversion flux values. Hence this part of the energy cycle diagram is of little interest because boundary fluxes largely dominate over processes occurring within the domain. All other boundary flux terms are much smaller than conversion or generation/dissipation terms, and hence will not be discussed here.

1.4.4 Vertical profiles

Fig. 1-18 shows the vertical profiles of time- (May-September) and domain- (20°W – 20°E ; 0 – 20°N) averaged values of the tendency equations of A_M , A_E , K_E and K_M . Colored lines represent individual terms acting upon various energy reservoirs and black lines represent the residual, the sum of the contributions to reservoirs.

Fig. 1-18a shows the various contributions to the time tendency of A_M . Contributions I_{AB} and C_{MA} dominate the energy budget, as mentioned before, confirming the energy equilibrium shown in Fig. 1-9. During wetter years, conversion terms I_{AB} and C_{MA} are larger as the consequence of a more intense Hadley cell activity. The contribution of G_E is positive in the low levels due to the covariance of surface sensible heat flux and temperature. The small positive residual below 950 hPa suggests an imbalance in the budget calculation due to topography.

Fig. 1-18b shows the various contributions to the time tendency of A_E . The mean equilibrium for A_E appears to result from a compensation, with C_A and G_E adding up to feed C_{EA} . Conversion terms C_A and C_{EA} , and the generation term G_E , dominate the A_E budget on average over the domain, as shown in Fig. 1-9, and boundaries fluxes terms are negligible. Hence, C_A and G_E add up to feed C_{EA} . The positive residual in the boundary layer reveals again the difficulty in closing

the energy budget. The interannual variability is larger in the upper levels, with conversion contributions being stronger during wet years.

Fig. 1-18c shows the various contributions to the time tendency of K_M . Compensation occurs between different contributions, depending upon level. Below 850 hPa, the time-mean ageostrophic circulation source term C_{MK} counterbalances the frictional term D_M as to be expected with wind convergence in low pressures. Between 800 and 400 hPa, the barotropic conversion C_K also contributes to the balance between C_{MK} and D_M , with some contribution from the boundary term H_{KM} . During wetter years, various contributions to the local tendency of K_M increase in agreement with the AEJ intensity noted in Figs. 10d and 11d.

Fig. 1-18d shows the various contributions to the time tendency of K_E . In the boundary layer, the main balance is between the ageostrophic circulation source term C_{EK} and the frictional sink term D_M , reflecting wind convergence in low pressures. Below the AEJ level, the time-variability ageostrophic conversion term C_{EK} and the barotropic conversion term C_K are the main source of production of K_E and therefore contribute to the growth and maintenance of the AEWs, whereas the dissipative term D_E acts as the main source of dissipation of time-variability kinetic energy. There is a low interannual variability between wet and dry years. We note that the time tendency, which should nearly vanish, increases slightly gradually from the ground, as a result of inaccuracies in the calculation of the several contributions that are summed up.

1.5 SUMMARY AND CONCLUSIONS

In this study, our first motivation was to develop an atmospheric energetics framework suitable for both weather and climate studies over limited-area domains. This is accomplished by adapting to climate energetic the equations originally developed by NL3 for the study of inter-member variability, and by revising completely the framework proposed by (Clément *et al.*, 2017) for the study of weather systems energetics. The main advantage of this approach is to allow retrieving the total kinetic energy and enthalpy equations by summing climate and weather tendency equations.

The second motivation of this paper was to apply the developed atmospheric climate energetics equations over West Africa, to improve our knowledge on mechanisms responsible of the rainfall interannual variability. To reach this goal, three contrasting years have been simulated (1997/dry, 1999/wet and 2006/moderate) using the sixth-generation Regional Climate Model (CRCM6), driven by the new ERA5 reanalyses. The simulation succeeds in reproducing the overall distribution of the main physical variables describing the West African intra-seasonal variability. Our study used the CRCM6 to benefit from enhanced resolution and variables unavailable in ERA5.

For the study of the WAM atmospheric energetics, the energy cycle developed here is quite similar to the one used by (Nikiéma *et al.*, 2018) for the energy budget. A major difference is the addition of “nodes” corresponding to ageostrophic circulation terms, in time-mean and time-variability, $F_{\phi M}$ and $F_{\phi E}$ respectively. This approach allows us to make a distinction between fluxes terms not highlighting a meaningful physical process and others that act on different spatial and temporal scales of the WAM. In Fig. 1-9 was presented domain-averaged and vertically integrated values of the energy reservoirs, energy conversion and boundary fluxes terms.

In our limited-area domain, A_M dominates other energy reservoirs. In this study, the introduction of a node representing the boundary flux $F_{\phi M}$ shows that most of A_M generated by the conversion from the pressure-dependent part of available enthalpy I_{AB} is dissipated by time-mean pressure

work at the lateral boundaries. Even if terms involved in this conversion are very large, they are not meaningful for the understanding of the West African climate. For all the other terms, their magnitude is an indicator of the intensity of the physical processes in the domain of interest.

The A_M reservoir dominates the other energy reservoirs in the domain. Its magnitude reflects the high surface temperatures and lapse rate characteristic of a dry atmosphere. Most of A_M is generated by the boundary contribution I_{AB} and compensated by conversion C_{MA} towards K_M . The introduction of a node between A_M and K_M however revealed that the boundary flux $F_{\phi M}$ due to pressure work at the lateral boundary exports most of the C_{MA} contribution, and hence only a very small fraction C_{MK} contributes to K_M . Even if terms I_{AB} and $F_{\phi M}$ are very large, they are not meaningful for the understanding of the West African monsoon. For all the other terms, their magnitude is an indicator of the intensity of the physical processes in the domain of interest. We note that the time-averaged diabatic generation G_M contributed to A_M . In fine, a small part of the conversions from A_M contributes to A_E and K_M .

This latter conversion is the primary source of production of A_E , while the generation of A_E by diabatic processes G_E is the secondary source. Due to small contribution from boundary flux $F_{\phi E}$, the loss of A_E contributes almost entirely to the gain in K_E . This process, also named the baroclinic energy conversion is maximum in wetter years, contributes to the generation of AEWs and therefore, to precipitations in West Africa. The secondary source of generation of K_E is the barotropic conversion from K_M . The dissipation of time-variability kinetic energy by frictional forces D_E , acts to dampen the creation of AEW's. Finally, K_M is generated by the horizontal ageostrophic term expressing any local imbalances between the time-mean pressure gradient and Coriolis force, while the barotropic conversion term C_K and the time-mean kinetic energy dissipative term D_M acts as sink of energy.

Atmospheric energetic equations are powerful tools to evaluate a wide spectrum of temporal scales, in particular in regions with lack of long-term in situ data such as West Africa. Forthcoming works will focus on the study the life cycle of African Easterly Waves (AEW), aiming to understand mechanisms responsible of the generation, maintenance and dissipation of an AEW using the high-resolution CRCM6 driven by ERA5 and making use of equations developed for the time variations associated with weather systems.

Acknowledgements: This research was funded by the Discovery Grant program of the Natural Sciences and Engineering Research Council of Canada (NSERC). Computations were made on the Calcul Québec-Compute Canada supercomputer, whose operation is funded by the Canada Foundation for Innovation (CFI), Québec’s Ministère de l’Économie et de l’Innovation and the Fonds de recherche du Québec-Nature et technologies (FRQ-NT). The authors are grateful for the ERA5 global reanalysis from ECMWF. The authors are deeply indebted to Katja Winger and François Roberge for their essential support in the use of the CRCM6/GEM5, as well as for downloading and preparing ERA5 reanalyses.

1.6 Appendix

1.6.1 Appendix A1: Kinetic energy equation

The total kinetic energy equation is obtained as follows:

$$\begin{aligned}
 \frac{\partial K}{\partial t} &= \frac{1}{2} \frac{\partial (\vec{V}_H^2)}{\partial t} = \vec{V}_H \cdot \frac{\partial \vec{V}_H}{\partial t} \\
 \frac{\partial K}{\partial t} &= \vec{V}_H \cdot \left(-(\vec{V} \cdot \vec{\nabla}) \cdot \vec{V}_H - f \vec{k} \times \vec{V}_H - \vec{\nabla} \phi + \vec{F}_H \right) \\
 \frac{\partial K}{\partial t} &= -(\vec{V} \cdot \vec{\nabla}) K - \vec{V}_h \cdot \vec{\nabla}_h \phi + \vec{V}_h \cdot \vec{F}_h
 \end{aligned} \tag{A1.1}$$

with

$$\begin{aligned}
 \vec{V}_h \cdot (\vec{\nabla}_h \phi) &= \vec{\nabla}_h \cdot (\vec{V}_h \phi) - \phi (\vec{\nabla}_h \cdot \vec{V}_h) \\
 &= \vec{\nabla}_h \cdot (\phi \vec{V}_h) + \phi \frac{\partial \omega}{\partial p} \\
 &= \vec{\nabla}_h \cdot (\phi \vec{V}_h) + \frac{\partial (\phi \omega)}{\partial p} - \omega \frac{\partial \phi}{\partial p} \\
 &= \vec{\nabla} \cdot (\phi \vec{V}) + \omega \alpha
 \end{aligned}$$

1.6.2 Appendix A2: Alternative decompositions of quadratic terms

Depending on the approach chosen to obtain energy equation terms, different Reynolds decomposition methods could be used as follows

$$\langle y'^2 \rangle = \langle (y - \langle y \rangle)^2 \rangle = \langle y^2 \rangle - 2\langle y \rangle \langle y' \rangle + \langle y \rangle^2 = \langle y^2 \rangle - \langle y \rangle^2 \quad (\text{A2.1})$$

$$y^2 - \langle y^2 \rangle = \langle (y + y')^2 \rangle - \langle (y + y')^2 \rangle = y'^2 - \langle y'^2 \rangle + 2\langle y \rangle y' \quad (\text{A2.2})$$

Eq. (A2.1) shows that time-mean equation associated with the time-mean of variables can either be obtained by the variance of deviations $\langle y'^2 \rangle$ or by subtracting the square of the time-mean of the variable $\langle y \rangle^2$ from the time-mean of the square of the variable $\langle y^2 \rangle$. Therefore, we obtain an alternative form of the prognostic equation

$$\begin{aligned} d_t \langle y'^2 \rangle &= d_t \left(\langle y^2 \rangle - \langle y \rangle^2 \right) \\ \Rightarrow \langle y' d_t y' \rangle &= \langle y d_t y \rangle - \langle d_t y \rangle \langle d_t y' \rangle \end{aligned} \quad (\text{A2.3})$$

In this paper we privileged time-mean variables to evaluate climate equations terms. We think that energy budget will be better evaluated if we deal time-mean forms rather than their variability.

Eq. (A2.2) shows that the full energy deviations could either be obtained by subtracting the time-mean of the full total energy $\langle y^2 \rangle$ from the total energy y^2 or by summing its different deviations forms $y'^2 - \langle y'^2 \rangle + 2\langle y \rangle y'$. Therefore, we obtain an alternative form of the prognostic equation

$$\begin{aligned} d_t \langle y^2 - \langle y^2 \rangle \rangle &= d_t \langle y'^2 - \langle y'^2 \rangle \rangle + 2d_t \langle \langle y \rangle y' \rangle \\ \Rightarrow \langle y d_t y - \langle y d_t y \rangle \rangle &= \langle y' d_t y' - \langle y' d_t y' \rangle \rangle + 2 \left(\langle y \rangle d_t y' + y' \langle d_t y \rangle \langle d_t y' \rangle \right) \end{aligned} \quad (\text{A2.4})$$

In the accompanying paper following this paper, we privilege time-variability variables to evaluate storms equations terms. In fact, terms resulting from the decomposition of time-variability express physical processes suitable for storms studies.

1.6.3 Appendix A3: Effective thermodynamics equation

When using the exact definition for a_T

$$a_T(T) = C_p T_r \left[\left(\frac{T - T_r}{T_r} \right) - \ln \left(\frac{T}{T_r} \right) \right] \quad (\text{A3.1})$$

the prognostic equation

$$\frac{da_T}{dt} - \frac{R\omega}{p} (T - T_r) - \left(1 - \frac{T_r}{T} \right) Q = 0 \quad (\text{A3.2})$$

is exact in the sense of resulting from the exact thermodynamic equation

$$C_p \frac{dT}{dt} - \frac{R}{p} \omega T - Q = 0 \quad (\text{A3.3})$$

Let us define $\chi = \frac{(T - T_r)}{T_r} = \left(\frac{T}{T_r} \right) - 1$ which is $<<1$ for practical applications. Then

$$\begin{aligned} a_T(T) &= C_p T_r \left[\left(\frac{T - T_r}{T_r} \right) - \ln \left(\frac{T}{T_r} \right) \right] \\ &= C_p T_r [\chi - \ln(1 + \chi)] \\ &= C_p T_r \left[\chi - \left(\chi - \frac{\chi^2}{2} + \frac{\chi^3}{3} - \dots \right) \right] \\ &= C_p T_r \left[\frac{\chi^2}{2} - \frac{\chi^3}{3} + \dots \right] \\ &= C_p T_r \left[\frac{\chi^2}{2} \left(1 - \frac{2\chi}{3} + \dots \right) \right] \\ &\approx C_p T_r \frac{\chi^2}{2} \\ &\approx \frac{C_p T_r}{2} \left(\frac{T - T_r}{T_r} \right)^2 \end{aligned} \quad (\text{A3.4})$$

which is the small- C approximation used in defining the temperature component of available enthalpy

$$a_T(T) \approx \frac{C_p T_r}{2} \left(\frac{T - T_r}{T_r} \right)^2 \quad (\text{A3.5})$$

Let us now return to the prognostic equation

$$\frac{da_T}{dt} - \frac{R\omega}{p} (T - T_r) - \left(1 - \frac{T_r}{T} \right) Q = 0 \quad (\text{A3.6})$$

and apply systematically the same small- C approximation. Consider the diabatic contribution

$$\left(1 - \frac{T_r}{T} \right) Q = \frac{T - T_r}{T_r} \frac{T_r}{T} = \frac{T - T_r}{T_r} (1 + \chi)^{-1} \approx \frac{T - T_r}{T_r} (1 - \chi) \approx \frac{T - T_r}{T_r} \quad (\text{A3.7})$$

So in the small- C approximation the corresponding approximate form of the prognostic equation is

$$\frac{da_T}{dt} - \frac{R\omega}{p} (T - T_r) - \left(\frac{T}{T_r} - 1 \right) Q \approx 0 \quad (\text{A3.8})$$

Note that this equation is slightly different from eq. (A3.2).

Using this equation corresponds to using an approximate form of the thermodynamic equation, as we shall show here:

$$\begin{aligned} & \frac{da_T}{dt} - \frac{R\omega}{p} (T - T_r) - \left(\frac{T}{T_r} - 1 \right) Q \approx 0 \\ & \Rightarrow \frac{C_p}{T_r} (T - T_r) \left[\frac{dT}{dt} - \frac{\omega R T_r}{p C_p} - \frac{Q}{C_p} \right] \approx 0 \\ & \Rightarrow \frac{dT}{dt} - \frac{\omega \alpha_r}{C_p} - \frac{Q}{C_p} \approx 0 \end{aligned} \quad (\text{A3.9})$$

which gives the effective, approximate form of the thermodynamic equation implied by the small- C approximation for a_T . We note that this approximate form of the thermodynamic equation is better than equation (65) in (Nikiéma et Laprise, 2013) that had also a factor of order unity $\frac{T_r}{T}$ affecting the diabatic heating term.

1.6.4 Appendix A4: Time-mean kinetic energy equation associated with time-mean wind

An equation for K_M is obtained by taking the dot product of the time-mean horizontal winds with the time-mean horizontal momentum equation as follows

$$\begin{aligned}\frac{\partial K_M}{\partial t} &= \langle \vec{V}_H \rangle \cdot \frac{\partial \langle \vec{V}_H \rangle}{\partial t} \\ &= - \langle \vec{V}_h \rangle \cdot \langle (\vec{V} \cdot \vec{\nabla}) \cdot \vec{V}_h \rangle - \langle \vec{V}_H \rangle \cdot \vec{\nabla} \langle \phi \rangle + \langle \vec{V}_h \rangle \cdot \langle \vec{F}_h \rangle\end{aligned}\quad (\text{A4.1})$$

When applying the following identity from Reynolds averaging rules

$$\langle AB \rangle = \langle A \rangle \langle B \rangle + \langle A' B' \rangle \quad (\text{A4.2})$$

we obtain

$$\begin{aligned}&\langle \vec{V}_h \rangle \cdot \langle (\vec{V} \cdot \vec{\nabla}) \cdot \vec{V}_h \rangle \\ &= \langle \vec{V}_h \rangle \cdot \left[\langle \vec{V} \rangle \cdot \vec{\nabla} \right] \cdot \langle \vec{V}_h \rangle + \langle (\vec{V}' \cdot \vec{\nabla}) \cdot \vec{V}_h' \rangle \\ &= \vec{\nabla} \cdot \left(\langle \vec{V} \rangle K_M \right) + \langle \vec{V}_h \rangle \cdot \langle \vec{V}' \cdot \vec{\nabla} \rangle \cdot \vec{V}_h' \\ &= \vec{\nabla} \cdot \left(\langle \vec{V} \rangle K_M \right) + \vec{\nabla} \cdot \left\langle \vec{V}' \left(\vec{V}_h' \cdot \langle \vec{V}_h \rangle \right) \right\rangle - \left\langle \vec{V}_h' \cdot \left(\vec{V}' \cdot \vec{\nabla} \right) \cdot \langle \vec{V}_h \rangle \right\rangle\end{aligned}\quad (\text{A4.3})$$

so that

$$\begin{aligned}\frac{\partial K_M}{\partial t} &= - \left\{ \vec{\nabla} \cdot \left(\langle \vec{V} \rangle K_M \right) + \vec{\nabla} \cdot \left\langle \vec{V}' \left(\vec{V}_h' \cdot \langle \vec{V}_h \rangle \right) \right\rangle - \left\langle \vec{V}_h' \cdot \left(\vec{V}' \cdot \vec{\nabla} \right) \cdot \langle \vec{V}_h \rangle \right\rangle \right\} \\ &\quad - \langle \vec{V}_h \rangle \cdot \vec{\nabla}_h \langle \phi \rangle + \langle \vec{V}_h \rangle \cdot \langle \vec{F}_h \rangle\end{aligned}\quad (\text{A4.4})$$

A_M and K_M energy reservoirs can be linked as follows:

$$\begin{aligned}
\langle \vec{V}_h \rangle \cdot (\vec{\nabla}_h \langle \phi \rangle) &= \vec{\nabla}_h \cdot (\langle \phi \rangle \langle \vec{V}_h \rangle) - \langle \phi \rangle (\vec{\nabla}_h \cdot \langle \vec{V}_h \rangle) \\
&= \vec{\nabla}_h \cdot (\langle \phi \rangle \langle \vec{V}_h \rangle) - \langle \phi \rangle \left(-\frac{\partial \langle \omega \rangle}{\partial p} \right) \\
&= \vec{\nabla}_h \cdot (\langle \phi \rangle \langle \vec{V}_h \rangle) + \langle \phi \rangle \left(\frac{\partial \langle \omega \rangle}{\partial p} \right) \\
&= \vec{\nabla}_h \cdot (\langle \phi \rangle \langle \vec{V}_h \rangle) + \left\{ \frac{\partial (\langle \phi \rangle \langle \omega \rangle)}{\partial p} - \langle \omega \rangle \frac{\partial \langle \phi \rangle}{\partial p} \right\} \\
&= \vec{\nabla} \cdot (\langle \phi \rangle \langle \vec{V} \rangle) + \langle \omega \rangle \langle \alpha \rangle
\end{aligned} \tag{A4.5}$$

1.6.5 Appendix A5: Time-mean kinetic energy associated with time-variability of the wind

The easiest way to obtain the time-mean kinetic energy associated with time-variability of the wind is by subtracting the time-mean kinetic energy equation and the kinetic energy equation associated with time-mean wind as follows

$$\begin{aligned} \frac{\partial K_E}{\partial t} &= \left\langle \vec{V}_h \cdot \frac{\partial \vec{V}_h}{\partial t} \right\rangle - \left\langle \vec{V}_h \right\rangle \cdot \frac{\partial \left\langle \vec{V}_h \right\rangle}{\partial t} \\ &= - \left\{ \left\langle (\vec{V} \cdot \vec{\nabla}) K \right\rangle - \left\langle \vec{V}_h \right\rangle \cdot \left\langle (\vec{V} \cdot \vec{\nabla}) \cdot \vec{V}_h \right\rangle \right\} - \left\{ \left\langle \vec{V}_h \cdot \vec{\nabla} \phi \right\rangle - \left\langle \vec{V}_h \right\rangle \cdot \vec{\nabla} \langle \phi \rangle \right\} + \left\{ \left\langle \vec{V}_h \cdot \vec{F}_h \right\rangle - \left\langle \vec{V}_h \right\rangle \cdot \left\langle \vec{F}_h \right\rangle \right\} \end{aligned} \quad (\text{A5.1})$$

Considering

$$\begin{aligned} &\left\langle (\vec{V} \cdot \vec{\nabla}) K \right\rangle \\ &= \vec{\nabla} \cdot \left\langle \vec{V} K \right\rangle \\ &= \vec{\nabla} \cdot \left(\left\langle \vec{V} \right\rangle \langle K \rangle \right) + \vec{\nabla} \cdot \left\langle \vec{V}' K_x \right\rangle \\ &= \vec{\nabla} \cdot \left\{ \left\langle \vec{V} \right\rangle (\langle K_M \rangle + \langle K_E \rangle) \right\} + \vec{\nabla} \cdot \left\langle \vec{V}' \left(\frac{1}{2} V_h'^2 - \left\langle \frac{1}{2} V_h'^2 \right\rangle + \left\langle \vec{V}_h \right\rangle \cdot \vec{V}_h' \right) \right\rangle \\ &= \vec{\nabla} \cdot \left(\left\langle \vec{V} \right\rangle K_M \right) + \vec{\nabla} \cdot \left(\left\langle \vec{V} \right\rangle K_E \right) + \vec{\nabla} \cdot \left\langle \vec{V}' \left(\frac{1}{2} V_h'^2 \right) \right\rangle + \vec{\nabla} \cdot \left\langle \vec{V}' \left(\vec{V}_h' \cdot \left\langle \vec{V}_h \right\rangle \right) \right\rangle \end{aligned} \quad (\text{A5.2})$$

and the identity obtained in eq. (A4.3), we obtain

$$\begin{aligned} &\left\langle (\vec{V} \cdot \vec{\nabla}) K \right\rangle - \left\langle \vec{V}_h \right\rangle \cdot \left\langle (\vec{V} \cdot \vec{\nabla}) \cdot \vec{V}_h \right\rangle \\ &= \left[\vec{\nabla} \cdot \left(\left\langle \vec{V} \right\rangle K_M \right) + \vec{\nabla} \cdot \left(\left\langle \vec{V} \right\rangle K_E \right) + \vec{\nabla} \cdot \left\langle \vec{V}' \left(\frac{1}{2} V_h'^2 \right) \right\rangle + \vec{\nabla} \cdot \left\langle \vec{V}' \left(\vec{V}_h' \cdot \left\langle \vec{V}_h \right\rangle \right) \right\rangle \right] \\ &\quad - \left[\vec{\nabla} \cdot \left(\left\langle \vec{V} \right\rangle K_M \right) + \vec{\nabla} \cdot \left\langle \vec{V}' \left(\vec{V}_h' \cdot \left\langle \vec{V}_h \right\rangle \right) \right\rangle - \left\langle \vec{V}_h' \cdot \left(\vec{V}' \cdot \vec{\nabla} \right) \cdot \left\langle \vec{V}_h \right\rangle \right\rangle \right] \\ &= \vec{\nabla} \cdot \left(\left\langle \vec{V} \right\rangle K_E \right) + \vec{\nabla} \cdot \left\langle \vec{V}' \left(\frac{1}{2} V_h'^2 \right) \right\rangle - \left\langle \vec{V}_h' \cdot \left(\vec{V}' \cdot \vec{\nabla} \right) \cdot \left\langle \vec{V}_h \right\rangle \right\rangle \end{aligned} \quad (\text{A5.3})$$

By doing the same for the frictional term

$$\left\langle \vec{V}_h \cdot \vec{F}_h \right\rangle - \left\langle \vec{V}_h \right\rangle \cdot \left\langle \vec{F}_h \right\rangle = \left\langle \vec{V}_h' \cdot \vec{F}_h' \right\rangle \quad (\text{A5.4})$$

so that

$$\begin{aligned} \frac{\partial K_M}{\partial t} = & - \left\{ \vec{\nabla} \cdot \left(\left\langle \vec{V} \right\rangle K_E \right) + \vec{\nabla} \cdot \left\langle \vec{V}' \left(\frac{1}{2} V_h'^2 \right) \right\rangle - \left\langle \vec{V}_h' \cdot \left(\vec{V}' \cdot \vec{\nabla} \right) \cdot \left\langle \vec{V}_h \right\rangle \right\rangle \right\} \\ & - \left\langle \vec{V}_H' \cdot \vec{\nabla} \phi' \right\rangle + \left\langle \vec{V}_h' \cdot \vec{F}_h' \right\rangle \end{aligned} \quad (\text{A5.5})$$

The link between A_E and K_E can be done by rewritten the term involving geopotential as follows:

$$\begin{aligned} & \left\langle \vec{V}_H \cdot \vec{\nabla} \phi \right\rangle - \left\langle \vec{V}_H \right\rangle \cdot \vec{\nabla} \langle \phi \rangle \\ = & \left\{ \vec{\nabla} \cdot \left\langle \phi \vec{V} \right\rangle + \langle \omega \alpha \rangle \right\} - \left\{ \vec{\nabla} \cdot \left(\langle \phi \rangle \langle \vec{V} \rangle \right) + \langle \omega \rangle \langle \alpha \rangle \right\} \\ = & \vec{\nabla} \cdot \left\{ \langle \phi \vec{V} \rangle - \left(\langle \phi \rangle \langle \vec{V} \rangle \right) \right\} + \left\{ \langle \omega \alpha \rangle - \langle \omega \rangle \langle \alpha \rangle \right\} \\ = & \vec{\nabla} \cdot \left\langle \phi' \vec{V}' \right\rangle + \langle \omega' \alpha' \rangle \end{aligned} \quad (\text{A5.6})$$

1.6.6 Appendix A6: Time-mean available enthalpy equation associated with time-mean temperature

An equation for A_M is obtained by multiplying $\frac{C_p}{T_r} \langle T - T_r \rangle$ by the time-mean thermodynamics equation as follows

$$\begin{aligned}\frac{\partial A_M}{\partial t} &= \frac{C_p}{T_r} \langle T - T_r \rangle \left\langle \frac{\partial T}{\partial t} \right\rangle \\ &= -\frac{C_p}{T_r} \langle T - T_r \rangle \left\langle (\vec{V} \cdot \vec{\nabla}) T \right\rangle + \langle \omega \rangle \frac{R}{p} \langle T - T_r \rangle + \left\langle \left(\frac{T}{T_r} - 1 \right) \right\rangle \langle Q \rangle\end{aligned}\quad (\text{A6.1})$$

Once again, using Reynolds averaging rule eq. (A4.2), we obtain

$$\begin{aligned}&\frac{C_p}{T_r} \langle T - T_r \rangle \left\langle (\vec{V} \cdot \vec{\nabla})(T - T_r) \right\rangle \\ &= \frac{C_p}{T_r} \langle T - T_r \rangle \left\{ \left(\langle \vec{V} \rangle \cdot \vec{\nabla} \right) \langle T - T_r \rangle + \left\langle (\vec{V}' \cdot \vec{\nabla}) T' \right\rangle \right\} \\ &= \vec{\nabla} \cdot \left(\langle \vec{V} \rangle A_M \right) + \frac{C_p}{T_r} \left\langle \langle T - T_r \rangle (\vec{V}' \cdot \vec{\nabla}) T' \right\rangle \\ &= \vec{\nabla} \cdot \left(\langle \vec{V} \rangle A_M \right) + \vec{\nabla} \cdot \left\langle \vec{V}' \left(\frac{C_p}{T_r} T' \langle T - T_r \rangle \right) \right\rangle - \frac{C_p}{T_r} \left(\langle T' \vec{V}' \rangle \cdot \vec{\nabla} \right) \langle T - T_r \rangle \\ &= \vec{\nabla} \cdot \left(\langle \vec{V} \rangle A_M \right) + \vec{\nabla} \cdot \left\langle \vec{V}' \left(\frac{C_p}{T_r} T' \langle T - T_r \rangle \right) \right\rangle - \frac{C_p}{T_r} \left(\langle T' \vec{V}' \rangle \cdot \vec{\nabla} \right) \langle T \rangle\end{aligned}\quad (\text{A6.2})$$

so that

$$\begin{aligned}\frac{\partial A_M}{\partial t} &= - \left\{ \vec{\nabla} \cdot \left(\langle \vec{V} \rangle A_M \right) + \vec{\nabla} \cdot \left\langle \vec{V}' \left(\frac{C_p}{T_r} T' \langle T - T_r \rangle \right) \right\rangle - \frac{C_p}{T_r} \left(\langle T' \vec{V}' \rangle \cdot \vec{\nabla} \right) \langle T \rangle \right\} \\ &\quad + \langle \omega \rangle \langle \alpha \rangle - \langle \omega \rangle \alpha_r + \left\langle \left(\frac{T}{T_r} - 1 \right) \right\rangle \langle Q \rangle\end{aligned}\quad (\text{A6.3})$$

1.6.7 Appendix A7: Time-mean available enthalpy equation associated with time-variability of temperature

An equation for A_E is obtained by subtracting the time-mean enthalpy equation by the time-mean available enthalpy equation associated with time-mean temperature as follows

$$\begin{aligned}\frac{\partial A_E}{\partial t} &= \frac{C_p}{T_r} \left\langle \left(T - T_r \right) \frac{\partial T}{\partial t} \right\rangle - \frac{C_p}{T_r} \langle T - T_r \rangle \left\langle \frac{\partial T}{\partial t} \right\rangle \\ &= - \left[\left\langle \left(\vec{V} \cdot \vec{\nabla} \right) A \right\rangle - \left\langle \frac{C_p}{T_r} \langle T - T_r \rangle \left(\vec{V} \cdot \vec{\nabla} \right) T \right\rangle \right] + \left[\langle \omega \alpha \rangle - \langle \omega \rangle \langle \alpha \rangle \right] + \left[\left\langle \left(\frac{T}{T_r} - 1 \right) Q \right\rangle - \left\langle \left(\frac{T}{T_r} - 1 \right) \right\rangle \langle Q \rangle \right]\end{aligned}\quad (\text{A7.1})$$

Considering

$$\begin{aligned}&\left\langle \left(\vec{V} \cdot \vec{\nabla} \right) A \right\rangle \\ &= \vec{\nabla} \cdot \left\langle \vec{V} A \right\rangle \\ &= \vec{\nabla} \cdot \left(\left\langle \vec{V} \right\rangle \langle A \rangle \right) + \vec{\nabla} \cdot \left\langle \vec{V}^t A_x \right\rangle \\ &= \vec{\nabla} \cdot \left\{ \left\langle \vec{V} \right\rangle \left(\langle A_M \rangle + \langle A_E \rangle \right) \right\} + \vec{\nabla} \cdot \left\langle \vec{V}^t \left(\frac{C_p}{2T_r} T'^2 - \left\langle \frac{C_p}{2T_r} T'^2 \right\rangle + \frac{C_p}{T_r} T' \langle T - T_r \rangle \right) \right\rangle \\ &= \vec{\nabla} \cdot \left(\left\langle \vec{V} \right\rangle A_M \right) + \vec{\nabla} \cdot \left(\left\langle \vec{V} \right\rangle A_E \right) + \vec{\nabla} \cdot \left\langle \vec{V}^t \left(\frac{C_p}{2T_r} T'^2 \right) \right\rangle + \vec{\nabla} \cdot \left\langle \vec{V}^t \left(\frac{C_p}{T_r} T' \langle T - T_r \rangle \right) \right\rangle\end{aligned}\quad (\text{A7.2})$$

and eqn. (A6.2), we obtain

$$\begin{aligned}
& \left\langle (\vec{V} \cdot \vec{\nabla}) A \right\rangle - \frac{C_p}{T_r} \langle T - T_r \rangle \left\langle (\vec{V} \cdot \vec{\nabla}) T \right\rangle \\
&= \left[\left[\vec{\nabla} \cdot \left(\langle \vec{V} \rangle_{A_M} \right) + \vec{\nabla} \cdot \left(\langle \vec{V} \rangle_{A_E} \right) + \vec{\nabla} \cdot \left\langle \vec{V}' \left(\frac{C_p}{2T_r} T'^2 \right) \right\rangle + \vec{\nabla} \cdot \left\langle \vec{V}' \left(\frac{C_p}{T_r} T' \langle T - T_r \rangle \right) \right\rangle \right] \right] \\
&\quad - \left[\vec{\nabla} \cdot \left(\langle \vec{V} \rangle_{A_M} \right) + \vec{\nabla} \cdot \left\langle \vec{V}' \left(\frac{C_p}{T_r} T' \langle T - T_r \rangle \right) \right\rangle - \frac{C_p}{T_r} \left(\langle T' \vec{V}' \rangle \cdot \vec{\nabla} \right) \langle T \rangle \right] \\
&= \vec{\nabla} \cdot \left(\langle \vec{V} \rangle_{A_E} \right) + \vec{\nabla} \cdot \left\langle \vec{V}' \left(\frac{C_p}{2T_r} T'^2 \right) \right\rangle + \frac{C_p}{T_r} \left(\langle T' \vec{V}' \rangle \cdot \vec{\nabla} \right) \langle T \rangle
\end{aligned} \tag{A7.3}$$

According to Reynolds decomposition rules

$$\langle w\alpha \rangle - \langle w \rangle \langle \alpha \rangle = \langle w' \alpha' \rangle \tag{A7.4}$$

$$\left\langle \left(\frac{T}{T_r} - 1 \right) Q \right\rangle - \left\langle \left(\frac{T}{T_r} - 1 \right) \right\rangle \langle Q \rangle = \frac{\langle T' Q' \rangle}{T_r} \tag{A7.5}$$

so that

$$\frac{\partial A_E}{\partial t} = - \left\{ \vec{\nabla} \cdot \left(\langle \vec{V} \rangle_{A_E} \right) + \vec{\nabla} \cdot \left\langle \vec{V}' \left(\frac{C_p}{2T_r} T'^2 \right) \right\rangle + \frac{C_p}{T_r} \left(\langle T' \vec{V}' \rangle \cdot \vec{\nabla} \right) \langle T \rangle \right\} + \langle w' \alpha' \rangle + \frac{\langle T' Q' \rangle}{T_r} \tag{A7.6}$$

1.6.8 Appendix A8: Instantaneous kinetic energy equation associated with variance of wind fluctuations

An equation for K_{X1} is obtained by taking the dot product of the time-variability horizontal wind \overrightarrow{V}_h' with the time-variability momentum equation

$$\begin{aligned}\frac{\partial K_{X1}}{\partial t} &= \overrightarrow{V}_h' \cdot \frac{\partial \overrightarrow{V}_h'}{\partial t} - \left\langle \overrightarrow{V}_h' \cdot \frac{\partial \overrightarrow{V}_h'}{\partial t} \right\rangle \\ &= \overrightarrow{V}_h' \cdot \left(-\left\langle (\vec{V} \cdot \vec{\nabla}) \cdot \vec{V}_h - \left\langle (\vec{V} \cdot \vec{\nabla}) \cdot \vec{V}_h \right\rangle \right\rangle - f \vec{k} \times \overrightarrow{V}_h' \cdot \vec{\nabla} \phi' + \overrightarrow{F}_h' \right) \\ &\quad - \left\langle \overrightarrow{V}_h' \cdot \left(-\left\langle (\vec{V} \cdot \vec{\nabla}) \cdot \vec{V}_h - \left\langle (\vec{V} \cdot \vec{\nabla}) \cdot \vec{V}_h \right\rangle \right\rangle - f \vec{k} \times \overrightarrow{V}_h' \cdot \vec{\nabla} \phi' + \overrightarrow{F}_h' \right) \right\rangle\end{aligned}\tag{A8.1}$$

The first advection term may be rewritten using the following Reynolds identity

$$AB - \langle AB \rangle = \langle A \rangle B' + A' \langle B \rangle + A' B' - \langle A' B' \rangle\tag{A8.2}$$

$$\begin{aligned}&-\overrightarrow{V}_h' \cdot \left\{ \left\langle (\vec{V} \cdot \vec{\nabla}) \cdot \vec{V}_h - \left\langle (\vec{V} \cdot \vec{\nabla}) \cdot \vec{V}_h \right\rangle \right\rangle \right\} \\ &= -\overrightarrow{V}_h' \cdot \left\{ \left\langle (\vec{V}' \cdot \vec{\nabla}) \cdot \langle \vec{V}_h \rangle + \left\langle (\vec{V} \cdot \vec{\nabla}) \cdot \vec{V}_h \right\rangle + (\vec{V}' \cdot \vec{\nabla}) \cdot \overrightarrow{V}_h' - \left\langle (\vec{V}' \cdot \vec{\nabla}) \cdot \overrightarrow{V}_h' \right\rangle \right\rangle \right\} \\ &= -\overrightarrow{V}_h' \cdot (\vec{V}' \cdot \vec{\nabla}) \cdot \langle \vec{V}_h \rangle - \vec{\nabla} \cdot \left\{ \langle \vec{V} \rangle \left(\frac{1}{2} V_h'^2 \right) \right\} - \vec{\nabla} \cdot \left\{ \overrightarrow{V}' \left(\frac{1}{2} V_h'^2 \right) \right\} + \overrightarrow{V}_h' \cdot \left\langle (\vec{V}' \cdot \vec{\nabla}) \cdot \overrightarrow{V}_h' \right\rangle \\ &= -\vec{\nabla} \cdot \left\{ \vec{V} \left(\frac{1}{2} V_h'^2 \right) \right\} - \overrightarrow{V}_h' \cdot (\vec{V}' \cdot \vec{\nabla}) \cdot \langle \vec{V}_h \rangle + \overrightarrow{V}_h' \cdot \left\langle (\vec{V}' \cdot \vec{\nabla}) \cdot \overrightarrow{V}_h' \right\rangle\end{aligned}\tag{A8.3}$$

Consequently, the second advection term is its time-average

$$\begin{aligned}&\left\langle \overrightarrow{V}_h' \cdot \left\{ \left\langle (\vec{V} \cdot \vec{\nabla}) \cdot \vec{V}_h - \left\langle (\vec{V} \cdot \vec{\nabla}) \cdot \vec{V}_h \right\rangle \right\rangle \right\} \right\rangle \\ &= \vec{\nabla} \cdot \left\{ \left\langle \vec{V} \left(\frac{1}{2} V_h'^2 \right) \right\rangle \right\} + \left\langle \overrightarrow{V}_h' \cdot (\vec{V}' \cdot \vec{\nabla}) \cdot \langle \vec{V}_h \rangle \right\rangle\end{aligned}\tag{A8.4}$$

The term involving geopotential may be rewritten as follows

Terms involving the Coriolis parameter are all equals to zero.

Finally,

$$\begin{aligned} \frac{\partial K_{X1}}{\partial t} = & -\vec{\nabla} \cdot \left\{ \vec{V} \left(\frac{1}{2} V_h'^2 \right) - \left\langle \vec{V} \left(\frac{1}{2} V_h'^2 \right) \right\rangle \right\} - \left\{ \vec{V}_h' \cdot (\vec{V}' \cdot \vec{\nabla}) \cdot \langle \vec{V}_h' \rangle - \langle \vec{V}_h' \cdot (\vec{V}' \cdot \vec{\nabla}) \cdot \langle \vec{V}_h' \rangle \rangle \right\} \\ & + \vec{V}_h' \cdot \left\langle (\vec{V}' \cdot \vec{\nabla}) \cdot \vec{V}_h' \right\rangle - \left\{ \vec{V}_h' \cdot \vec{\nabla}_h \phi' - \langle \vec{V}_h' \cdot \vec{\nabla}_h \phi' \rangle \right\} + \left\{ \vec{V}_h' \cdot \vec{F}_h' - \langle \vec{V}_h' \cdot \vec{F}_h' \rangle \right\} \end{aligned} \quad (\text{A8.5})$$

A_{X1} and K_{X1} energy reservoirs can be linked as follows:

$$\begin{aligned} & \vec{V}_h' \cdot \vec{\nabla}_h \phi' \\ &= \vec{V}_h' \cdot \vec{\nabla}_h \phi' + \omega' \frac{\partial \phi'}{\partial p} - \omega' \frac{\partial \phi'}{\partial p} \\ &= \vec{V}' \cdot \vec{\nabla} \phi' - \omega' \frac{\partial \phi'}{\partial p} \quad (\text{A8.6}) \\ &= \left\{ \vec{\nabla} \cdot (\phi' \vec{V}') - \phi' (\vec{\nabla} \cdot \vec{V}') \right\} + \omega' \alpha' \\ &= \vec{\nabla} \cdot (\phi' \vec{V}') + \omega' \alpha' \end{aligned}$$

1.6.9 Appendix A9: Instantaneous kinetic energy equation associated with covariance of wind fluctuations and wind time-average

An equation for K_{X2} is obtained by taking the dot product of time-variability horizontal wind \overrightarrow{V}_h' with the time-mean momentum equation and the dot product of time-mean horizontal wind $\langle \overrightarrow{V}_h' \rangle$ with the time-variability momentum equation as follows

$$\begin{aligned} \frac{\partial K_{X2}}{\partial t} &= \overrightarrow{V}_h' \cdot \frac{\partial \langle \overrightarrow{V}_h' \rangle}{\partial t} + \langle \overrightarrow{V}_h' \rangle \cdot \frac{\partial \overrightarrow{V}_h'}{\partial t} \\ &= \overrightarrow{V}_h' \cdot \left[-\langle (\vec{V} \cdot \vec{\nabla}) \cdot \vec{V}_H \rangle - f \vec{k} \times \langle \vec{V}_H \rangle \cdot \vec{\nabla} \langle \phi \rangle + \langle \vec{F}_H \rangle \right] \\ &\quad + \langle \overrightarrow{V}_h' \rangle \cdot \left[-\left\{ \langle (\vec{V} \cdot \vec{\nabla}) \cdot \vec{V}_H \rangle - \langle (\vec{V} \cdot \vec{\nabla}) \cdot \vec{V}_H \rangle \right\} - f \vec{k} \times \vec{V}_H \cdot \vec{\nabla} \phi + \vec{F}_H \right] \end{aligned} \quad (\text{A9.1})$$

The total wind advection term is:

$$\begin{aligned} &- \overrightarrow{V}_h' \cdot \langle (\vec{V} \cdot \vec{\nabla}) \cdot \vec{V}_h \rangle - \left[\langle \overrightarrow{V}_h' \rangle \cdot \langle (\vec{V} \cdot \vec{\nabla}) \cdot \vec{V}_h \rangle - \langle \overrightarrow{V}_h' \rangle \cdot \langle (\vec{V} \cdot \vec{\nabla}) \cdot \vec{V}_h \rangle \right] \\ &= - \overrightarrow{V}_h' \cdot \langle (\vec{V} \cdot \vec{\nabla}) \cdot \vec{V}_h \rangle - \left[\langle \vec{V}_h - \vec{V}_h' \rangle \cdot \langle \vec{V} \cdot \vec{\nabla} \rangle \cdot \vec{V}_h - \langle \overrightarrow{V}_h' \rangle \cdot \langle (\vec{V} \cdot \vec{\nabla}) \cdot \vec{V}_h \rangle \right] \\ &= \overrightarrow{V}_h' \cdot \left[\langle \vec{V} \cdot \vec{\nabla} \rangle \cdot \vec{V}_h - \langle (\vec{V} \cdot \vec{\nabla}) \cdot \vec{V}_h \rangle \right] - \overrightarrow{V}_h \cdot \langle \vec{V} \cdot \vec{\nabla} \rangle \cdot \vec{V}_h + \langle \overrightarrow{V}_h' \rangle \cdot \langle (\vec{V} \cdot \vec{\nabla}) \cdot \vec{V}_h \rangle \end{aligned} \quad (\text{A9.2})$$

The first term into bracket has already been decomposed in (A8.3), the second is the advection of the total kinetic energy by the three-dimensional wind vector and the last term is obtained by combining two Reynolds identities:

$$\begin{aligned} \langle A \rangle \langle BC \rangle &= \langle A(BC) \rangle - \langle A'(BC)' \rangle \\ &= \langle ABC \rangle - \langle A' \left(B' \langle C \rangle + \langle B \rangle C' + B'C' - \langle B'C' \rangle \right) \rangle \\ &= \langle ABC \rangle - \langle A'B' \langle C \rangle \rangle - \langle A' \langle B \rangle C' \rangle - \langle A'B'C' \rangle \end{aligned} \quad (\text{A9.3})$$

we obtain

$$\begin{aligned}
& \overrightarrow{V}_h' \cdot \left[(\overrightarrow{V} \cdot \overrightarrow{\nabla}) \cdot \overrightarrow{V}_h - \langle (\overrightarrow{V} \cdot \overrightarrow{\nabla}) \cdot \overrightarrow{V}_h \rangle \right] - \overrightarrow{V}_h \cdot (\overrightarrow{V} \cdot \overrightarrow{\nabla}) \cdot \overrightarrow{V}_h + \langle \overrightarrow{V}_h \rangle \cdot \langle (\overrightarrow{V} \cdot \overrightarrow{\nabla}) \cdot \overrightarrow{V}_h \rangle \\
&= \left\{ \overrightarrow{\nabla} \cdot \left[\overrightarrow{V} \left(\frac{1}{2} V_h'^2 \right) \right] + \overrightarrow{V}_h' \cdot (\overrightarrow{V}' \cdot \overrightarrow{\nabla}) \cdot \langle \overrightarrow{V}_h \rangle - \overrightarrow{V}_h' \cdot \langle (\overrightarrow{V}' \cdot \overrightarrow{\nabla}) \cdot \overrightarrow{V}_h' \rangle \right\} - \overrightarrow{\nabla} \cdot \langle \overrightarrow{V} K \rangle \\
&+ \left\{ \langle \overrightarrow{V}_h \cdot (\overrightarrow{V} \cdot \overrightarrow{\nabla}) \cdot \overrightarrow{V}_h \rangle - \langle \overrightarrow{V}_h' \cdot (\overrightarrow{V}' \cdot \overrightarrow{\nabla}) \cdot \langle \overrightarrow{V}_h \rangle \rangle - \langle \overrightarrow{V}_h' \cdot \langle (\overrightarrow{V}' \cdot \overrightarrow{\nabla}) \cdot \overrightarrow{V}_h' \rangle - \langle \overrightarrow{V}_h' \cdot (\overrightarrow{V}' \cdot \overrightarrow{\nabla}) \cdot \overrightarrow{V}_h' \rangle \right\} \\
&= \left\{ \overrightarrow{\nabla} \cdot \left[\overrightarrow{V} \left(\frac{1}{2} V_h'^2 \right) \right] + \overrightarrow{V}_h' \cdot (\overrightarrow{V}' \cdot \overrightarrow{\nabla}) \cdot \langle \overrightarrow{V}_h \rangle - \overrightarrow{V}_h' \cdot \langle (\overrightarrow{V}' \cdot \overrightarrow{\nabla}) \cdot \overrightarrow{V}_h' \rangle \right\} - \overrightarrow{\nabla} \cdot \langle \overrightarrow{V} K \rangle \quad (A9.4) \\
&+ \left\{ \overrightarrow{\nabla} \cdot \langle \overrightarrow{V} K \rangle - \langle \overrightarrow{V}_h' \cdot (\overrightarrow{V}' \cdot \overrightarrow{\nabla}) \cdot \langle \overrightarrow{V}_h \rangle \rangle - \overrightarrow{\nabla} \cdot \left\langle \overrightarrow{V} \left(\frac{1}{2} V_h'^2 \right) \right\rangle \right\} \\
&= -\overrightarrow{\nabla} \cdot \left\{ \overrightarrow{V} \left(K - \frac{1}{2} V_h'^2 \right) - \left\langle \overrightarrow{V} \left(K - \frac{1}{2} V_h'^2 \right) \right\rangle \right\} \\
&+ \left\{ \overrightarrow{V}_h' \cdot (\overrightarrow{V}' \cdot \overrightarrow{\nabla}) \cdot \langle \overrightarrow{V}_h \rangle - \langle \overrightarrow{V}_h' \cdot (\overrightarrow{V}' \cdot \overrightarrow{\nabla}) \cdot \langle \overrightarrow{V}_h \rangle \rangle - \overrightarrow{V}_h' \cdot \langle (\overrightarrow{V}' \cdot \overrightarrow{\nabla}) \cdot \overrightarrow{V}_h' \rangle \right\}
\end{aligned}$$

Terms involving geopotential may be rewritten as follows

$$\begin{aligned}
\frac{\partial K_{X2}}{\partial t} &= -\overrightarrow{\nabla} \cdot \left\{ \overrightarrow{V} \left(K - \frac{1}{2} V_h'^2 \right) - \left\langle \overrightarrow{V} \left(K - \frac{1}{2} V_h'^2 \right) \right\rangle \right\} + \left\{ \overrightarrow{V}_h' \cdot (\overrightarrow{V}' \cdot \overrightarrow{\nabla}) \cdot \langle \overrightarrow{V}_h \rangle - \langle \overrightarrow{V}_h' \cdot (\overrightarrow{V}' \cdot \overrightarrow{\nabla}) \cdot \langle \overrightarrow{V}_h \rangle \rangle \right\} \\
&- \overrightarrow{V}_h' \cdot \langle (\overrightarrow{V}' \cdot \overrightarrow{\nabla}) \cdot \overrightarrow{V}_h' \rangle - \overrightarrow{\nabla} \cdot \left\{ \overrightarrow{V}_h' \cdot \overrightarrow{\nabla} \langle \overrightarrow{\phi} \rangle + \langle \overrightarrow{V}_h \rangle \cdot \overrightarrow{\nabla} \overrightarrow{\phi} \right\} + \left\{ \overrightarrow{V}_h' \cdot \langle \overrightarrow{F}_h \rangle + \langle \overrightarrow{V}_h \rangle \cdot \overrightarrow{F}_H \right\} \quad (A9.5)
\end{aligned}$$

A_{X2} and K_{X2} energy reservoirs can be linked as follows:

$$\begin{aligned}
\overrightarrow{V}_h' \cdot \overrightarrow{\nabla} \langle \phi \rangle &= \overrightarrow{\nabla}_h' \cdot (\overrightarrow{V}_h' \langle \phi \rangle) - \langle \phi \rangle (\overrightarrow{\nabla}_h' \cdot \overrightarrow{V}_h') \\
&= \overrightarrow{\nabla}_h' \cdot (\overrightarrow{V}_h' \langle \phi \rangle) + \langle \phi \rangle \frac{\partial \omega'}{\partial p} \\
&= \left\{ \overrightarrow{\nabla}_h' \cdot (\overrightarrow{V}_h' \langle \phi \rangle) + \frac{\partial \omega' \langle \phi \rangle}{\partial p} \right\} - \omega' \frac{\partial \langle \phi \rangle}{\partial p} \quad (A9.6) \\
&= \overrightarrow{\nabla} \cdot (\overrightarrow{V}' \langle \phi \rangle) + \omega' \langle \alpha \rangle
\end{aligned}$$

Likewise,

$$\langle \overrightarrow{V}_h \rangle \cdot \overrightarrow{\nabla} \phi' = \overrightarrow{\nabla} \cdot (\langle \overrightarrow{V} \rangle \phi') + \langle \omega \rangle \alpha' \quad (A9.7)$$

1.6.10 Appendix A10: Instantaneous available enthalpy associated with variance of temperature fluctuations

An equation for A_{X1} is obtained by multiplying $\frac{C_p}{T_r} T'$ with the time-variability thermodynamics equation

$$\begin{aligned}\frac{\partial A_{X1}}{\partial t} &= \frac{C_p}{T_r} \left(T' \frac{\partial T'}{\partial t} - \left\langle T' \frac{\partial T'}{\partial t} \right\rangle \right) \\ &= \frac{C_p}{T_r} T' \left(- \left\{ (\vec{V} \cdot \vec{\nabla}) T - \left\langle (\vec{V} \cdot \vec{\nabla}) T \right\rangle \right\} + \frac{\omega' \alpha_r}{C_p} + \frac{Q'}{C_p} \right) \\ &\quad - \frac{C_p}{T_r} \left\langle T' \left(- \left\{ (\vec{V} \cdot \vec{\nabla}) T - \left\langle (\vec{V} \cdot \vec{\nabla}) T \right\rangle \right\} + \frac{\omega' \alpha_r}{C_p} + \frac{Q'}{C_p} \right) \right\rangle\end{aligned}\tag{A10.1}$$

The first advection term may be rewritten as follows

$$\begin{aligned}&- \frac{C_p}{T_r} T' \left\{ (\vec{V} \cdot \vec{\nabla}) T - \left\langle (\vec{V} \cdot \vec{\nabla}) T \right\rangle \right\} \\ &= - \frac{C_p}{T_r} T' \left\{ \left\langle \vec{V} \right\rangle \cdot \vec{\nabla} T' + (\vec{V}' \cdot \vec{\nabla}) \langle T \rangle + (\vec{V}' \cdot \vec{\nabla}) T' - \left\langle (\vec{V}' \cdot \vec{\nabla}) T' \right\rangle \right\} \\ &= - \vec{\nabla} \cdot \left\{ \left\langle \vec{V} \right\rangle \left(\frac{C_p}{2T_r} T'^2 \right) \right\} - \frac{C_p}{T_r} T' (\vec{V}' \cdot \vec{\nabla}) \langle T \rangle - \vec{\nabla} \cdot \left\{ \vec{V}' \left(\frac{C_p}{2T_r} T'^2 \right) \right\} + \frac{C_p}{T_r} T' \left\langle (\vec{V}' \cdot \vec{\nabla}) T' \right\rangle \\ &= - \vec{\nabla} \cdot \left\{ \vec{V} \left(\frac{C_p}{2T_r} T'^2 \right) \right\} - \frac{C_p}{T_r} T' (\vec{V}' \cdot \vec{\nabla}) \langle T \rangle + \frac{C_p}{T_r} T' \left\langle (\vec{V}' \cdot \vec{\nabla}) T' \right\rangle\end{aligned}\tag{A10.2}$$

Consequently, the second advection term is its time-average

$$\begin{aligned}&\frac{C_p}{T_r} T' \left\{ (\vec{V} \cdot \vec{\nabla}) T - \left\langle (\vec{V} \cdot \vec{\nabla}) T \right\rangle \right\} \\ &= \vec{\nabla} \cdot \left\{ \left\langle \vec{V} \left(\frac{C_p}{2T_r} T'^2 \right) \right\rangle \right\} + \frac{C_p}{T_r} \left\langle T' (\vec{V}' \cdot \vec{\nabla}) \langle T \rangle \right\rangle\end{aligned}\tag{A10.3}$$

so that

$$\begin{aligned}
\frac{\partial A_{x1}}{\partial t} = & -\vec{\nabla} \cdot \left\{ \vec{V} \left(\frac{C_p}{2T_r} T'^2 \right) - \left\langle \vec{V} \left(\frac{C_p}{2T_r} T'^2 \right) \right\rangle \right\} - \frac{C_p}{T_r} \left\{ \left\langle T' \vec{V}' \cdot \vec{\nabla} \right\rangle \langle T \rangle - \left\langle \left(T' \vec{V}' \cdot \vec{\nabla} \right) \langle T \rangle \right\rangle \right\} \\
& + \frac{C_p}{T_r} T' \left\langle \left(\vec{V}' \cdot \vec{\nabla} \right) T' \right\rangle + \left\{ \omega' \alpha' - \left\langle \omega' \alpha' \right\rangle \right\} + \frac{1}{T_r} \left\{ T' Q' - \left\langle T' Q' \right\rangle \right\}
\end{aligned} \tag{A10.4}$$

1.6.11 Appendix A11: Instantaneous available enthalpy associated with covariance of temperature fluctuations and wind time-average

An equation for A_{X2} is obtained by multiplying $\frac{C_p}{T_r} T'$ with the time-mean thermodynamics equation and $\frac{C_p}{T_r} \langle T - T_r \rangle$ with the time-variability thermodynamics equation as follows

$$\begin{aligned} \frac{\partial A_{X2}}{\partial t} &= \frac{C_p}{T_r} \left(T' \frac{\partial \langle T \rangle}{\partial t} + \langle T - T_r \rangle \frac{\partial T'}{\partial t} \right) \\ &= \frac{C_p}{T_r} T' \left(-\langle (\vec{V} \cdot \vec{\nabla}) (T - T_r) \rangle + \frac{\langle \omega \rangle \alpha_r}{C_p} + \frac{\langle Q \rangle}{C_p} \right) \\ &\quad + \frac{C_p}{T_r} \langle T - T_r \rangle \left(-\left\{ \langle (\vec{V} \cdot \vec{\nabla}) (T - T_r) \rangle - \langle (\vec{V} \cdot \vec{\nabla}) (T - T_r) \rangle \right\} + \frac{\omega' \alpha_r}{C_p} + \frac{Q'}{C_p} \right) \end{aligned} \quad (\text{A11.1})$$

Considering

$$\begin{aligned} &-T' \langle (\vec{V} \cdot \vec{\nabla}) (T - T_r) \rangle - \left[\langle T - T_r \rangle \langle (\vec{V} \cdot \vec{\nabla}) (T - T_r) \rangle - \langle T - T_r \rangle \langle (\vec{V} \cdot \vec{\nabla}) (T - T_r) \rangle \right] \\ &= -T' \langle (\vec{V} \cdot \vec{\nabla}) T \rangle - \left[\langle T - T_r \rangle \langle (\vec{V} \cdot \vec{\nabla}) T \rangle - \langle T - T_r \rangle \langle (\vec{V} \cdot \vec{\nabla}) T \rangle \right] \\ &= -T' \langle (\vec{V} \cdot \vec{\nabla}) T \rangle - \left[(T - T' - T_r) \langle (\vec{V} \cdot \vec{\nabla}) T \rangle - \langle T - T_r \rangle \langle (\vec{V} \cdot \vec{\nabla}) T \rangle \right] \\ &= -T' \langle (\vec{V} \cdot \vec{\nabla}) T \rangle - \left[\{(T - T_r) - T'\} \langle (\vec{V} \cdot \vec{\nabla}) T \rangle - \langle T - T_r \rangle \langle (\vec{V} \cdot \vec{\nabla}) T \rangle \right] \\ &= T' \left[\langle (\vec{V} \cdot \vec{\nabla}) T \rangle - \langle (\vec{V} \cdot \vec{\nabla}) T \rangle \right] - (T - T_r) \langle (\vec{V} \cdot \vec{\nabla}) T \rangle + \langle T - T_r \rangle \langle (\vec{V} \cdot \vec{\nabla}) T \rangle \end{aligned} \quad (\text{A11.2})$$

The first term into bracket has already been evaluated in eq. (A10.2), the second is proportional to the advection of the total available enthalpy by the three-dimensional wind vector and the last term is obtained using the combination of two Reynolds identity developed in eq. (A9.3) as follows:

$$\begin{aligned}
& \langle T - T_r \rangle \langle (\vec{V} \cdot \vec{\nabla}) T \rangle \\
&= \left\langle (T - T_r) (\vec{V} \cdot \vec{\nabla}) T \right\rangle + \left\langle T' (\vec{V} \cdot \vec{\nabla}) \langle T \rangle \right\rangle + \left\langle T' \left(\langle \vec{V} \rangle \cdot \vec{\nabla} \right) T' \right\rangle - \left\langle T' (\vec{V}' \cdot \vec{\nabla}) T' \right\rangle \\
&= \vec{\nabla} \cdot \left\langle \vec{V} \frac{(T - T_r)^2}{2} \right\rangle + \left\langle T' (\vec{V} \cdot \vec{\nabla}) \langle T \rangle \right\rangle + \vec{\nabla} \cdot \left\langle \left(\langle \vec{V} \rangle \frac{T'^2}{2} \right) \right\rangle - \vec{\nabla} \cdot \left\langle \left(\vec{V}' \frac{T'^2}{2} \right) \right\rangle
\end{aligned} \tag{A11.3}$$

Consequently, the total advection term becomes

$$\begin{aligned}
& \frac{C_p}{T_r} T' \left[(\vec{V} \cdot \vec{\nabla}) T - \langle (\vec{V} \cdot \vec{\nabla}) T \rangle \right] - \frac{C_p}{T_r} (T - T_r) (\vec{V} \cdot \vec{\nabla}) T + \frac{C_p}{T_r} \langle T - T_r \rangle \langle (\vec{V} \cdot \vec{\nabla}) T \rangle \\
&= \left\{ \vec{\nabla} \cdot \left\langle \vec{V} \left(\frac{C_p}{2T_r} T'^2 \right) \right\rangle + \frac{C_p}{T_r} T' (\vec{V}' \cdot \vec{\nabla}) \langle T \rangle - \frac{C_p}{T_r} T' \langle (\vec{V}' \cdot \vec{\nabla}) T' \rangle \right\} - \vec{\nabla} \cdot \left\langle \vec{V} A \right\rangle \\
&+ \left\{ \vec{\nabla} \cdot \left\langle \vec{V} A \right\rangle - \left\langle \frac{C_p}{T_r} T' (\vec{V}' \cdot \vec{\nabla}) \langle T \rangle \right\rangle - \left\langle \frac{C_p}{T_r} T' \left(\langle \vec{V} \rangle \cdot \vec{\nabla} \right) T' \right\rangle - \left\langle \frac{C_p}{T_r} T' (\vec{V}' \cdot \vec{\nabla}) T' \right\rangle \right\} \\
&= \left\{ \vec{\nabla} \cdot \left\langle \vec{V} \left(\frac{C_p}{2T_r} T'^2 \right) \right\rangle + \frac{C_p}{T_r} T' (\vec{V}' \cdot \vec{\nabla}) \langle T \rangle - \frac{C_p}{T_r} T' \langle (\vec{V}' \cdot \vec{\nabla}) T' \rangle \right\} - \vec{\nabla} \cdot \left\langle \vec{V} A \right\rangle \\
&+ \left\{ \vec{\nabla} \cdot \left\langle \vec{V} A \right\rangle - \left\langle \frac{C_p}{T_r} T' (\vec{V}' \cdot \vec{\nabla}) \langle T \rangle \right\rangle - \vec{\nabla} \cdot \left\langle \vec{V} \left(\frac{C_p}{2T_r} T'^2 \right) \right\rangle \right\} \\
&= -\vec{\nabla} \cdot \left\{ \vec{V} \left(A - \frac{C_p}{2T_r} T'^2 \right) - \left\langle \vec{V} \left(A - \frac{C_p}{2T_r} T'^2 \right) \right\rangle \right\} + \frac{C_p}{T_r} \left\{ \left(T' \vec{V}' \cdot \vec{\nabla} \right) \langle T \rangle - \left\langle \left(T' \vec{V}' \cdot \vec{\nabla} \right) \langle T \rangle \right\rangle \right\} \\
&- \frac{C_p}{T_r} T' \langle (\vec{V}' \cdot \vec{\nabla}) T' \rangle
\end{aligned} \tag{A11.4}$$

Moreover

$$\frac{C_p}{T_r} T' \frac{\langle \omega \rangle \alpha_r}{C_p} = \langle \omega \rangle \alpha' \tag{A11.5}$$

$$\langle T - T_r \rangle \frac{\omega' R}{p} = \omega' (\langle \alpha \rangle - \alpha_r) \tag{A11.6}$$

$$\frac{\partial A_{x2}}{\partial t} = -\vec{\nabla} \cdot \left\{ \vec{V} \left(A - \frac{C_p}{2T_r} T'^2 \right) - \left\langle \vec{V} \left(A - \frac{C_p}{2T_r} T'^2 \right) \right\rangle \right\} + \frac{C_p}{T_r} \left\{ \left(T' \vec{V}' \cdot \vec{\nabla} \right) \langle T \rangle - \left\langle \left(T' \vec{V}' \cdot \vec{\nabla} \right) \langle T \rangle \right\rangle \right\}$$

so that $- \frac{C_p}{T_r} T' \left\langle \left(\vec{V}' \cdot \vec{\nabla} \right) T' \right\rangle + \left[\left(\langle \omega \rangle \alpha' + \omega' \langle \alpha \rangle \right) - \omega' \alpha_r \right] + \frac{1}{T_r} \left(T' \langle Q \rangle + \langle T - T_r \rangle Q' \right)$

(A11.7)

1.6.12 Appendix A12: Total kinetic energy retrieval

We ensure that the computation of time-mean and time-variability kinetic energy budget were correct by summing all their contributions to retrieve the total kinetic energy equation terms obtained in (A1.1).

The sum of conversion and boundary fluxes terms appearing in K_M , K_E , K_{X1} and K_{X2} tendency equations is:

$$\begin{aligned}
 & - \left[\overrightarrow{V_h} \cdot (\overrightarrow{V}' \cdot \vec{\nabla}) \cdot \langle \overrightarrow{V_h} \rangle \right] - \left[\overrightarrow{V_h} \cdot (\overrightarrow{V}' \cdot \vec{\nabla}) \cdot \langle \overrightarrow{V_h} \rangle \right] \\
 & - \left[+\vec{\nabla} \cdot \langle \overrightarrow{V} \rangle K_M \right] - \left[+\vec{\nabla} \cdot \langle \overrightarrow{V} \rangle K_E \right] \\
 & - \left[+\vec{\nabla} \cdot \langle \overrightarrow{V}' \langle \overrightarrow{V}_h \cdot \langle \overrightarrow{V}_h \rangle \rangle \right] - \left[+\vec{\nabla} \cdot \left\langle \overrightarrow{V}' \left(\frac{\overrightarrow{V}_h \cdot \overrightarrow{V}_h}{2} \right) \right\rangle \right] \\
 & - \left[\vec{\nabla} \cdot \left\{ \overrightarrow{V} \left(\frac{1}{2} V_h'^2 \right) - \left\langle \overrightarrow{V} \left(\frac{1}{2} V_h'^2 \right) \right\rangle \right\} + \right] - \left[\vec{\nabla} \cdot \left\{ \overrightarrow{V} \left(K - \frac{1}{2} V_h'^2 \right) - \left\langle \overrightarrow{V} \left(K - \frac{1}{2} V_h'^2 \right) \right\rangle \right\} - \right] \\
 & - \left[\langle \overrightarrow{V}_h' \cdot (\overrightarrow{V}' \cdot \vec{\nabla}) \cdot \langle \overrightarrow{V}_h \rangle - \langle \overrightarrow{V}_h' \cdot (\overrightarrow{V}' \cdot \vec{\nabla}) \cdot \langle \overrightarrow{V}_h \rangle \rangle \right] - \left[\langle \overrightarrow{V}_h' \cdot (\overrightarrow{V}' \cdot \vec{\nabla}) \cdot \langle \overrightarrow{V}_h \rangle - \langle \overrightarrow{V}_h' \cdot (\overrightarrow{V}' \cdot \vec{\nabla}) \cdot \langle \overrightarrow{V}_h \rangle \rangle \right] \\
 & - \left[-\overrightarrow{V}_h' \cdot \langle (\overrightarrow{V}' \cdot \vec{\nabla}) \cdot \overrightarrow{V}_h' \rangle \right] - \left[+\overrightarrow{V}_h' \cdot \langle (\overrightarrow{V}' \cdot \vec{\nabla}) \cdot \overrightarrow{V}_h' \rangle \right] \\
 & = - \left\{ \vec{\nabla} \cdot \langle \overrightarrow{V} \rangle \langle K \rangle + \vec{\nabla} \cdot \langle \overrightarrow{V}' K_X \rangle \right\} - \vec{\nabla} \cdot \left\{ \overrightarrow{V} K - \langle \overrightarrow{V} K \rangle \right\} \\
 & = -\vec{\nabla} \cdot \langle \overrightarrow{V} K \rangle - \vec{\nabla} \cdot \left\{ \overrightarrow{V} K - \langle \overrightarrow{V} K \rangle \right\} \\
 & = -\vec{\nabla} \cdot \langle \overrightarrow{V} K \rangle
 \end{aligned} \tag{A12.1}$$

The sum of contribution of geopotential heights appearing in K_M , K_E , K_{X1} and K_{X2} tendency equations is:

$$\begin{aligned}
& -\langle \vec{V}_h \rangle \cdot \overline{\nabla}_h \langle \phi \rangle - \langle \vec{V}_h' \cdot \overline{\nabla}_h \phi' \rangle - \left(\vec{V}_h' \cdot \overline{\nabla}_h \phi' - \langle \vec{V}_h' \cdot \overline{\nabla}_h \phi' \rangle \right) - \left(\vec{V}_h' \cdot \overline{\nabla}_h \langle \phi \rangle + \langle \vec{V}_h' \cdot \overline{\nabla}_h \phi' \rangle \right) \\
& = -\langle \vec{V}_h \rangle \cdot \overline{\nabla}_h \langle \phi \rangle - \vec{V}_h' \cdot \overline{\nabla}_h \phi' - \left(\vec{V}_h' \cdot \overline{\nabla}_h \langle \phi \rangle + \langle \vec{V}_h' \cdot \overline{\nabla}_h \phi' \rangle \right) \\
& = -\left(\langle \vec{V}_h \rangle \cdot \overline{\nabla}_h \langle \phi \rangle + \langle \vec{V}_h' \cdot \overline{\nabla}_h \phi' \rangle \right) - \left(\vec{V}_h' \cdot \overline{\nabla}_h \phi' + \vec{V}_h' \cdot \overline{\nabla}_h \langle \phi \rangle \right) \\
& = -\langle \vec{V}_h \rangle \cdot \overline{\nabla}_h \phi - \vec{V}_h' \cdot \overline{\nabla}_h \phi \\
& = -\vec{V}_h \cdot \overline{\nabla}_h \phi
\end{aligned} \tag{A12.2}$$

The sum of contribution to the dissipation of the kinetic energy appearing in K_M , K_E , K_{X1} and K_{X2} tendency equations is:

$$\begin{aligned}
& \langle \vec{V}_h \rangle \cdot \langle \vec{F}_h \rangle + \langle \vec{V}_h' \cdot \vec{F}_h' \rangle + \left(\vec{V}_h' \cdot \vec{F}_h' - \langle \vec{V}_h' \cdot \vec{F}_h' \rangle \right) + \left(\vec{V}_h' \cdot \langle \vec{F}_h \rangle + \langle \vec{V}_h' \cdot \vec{F}_h' \rangle \right) \\
& = \langle \vec{V}_h \rangle \cdot \langle \vec{F}_h \rangle + \vec{V}_h' \cdot \vec{F}_h' + \vec{V}_h' \cdot \langle \vec{F}_h \rangle + \langle \vec{V}_h' \cdot \vec{F}_h' \rangle \\
& = \vec{V}_h \cdot \vec{F}_h
\end{aligned} \tag{A12.3}$$

Finally, we retrieve all terms present in (A1.1) and is a confirmation of the robustness of the kinetic energy equations developed in this paper.

1.6.13 Appendix A13: Total kinetic energy retrieval

We ensure that the computation of time-mean and time-variability available enthalpy energy budget were correct by summing all their contributions to retrieve the total kinetic energy equation terms obtained in (A3.8).

The sum of conversion and boundary fluxes terms appearing in A_M , A_E , A_{X1} and A_{X2} tendency equations is:

$$\begin{aligned}
 & \left[-\frac{C_p}{T_r} \left(\langle T' \bar{V}' \rangle \cdot \bar{\nabla} \right) \langle T \rangle \right. \\
 & - \left[+\bar{\nabla} \cdot \left(\langle \bar{V} \rangle A_M \right) \right. \\
 & \left. \left. +\bar{\nabla} \cdot \left\langle \bar{V}' \left(\frac{C_p}{T_r} \langle T - T_r \rangle T' \right) \right\rangle \right] \right. \\
 & \left. \left[\frac{C_p}{T_r} \left(\langle T' \bar{V}' \rangle \cdot \bar{\nabla} \right) \langle T \rangle \right. \right. \\
 & \left. \left. +\bar{\nabla} \cdot \left(\langle \bar{V} \rangle A_E \right) \right. \\
 & \left. \left. +\bar{\nabla} \cdot \left\langle \bar{V}' \left(\frac{C_p}{2T_r} T'^2 \right) \right\rangle \right] \right. \\
 & \left. \left[\bar{\nabla} \cdot \left\{ \bar{V} \left(\frac{C_p}{2T_r} T'^2 \right) - \left\langle \bar{V} \left(\frac{C_p}{2T_r} T'^2 \right) \right\rangle \right\} \right. \right. \\
 & \left. \left. - \bar{\nabla} \cdot \left\{ \bar{V} \left(A - \frac{C_p}{2T_r} T'^2 \right) - \left\langle \bar{V} \left(A - \frac{C_p}{2T_r} T'^2 \right) \right\rangle \right\} \right] \right. \\
 & \left. \left[-\frac{C_p}{T_r} \left\{ \left(T' \bar{V}' \cdot \bar{\nabla} \right) \langle T \rangle - \left\langle \left(T' \bar{V}' \cdot \bar{\nabla} \right) \langle T \rangle \right\rangle \right\} \right. \right. \\
 & \left. \left. - \frac{C_p}{T_r} T' \left\langle \left(\bar{V}' \cdot \bar{\nabla} \right) T' \right\rangle \right] \right. \\
 & = -\bar{\nabla} \cdot \left\{ \langle \bar{V} \rangle \langle A \rangle - \langle \bar{V}' A_x \rangle \right\} - \bar{\nabla} \cdot \left\{ \bar{V} A - \langle \bar{V} A \rangle \right\} \\
 & = -\bar{\nabla} \cdot \langle \bar{V} A \rangle - \bar{\nabla} \cdot \left\{ \bar{V} A - \langle \bar{V} A \rangle \right\} \\
 & = -\bar{\nabla} \cdot (\bar{V} A)
 \end{aligned} \tag{A13.1}$$

The sum of terms contributing to the diabatic heating in K_M , K_E , K_{X1} and K_{X2} tendency equations is:

$$\begin{aligned}
& \left\langle \left(\frac{T}{T_r} - 1 \right) \right\rangle \langle Q \rangle + \left\langle \frac{T'Q'}{T_r} \right\rangle + \frac{1}{T_r} \{ T'Q' - \langle T'Q' \rangle \} + \frac{1}{T_r} (T' \langle Q \rangle + \langle T - T_r \rangle Q') \\
&= \left\langle \left(\frac{T}{T_r} - 1 \right) \right\rangle \langle Q \rangle + \frac{T'Q'}{T_r} + \frac{1}{T_r} (T' \langle Q \rangle + \langle T - T_r \rangle Q') \\
&= \frac{1}{T_r} \{ \langle T \rangle \langle Q \rangle + T'Q'T' \langle Q \rangle + \langle T_r \rangle Q' \} - \{ \langle Q \rangle + Q' \} \\
&= \frac{1}{T_r} TQ - Q \\
&= \left(\frac{T}{T_r} - 1 \right) Q
\end{aligned} \tag{A13.2}$$

We retrieve all terms present in (A1.2); this confirms the robustness of the available enthalpy equations developed in this paper.

1.6.14 Appendix A14: Link between C_E and C_A 's vertical component

The vertical component of C_A in pressure coordinates can be rewritten as follows:

$$\begin{aligned}
 C_{A_p} &= -\frac{C_p}{T_r} \left\langle T' \omega' \right\rangle \left\langle \frac{\partial T}{\partial p} \right\rangle \\
 &= -\frac{p C_p}{RT_r} \left\langle \frac{RT'}{p} \omega' \right\rangle \left\langle \frac{\partial T}{\partial p} \right\rangle \\
 &= -\frac{p C_p}{RT_r} \left\langle \omega' \alpha' \right\rangle \left\langle \frac{\partial T}{\partial p} \right\rangle \\
 &= \frac{p C_p}{RT_r} \left\langle \frac{\partial T}{\partial p} \right\rangle * C_E
 \end{aligned} \tag{A14.1}$$

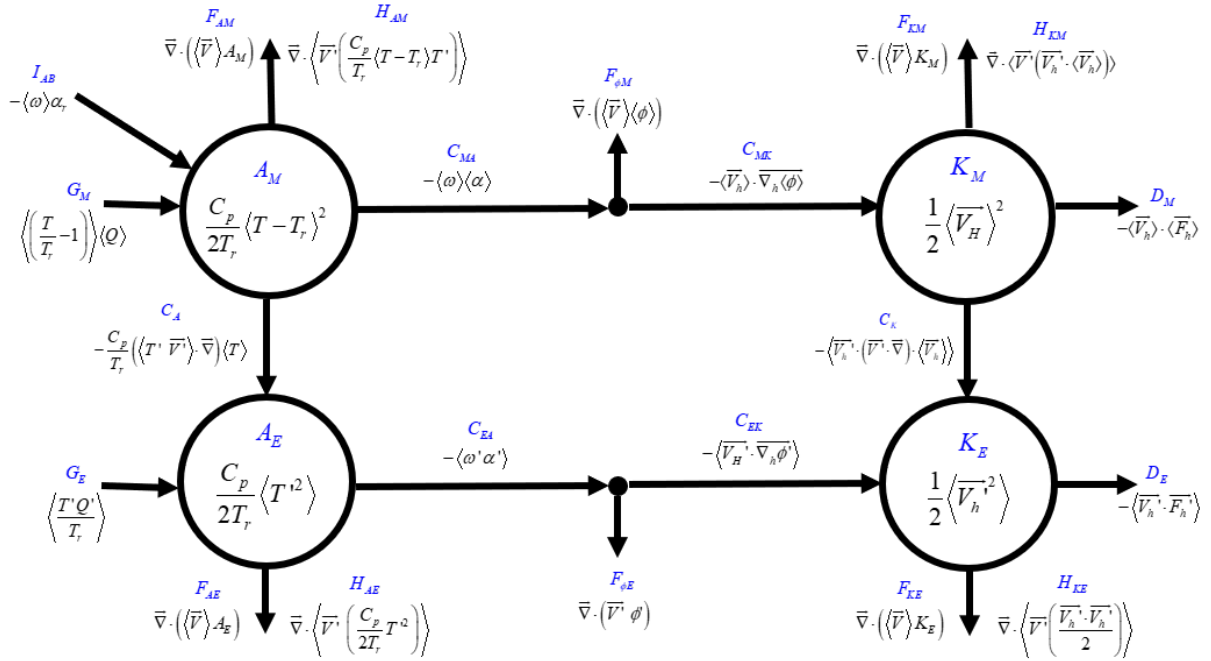


Figure 1-1: Climate energy cycle. Boxes represent the different energy reservoirs and arrows the various sources/sinks of energy acting on them.

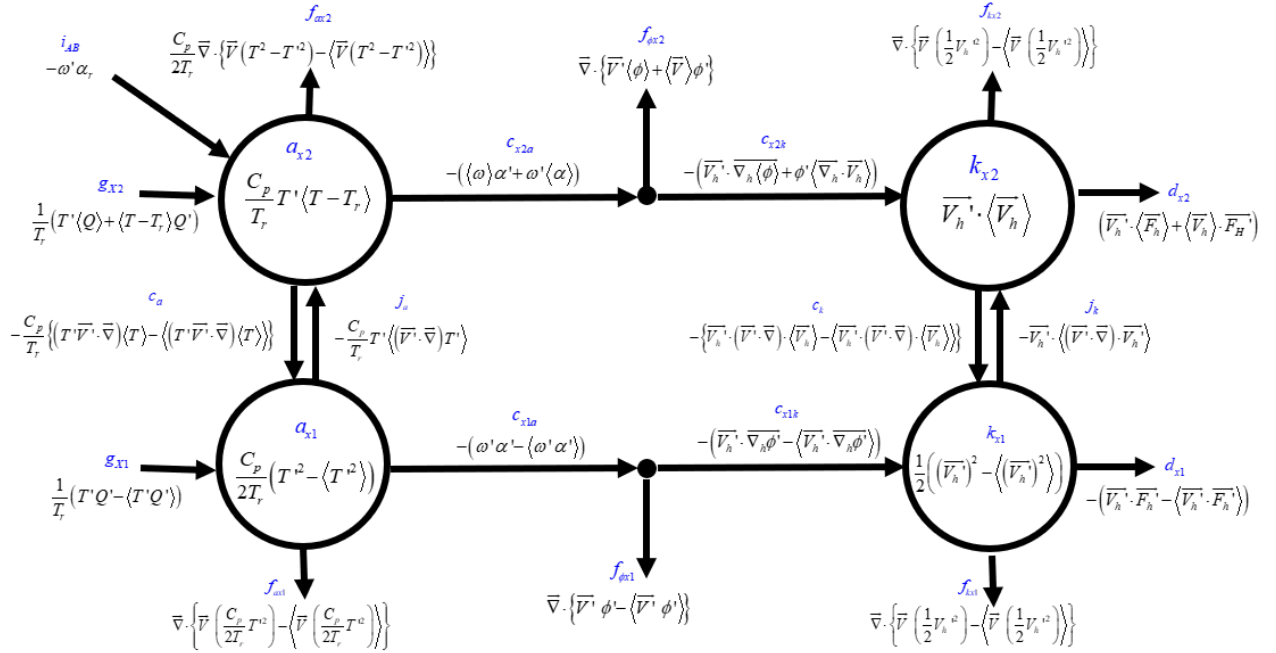


Figure 1-2: Storm energy cycle. Boxes represent the different energy reservoirs and arrows the various sources/sinks of energy acting on them.

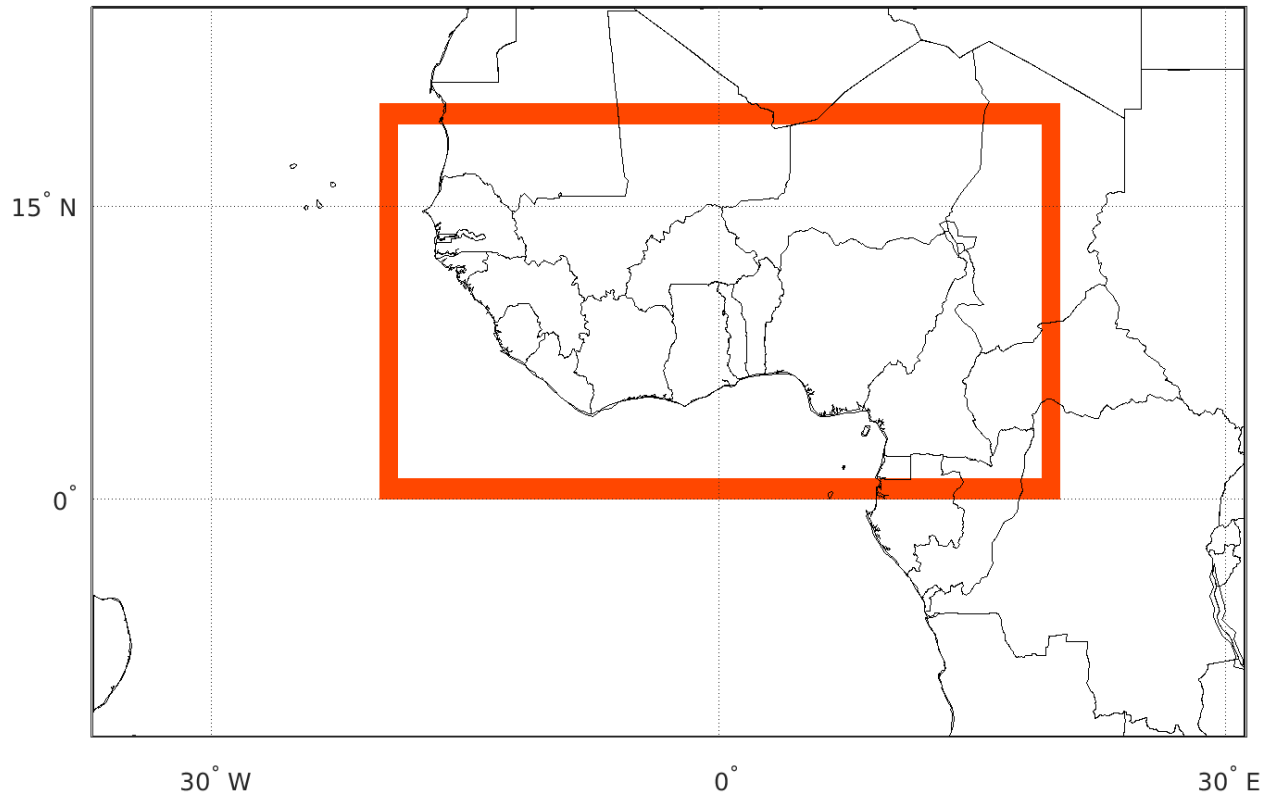


Figure 1-3: Free domain excluding, 10 grid-point-wide semi-Lagrangian halo and 10 grid-point-wide lateral Davies' sponge zone, contains 620*340 grid points. The red band delimits our main West Africa study domain [20°W–20°E; 0–20°N].

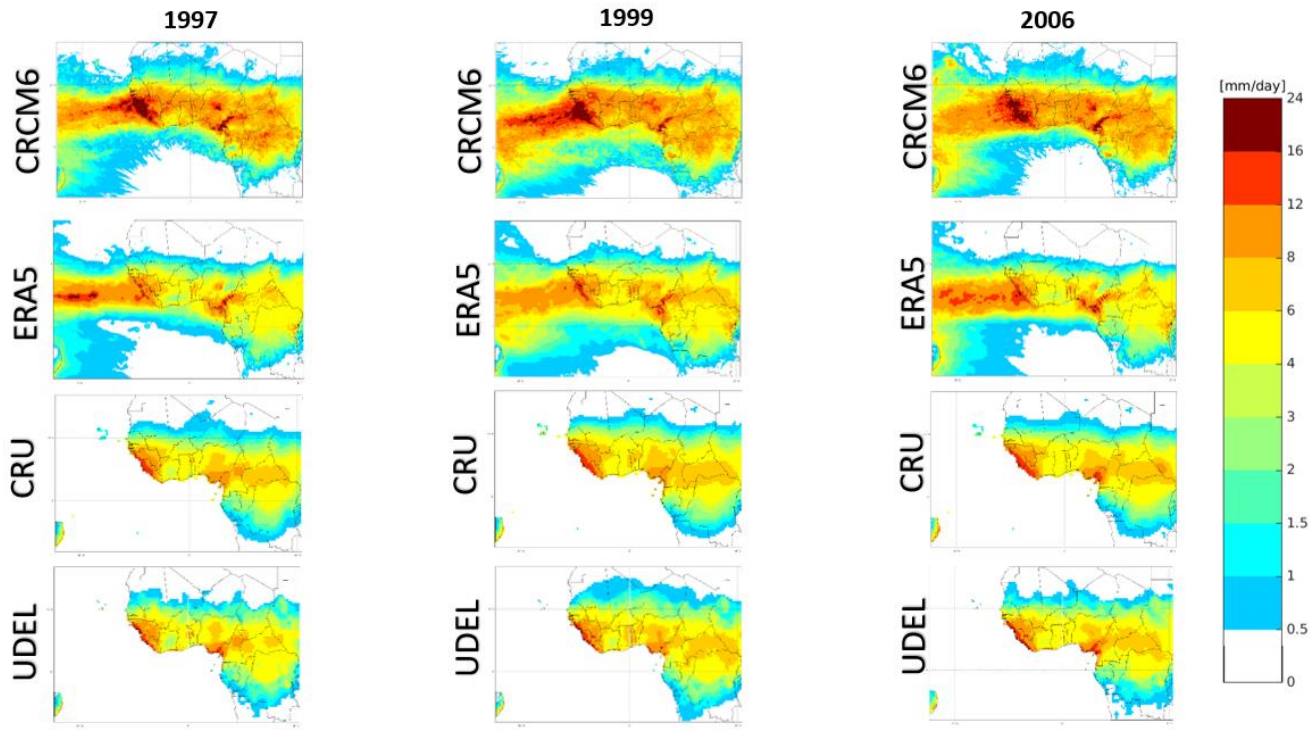


Figure 1-4: Mean (May to September) precipitation for 1997 (dry year), 1999 (humid year) and 2006 (normal year) from CRCM6, ERA5, CRU and UDEL in mm/day.

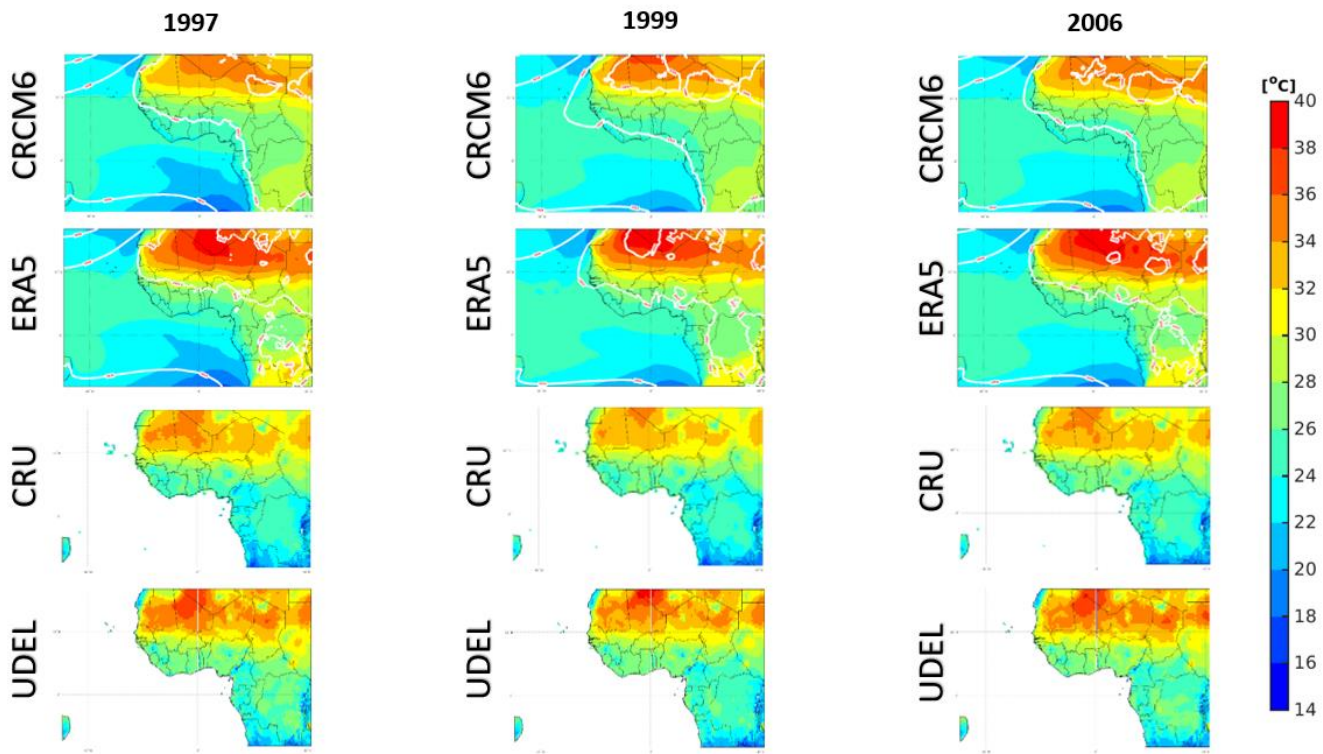


Figure 1-5: May to September mean surface temperature (colors, in °C) and mean sea level pressure (white contour, in hPa) for 1997 (dry year), 1999 (humid year) and 2006 (normal year) from ERA5, CRCM6, CRU and UDEL.

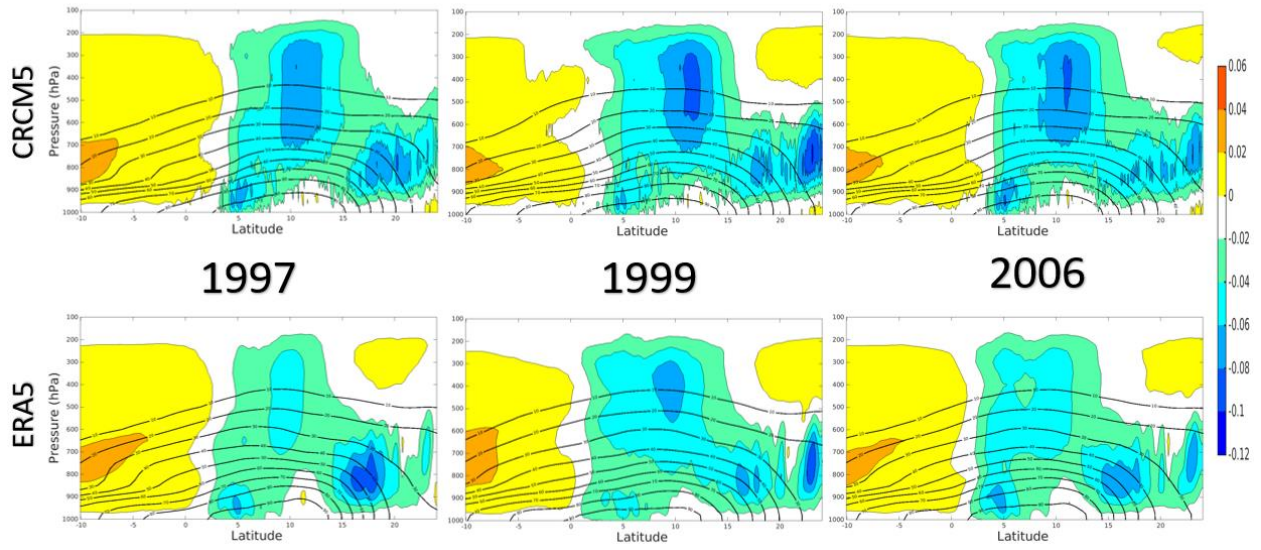


Figure 1-6: Vertical latitude cross-section of May to September averaged vertical velocity, negative (positive) values are upward (downward) motion (colors, in Pa/s) and relative humidity (black contour, in %) averaged in the longitude 10°W - 10°E , from CRCM6 (top) and ERA5 (bottom).

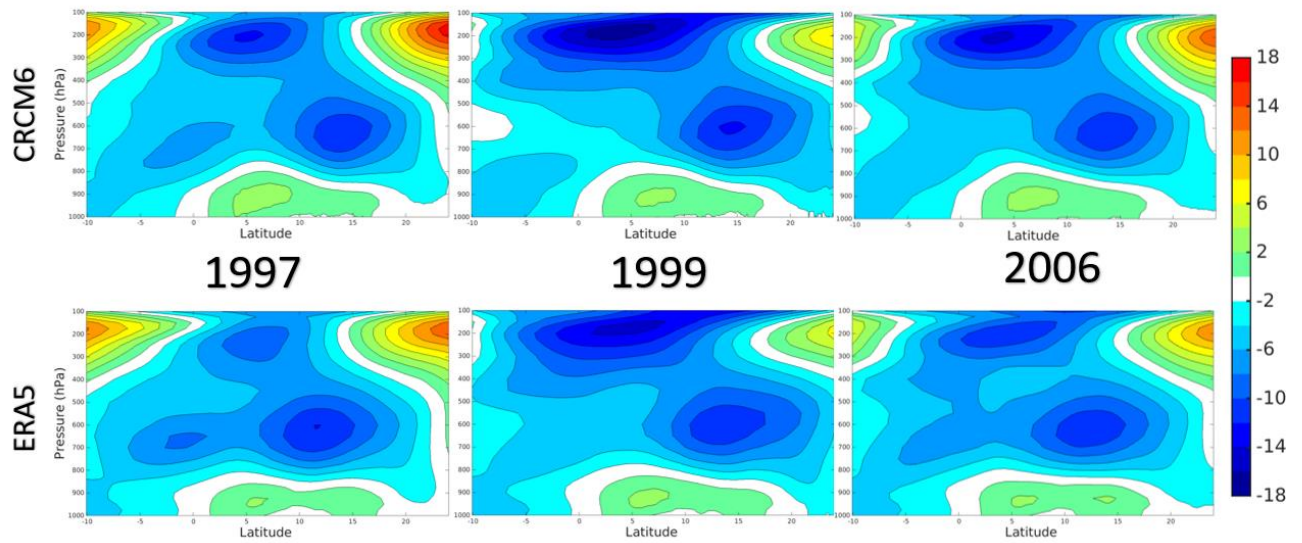


Figure 1-7: Vertical latitude cross-section of May to September averaged zonal wind (colors, in m/s), averaged in the longitude $10^{\circ}\text{W} - 10^{\circ}\text{E}$, from CRCM6 (top) and ERA5 (bottom).

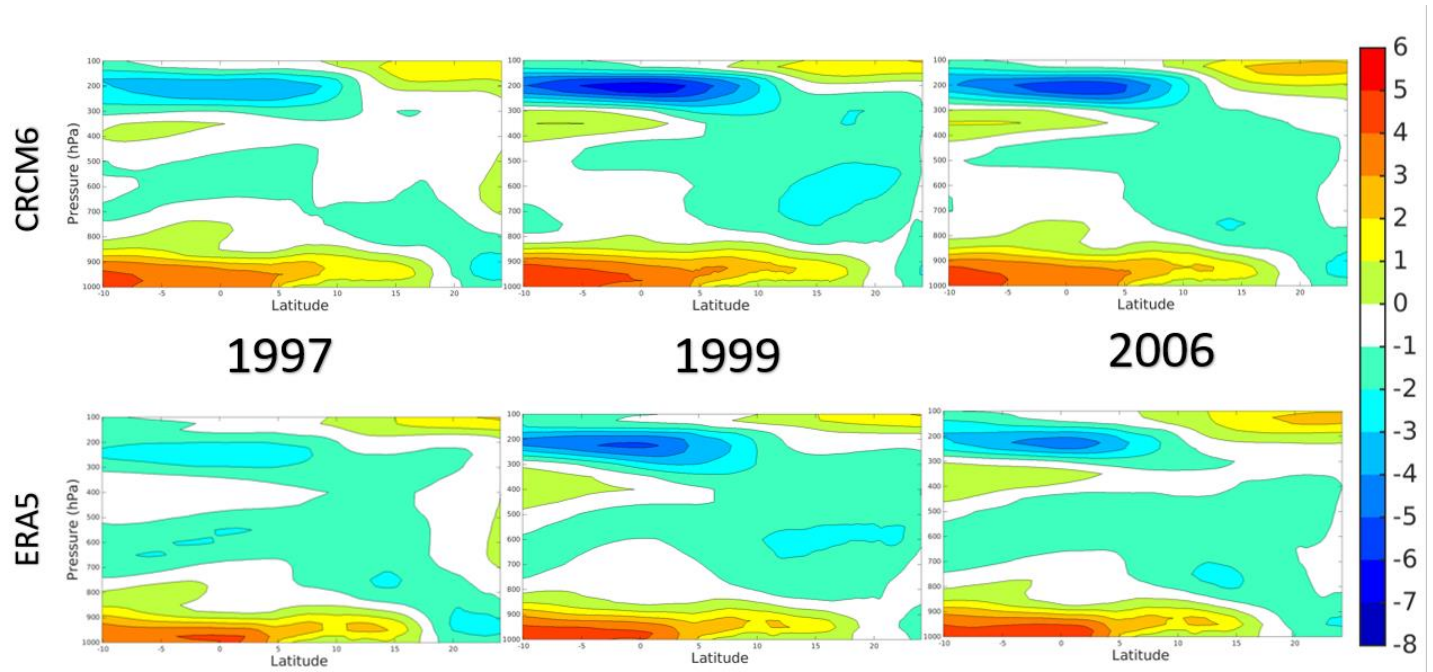
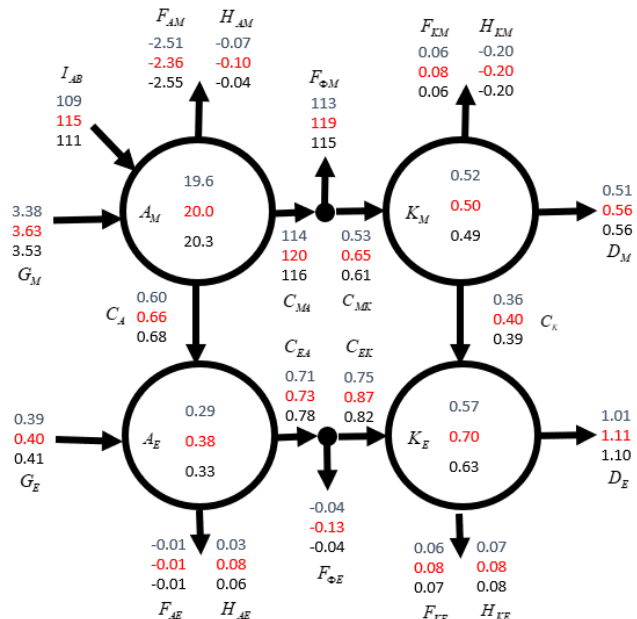


Figure 1-8: Vertical latitude cross-section of May to September averaged meridional wind (colors, in m/s), averaged in the longitude $10^{\circ}\text{W} - 10^{\circ}\text{E}$, from CRCM6 (top) and ERA5 (bottom).

CRCM6



ERA5

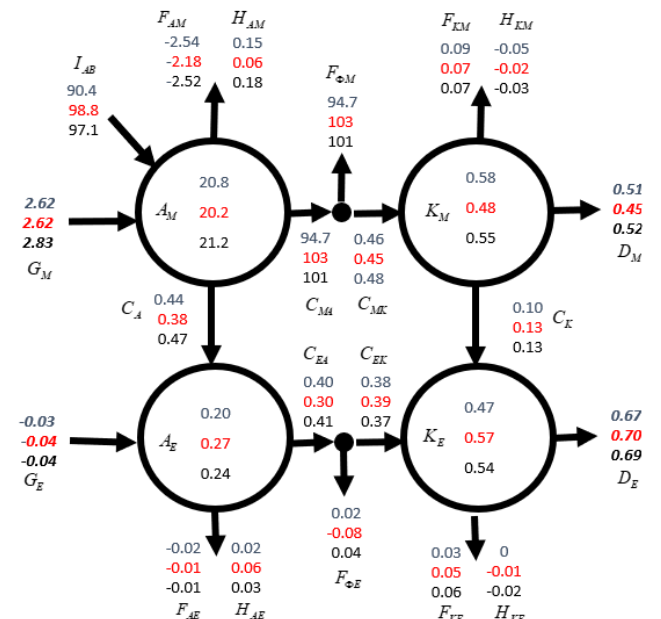


Figure 1-9: Vertically integrated time- and domain-averaged climate energy cycle for 1997 (dry-year, blue values, up), 1999 (wet-year, red values, middle) and 2006 (normal-year, black values, down). Energy reservoirs (boxes) are shown in 10^5 J m^{-2} and energy fluxes (arrows) in W m^{-2}

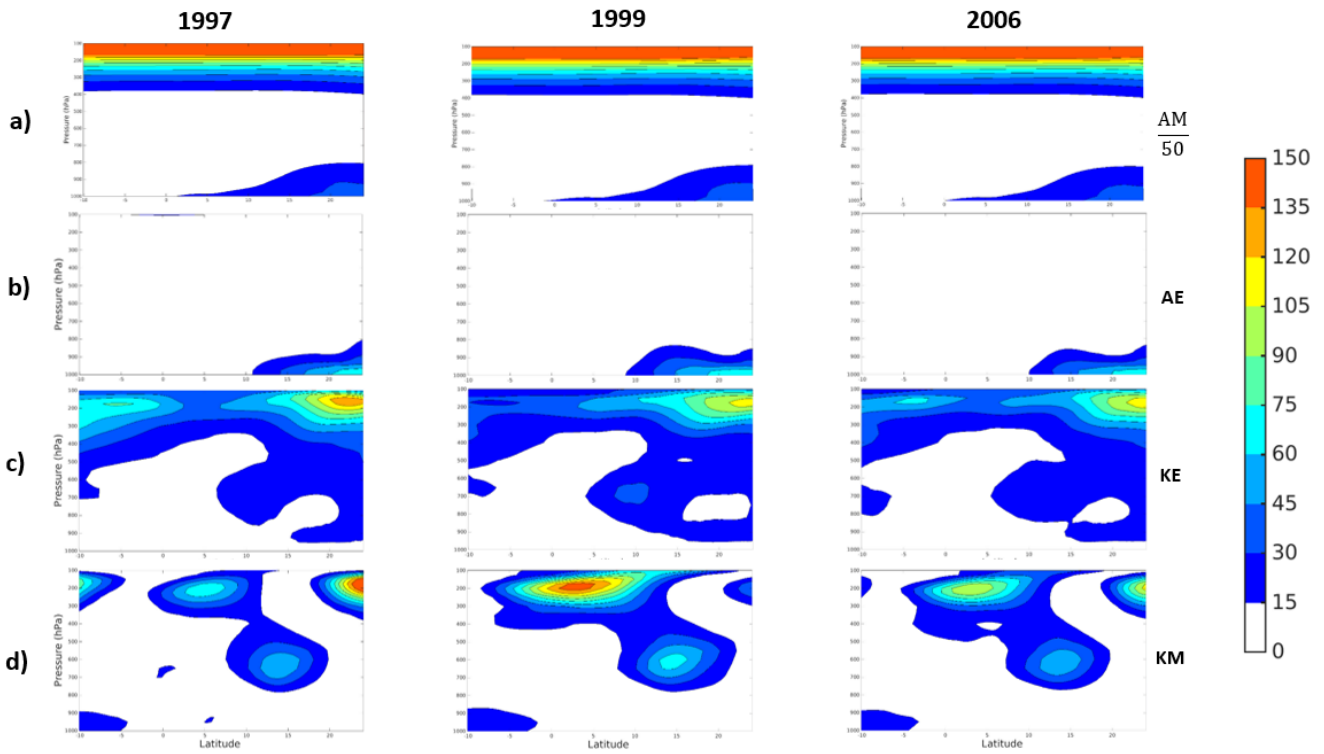


Figure 1-10: Vertical latitude cross-section of a) A_M (divided by 50 for uniformity), b) A_E , c) K_E and d) K_M averaged in the longitude $10^\circ\text{W} - 10^\circ\text{E}$. Values are in $\text{J} \cdot \text{kg}^{-1}$.

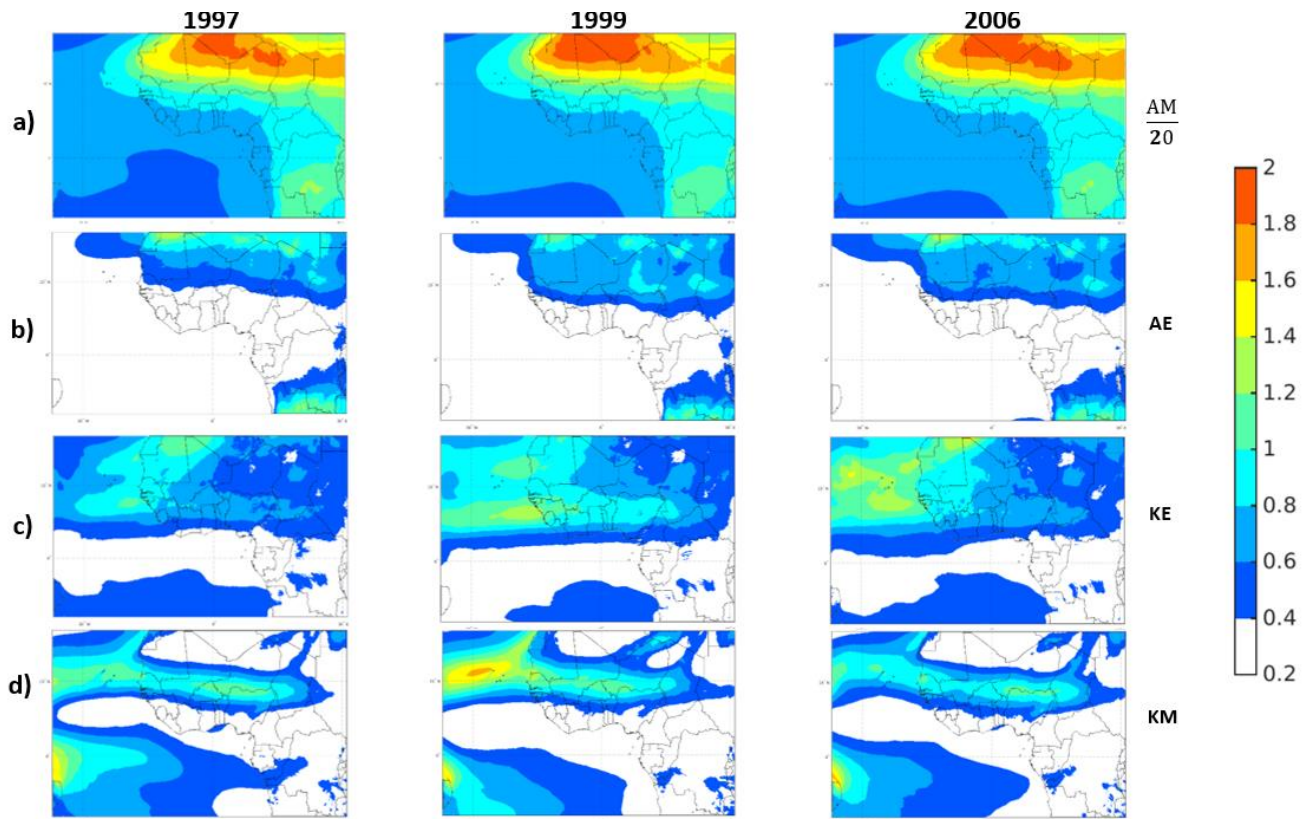


Figure 1-11: Maps of vertically integrated of a) A_M (divided by 20 for uniformity), b) A_E , c) K_E and d) K_M . Values are in 10^5 J.m^{-2} .

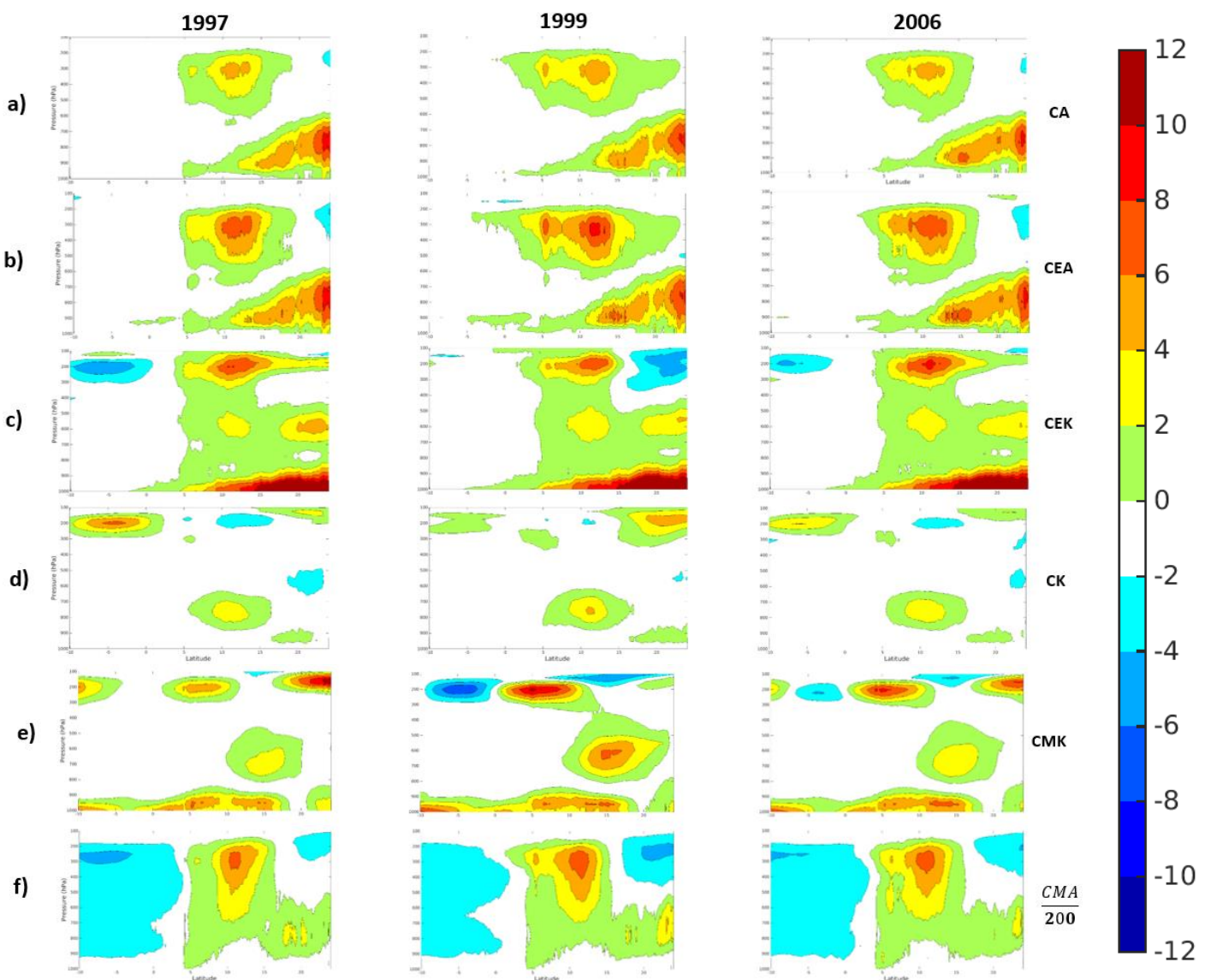


Figure 1-12: Vertical latitude cross-section of a) CA, b) CEA, c) CEK, d) CK, e) CMK and f) CMA (divided by 200 for uniformity) averaged in the longitude $10^{\circ}\text{W} - 10^{\circ}\text{E}$. Values are in $10^{-4} \text{ W} \cdot \text{kg}^{-1}$

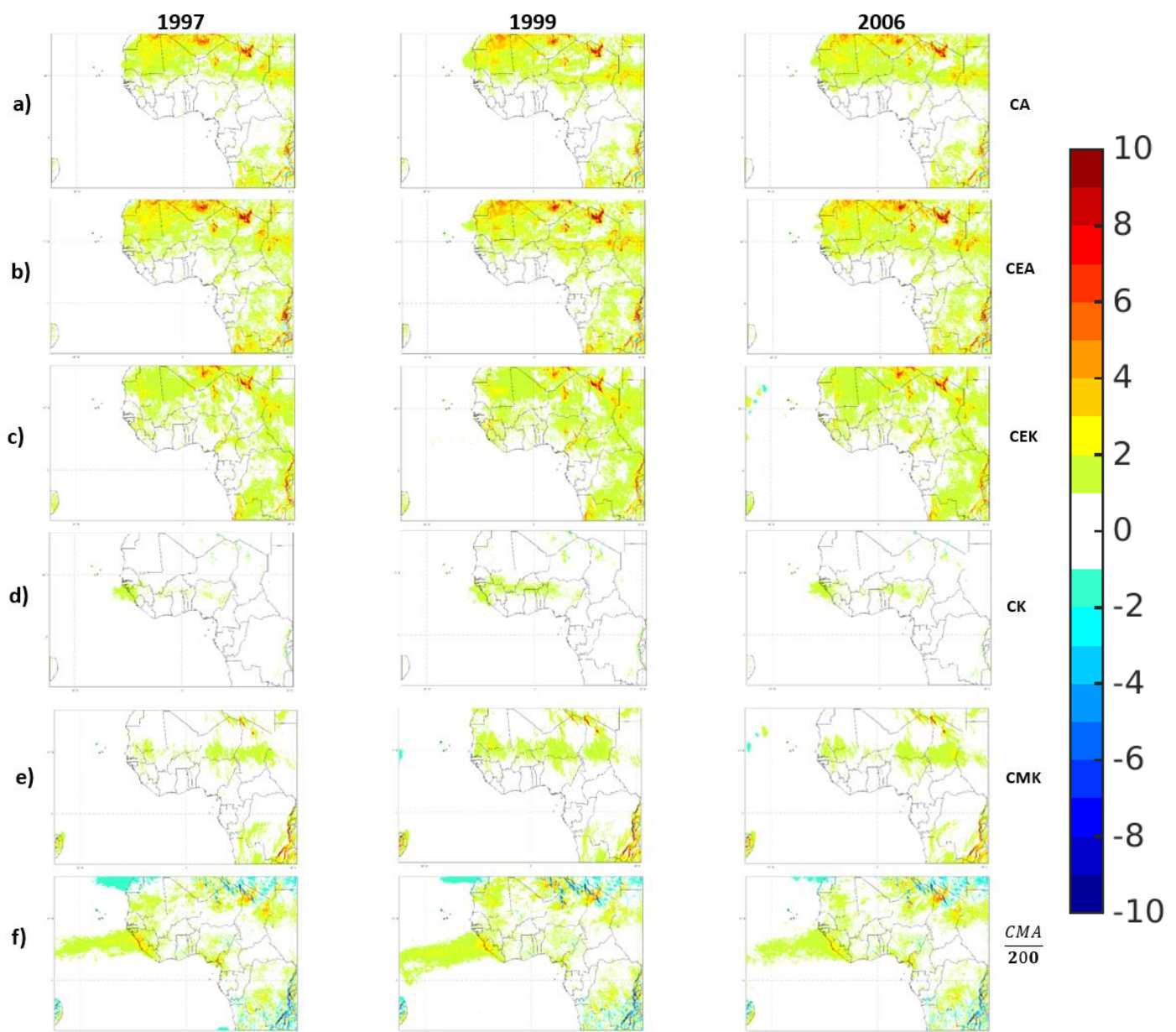


Figure 1-13: Maps of vertically integrated conversion of a) C_A , b) C_{EA} , c) C_{EK} , d) C_K e) C_{MK} and f) C_{MA} (divided by 200 for uniformity) . Values are in $W \cdot m^{-2}$.

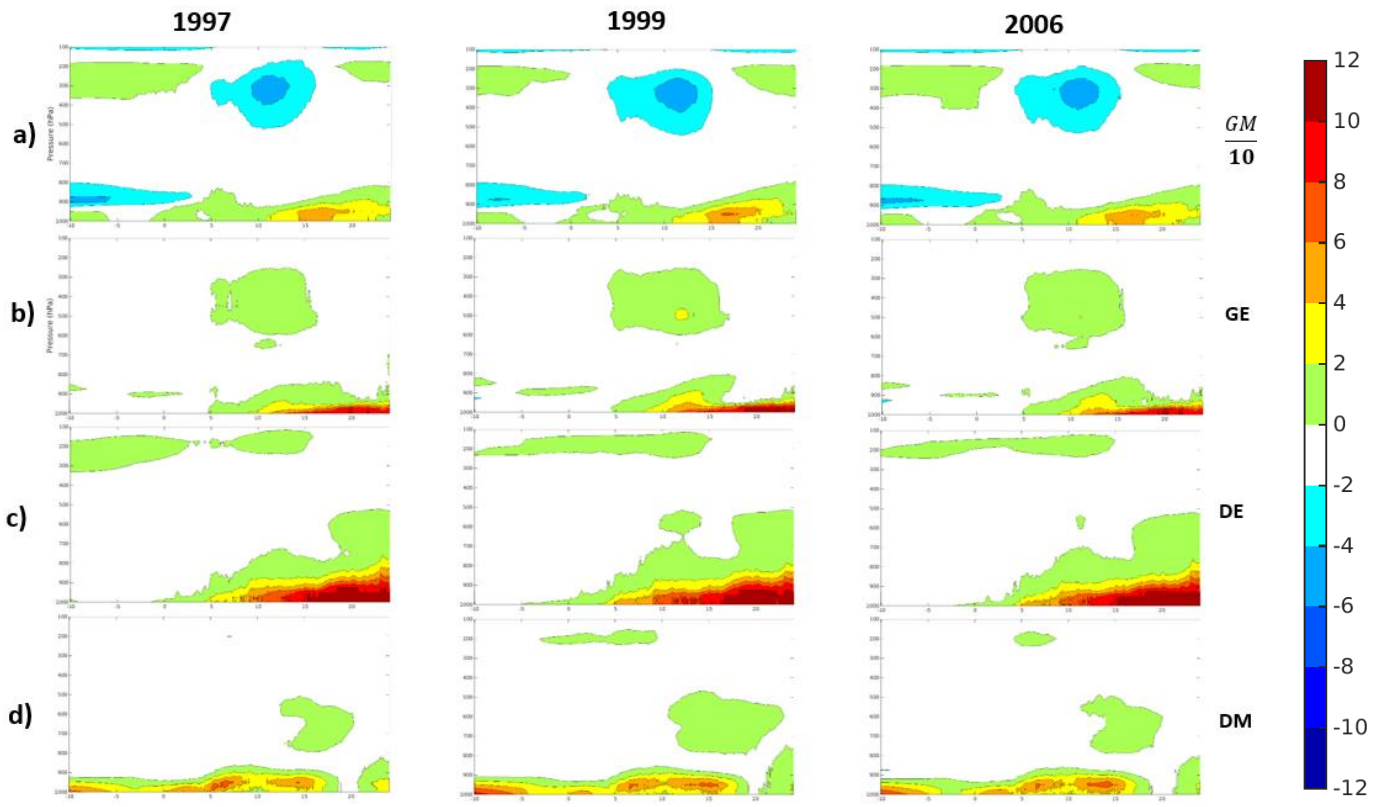


Figure 1-14: Vertical cross-section of a) GM (divided by 10 for uniformity), b) GE , c) DE and d) DM , averaged in the region between $10^{\circ}\text{W} - 10^{\circ}\text{E}$ and $10^{\circ}\text{S} - 25^{\circ}\text{N}$. Values are in $10^{-4} \text{ W.kg}^{-1}$.

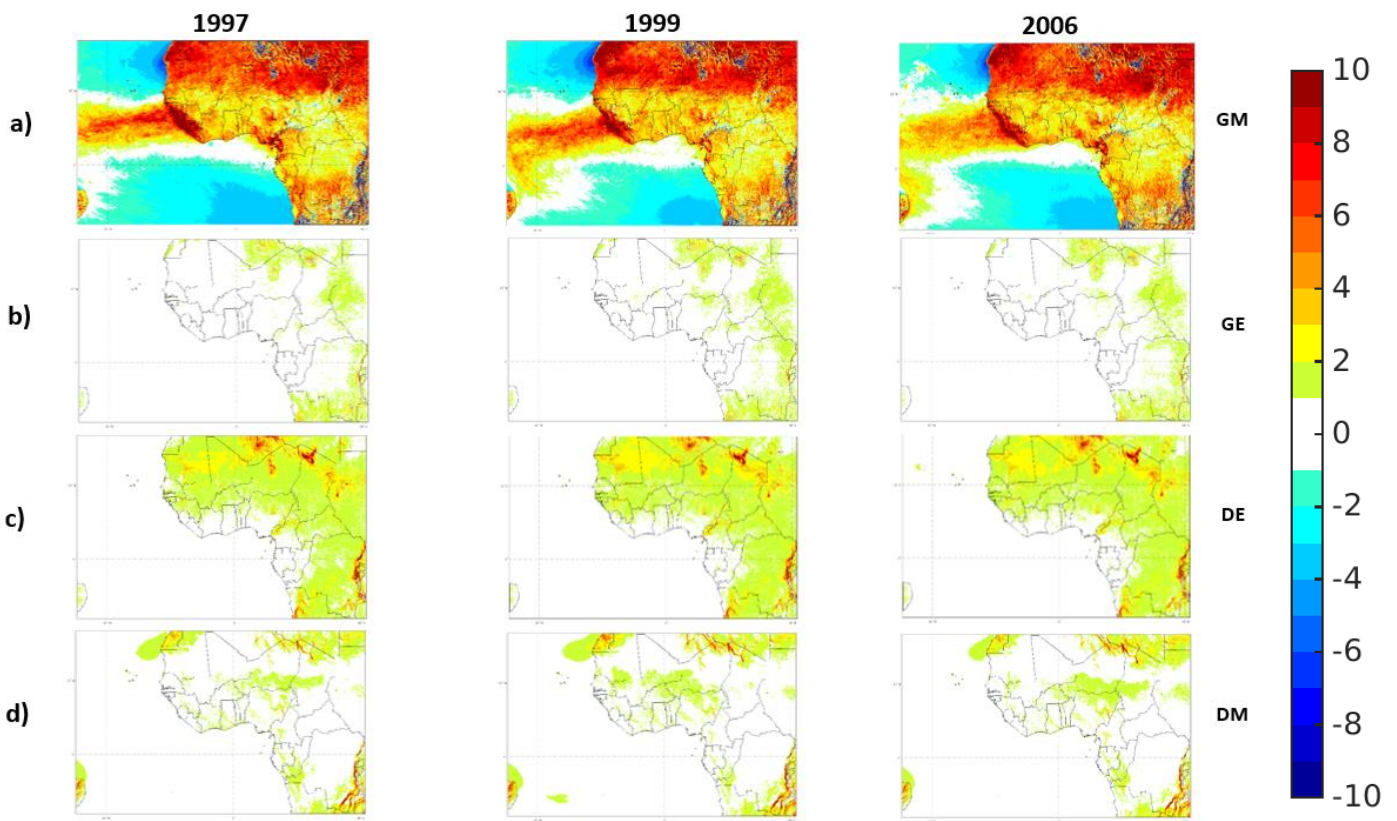


Figure 1-15: Maps of vertically integrated a) G_M , b) G_E , c) D_E and d) D_M . Values are in $\text{W} \cdot \text{m}^{-2}$.

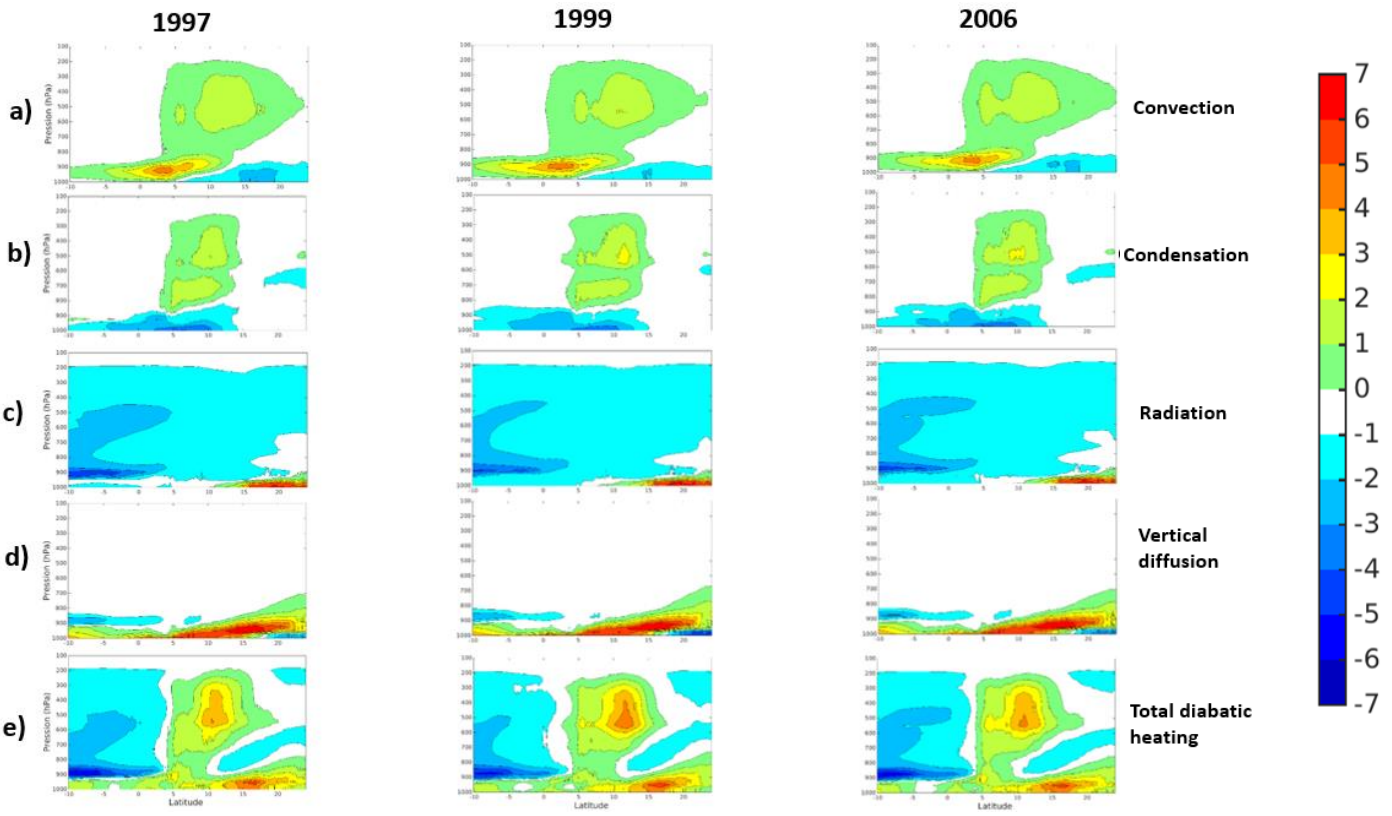


Figure 1-16: Vertical latitude cross-section of a) convection contribution, b) condensation contribution, c) radiation contribution, d) vertical diffusion contribution and e) total diabatic heating averaged in the longitude $10^{\circ}\text{W} - 10^{\circ}\text{E}$. Values are in $\text{K} \cdot \text{day}^{-1}$.

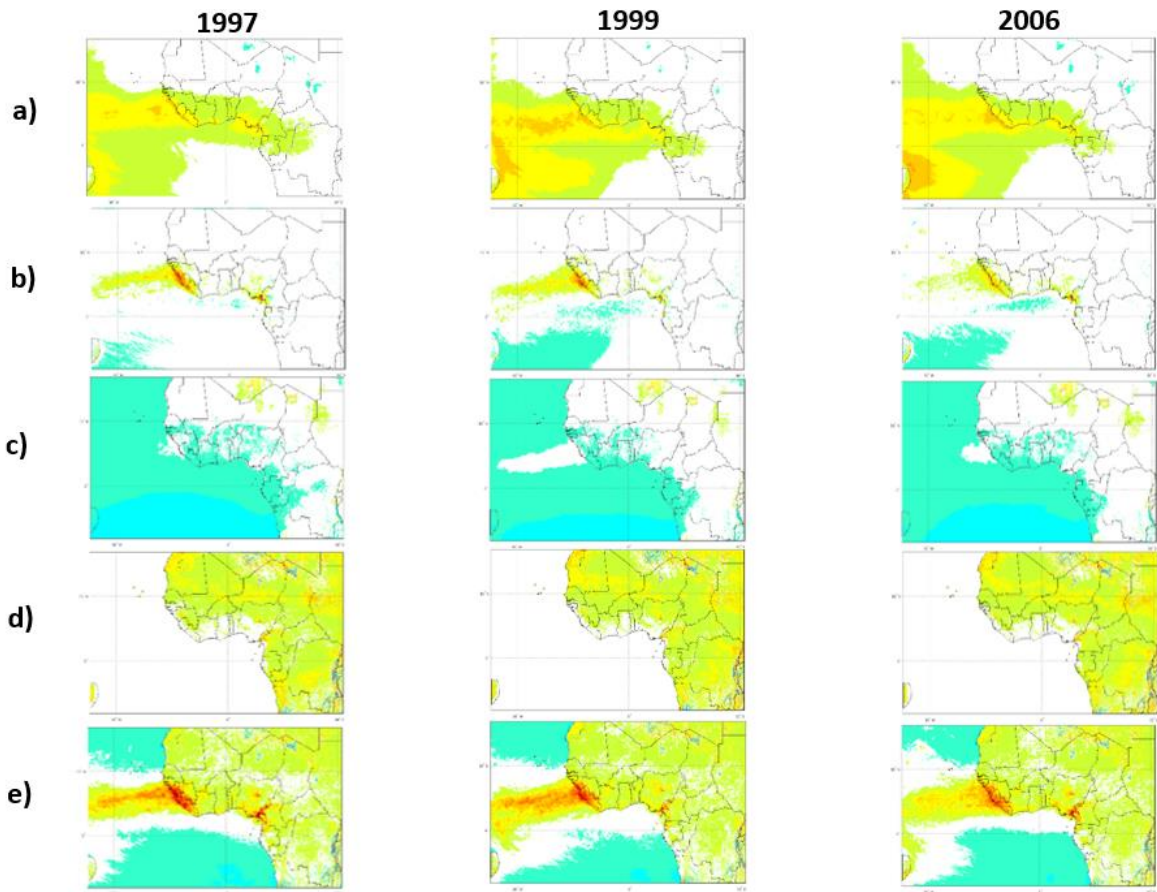


Figure 1-17: Maps of vertically integrated a) convection contribution, b) condensation contribution, c) radiation contribution and d) vertical diffusion contribution and e) total diabatic heating rate. Values are in K/day.

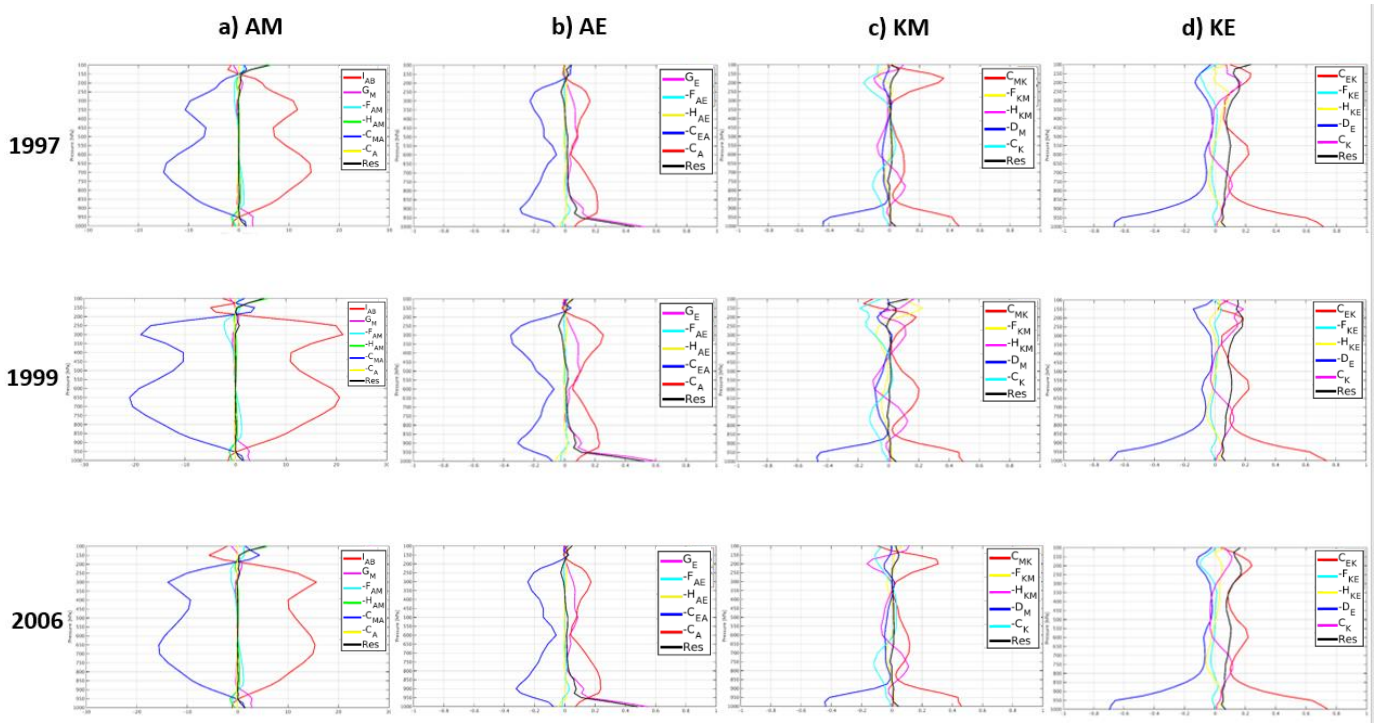


Figure 1-18: Vertical profiles of time- and study domain (20°W – 20°E ; 0 – 20°N)-averaged fluxes acting on energy reservoirs of a) AM, b) AE, c) KM and d) KE, values are in 10^{-3} W/Kg.

CHAPITRE 2

Energetic study of an African wave simulated by the CRCM6 using regional transient-eddy budget equations

Ce chapitre est la version préliminaire d'un article à soumettre dans *Climate Dynamics*.

Y. Ngueto and R. Laprise. 2023. "Energetic study of an African wave simulated by the CRCM6 using regional transient-eddy budget equations". *To be submitted to Climate Dynamics*.

Abstract

The recent development of detailed energy budget formulation suitable for limited-area domain allows the studies of synoptic disturbances such as African Easterly Waves (AEWs). In this study, we follow the evolution of AEWs originating from the South Sudan and crossing the West African coast during three contrasting summers (1997-dry, 1999-wet and 2006-normal), using simulations of the sixth-generation Canadian Regional Climate Model (CRCM6). A case study was chosen based on the assumption that an AEW generated with a large amount of kinetic energy has more chance to persist while crossing the continent and develop into an extra tropical depression while reaching the west coast. The selected wave has been found in the literature as a tropical cyclone associated with the genesis of Hurricane Alberto and constitutes an ideal case study of the life cycle of an intense AEW using transient-eddy kinetic energy budget equations. The computation of the energy budget of an AEW show that the transient-eddy available enthalpy (AX_1) and kinetic energy (K_{X1}) are highly correlated in the Sahel until the wave reaches the Atlantic. The flux of transient-eddy geopotential heights acting in the lateral boundaries is the only physical process that could amplify or dampen conversions of AX_1 into K_{X1} in a regional domain.

Key words: Atmospherics energetics, AEWs, Regional climate model.

2.1 Introduction

African Easterly Waves (AEWs) are the main synoptic weather systems bringing rain in West Africa. Their discovery was made by two German meteorologists, Regula and Piersig. (Regula,

1943) studied large-scale pressure changes in West Africa in relation to the wind changes. He found that "tornadoes" (squall lines) occur between a falling pressure tendency followed by a rising tendency. (Piersig, 1944) made a systematic review of "Hoffmeyer Charts" in the eastern North Atlantic. He found a low pressure in the West African coast between 5° and 20° N, which moved westward usually along the southern edge of the trade-wind belt. Because of lack of observations from the interior of Africa, (Piersig, 1944) could not say more about the real course of cyclogenesis in West African "tornado" systems. However, the origin and tracks of AEWs over the African continent were still not identified and the link between AEW-like disturbances and Atlantic tropical cyclones remained largely speculative (Fink, 2012).

(Burpee, 1972) used power spectrum method on weather charts to investigate the origin and structure of AEWs. He found that AEWs propagate westward with a periodicity of 3-5 days, with wind perturbations maximum amplitude of 1-2 m/s near 700 hPa, and originate between Khartoum (32°E) and Ft. Lamy (15°E) as a consequence of the instability of the African Easterly Jet (AEJ). This instability behaviour of the AEWs has been investigated by (Thorncroft, CD et Hoskins, 1994a, 1994b) in a dry model. It appears that AEWs may arise through a mixed barotropic/baroclinic instability mechanism, with easterly waves initially dominated by barotropic energy conversions, but later growing mainly through baroclinic energy conversions. However, it seems that shear instability alone cannot explain the initiation of AEWs (Hall *et al.*, 2006; Kiladis *et al.*, 2006).

Other authors linked the AEWs initiation to the convection. (Carlson, 1969) took advantage of the advent of satellites to examine the evolution of cloudiness and convection and the intensification of four major AEWs, three of which later became Atlantic hurricanes. (Mass, 1979) suggested an important role for convection in extending and coupling the influence of the disturbances away from the jet level, where barotropic instability appears to dominate. (Berry et Thorncroft, 2005) studied an intense AEW that strongly suggests that the genesis of this AEW is associated with a convective burst over Darfur. (Thorncroft, C. D. *et al.*, 2008) promoted the view that AEWs are triggered by localized forcing, most likely associated with latent heating upstream of the region of observed AEW growth. In this same vein, (Hsieh et Cook, 2007) argued that a connection between the waves and the ITCZ implies that baroclinic conversions provide the primary wave energy, while a connection with the jet implies that barotropic

conversions dominate. Numerous recent studies have shown that AEWs are intimately linked with diabatic processes (Berry et Thorncroft, 2012; Cornforth *et al.*, 2009; Poan *et al.*, 2015; Poan *et al.*, 2013; Russell *et al.*, 2020; Tomassini *et al.*, 2017).

Atmospheric energetics offer a quantitative approach to shed light on the physical processes responsible for AEWs, through a detailed analysis of the transient-eddy energy budget equations. The aim of this paper is to diagnose a simulation of the sixth-generation Canadian Regional Climate Model (CRCM6), using a transient-eddy energetics equation developed in Chapter 1. This case study will benefit from the higher resolution and model physics output terms, not available in the reanalysis data set, in order to improve our understanding of the physical processes responsible for AEWs. The paper is organised as follows. Section 2 presents the methodology employed for the detection of AEWs, the selection criteria used for the case study and the energy budget equations for time-evolving disturbances. Section 3 will present an analysis of terms during the development, growth and decay of the wave. Section 4 will summarise and conclude the paper.

2.2 Methodology

A detailed description of the CRCM6 model configuration and the ERA5 reanalysis providing lateral boundary conditions and used for the evaluation are given in Chapter 1 that focussed on time-mean terms of the energy budget to improve our current knowledge of the West Africa climate. This paper also investigated the energetics differences between three contrasting summers (dry, rainy and moderate). In this study, we want to select a case study among different AEWs crossing the continent during these three contrasting years. We will be particularly interested in conditions that favour the transition of AEWs into extratropical systems. In this paper, we will apply the energy budget equations developed in Chapter 1 to understand mechanisms responsible of the generation and the development of AEWs.

2.2.1 Detection of African Easterly Waves

In the literature, AEWs are mostly detected using a Hovmöller diagram of either the meridional wind (Diedhiou—A *et al.*, 1999; Patricola *et al.*, 2018) or relative vorticity (Brammer et Thorncroft, 2015; Lin *et al.*, 2013). In fact, AEWs signature consists in an alternance of southerly

cool humid air from the Gulf of Guinea and northerly hot dry air from the Sahara Desert. This characteristic is clearly visible with meridional wind diagrams above the boundary layer. Furthermore, the AEJ, an important feature of the African monsoon, propagates from east to west crossing troughs and ridges, with meanders visible using relative vorticity diagrams between 700 and 600 hPa.

Figs. 2-1a and b show respectively a longitude-time Hovmöller diagram of meridional wind and relative vorticity at 700 hPa, averaged over the Sahel latitudinal band (5-15°N). In both diagrams, AEWs are associated with positive/negative band shape propagating from east to west, indicating southerly/northerly winds and cyclonic/anticyclonic curvatures. It can be seen that longer-lasting systems correspond to the more intense ones. The Hovmöller diagram of relative vorticity (Figs. 2-1b) offer the best view of AEWs. In 1997 (a dry year), successive red and blues strip are visible West of 15°W (over the Atlantic Ocean) from middle of July. This is a late start of the rainy season, which normally occurs around the June 24 (Laux *et al.*, 2008). This late start confirms the dry monsoon season, which is a disaster for many families living from agriculture. In 1999 (a humid year) and 2006 (a near-normal year), long strips are visible from the end of May 1999, especially in the relative vorticity diagram.

At first glance, Hovmöller diagrams of the relative vorticity and meridional winds are powerful tools to capture AEWs. However, the quality of diagrams is not always ideal for individual AEW identification. In this study, we use another variable taking part to the transient-eddy energy budget and holding the benefits of both meridional winds and relative vorticity: a derivative of the transient-eddy kinetic energy defined in Chapter 1:

$$k_{x1} = \frac{1}{2} \left[\left(u'^2 + v'^2 \right) - \langle u'^2 + v'^2 \rangle \right] \quad (2.1)$$

a variable that, by definition, vanishes when averaged in time. The brackets in (2-1) denote time averaging and the prime the deviation from the time mean.

In West Africa, the wind structure is quite zonal, allowing k_{x1} to have important values where meridional wind variations are maximum. Moreover, when the zonal AEJ wind structure crosses

the wave, maximum wind deviations occur close to the trough and ridges. The fact that, in the definition of k_{x1} , the time-mean eddy kinetic energy is removed from the transient-eddy kinetic energy, guarantees that storms are associated with positive values of k_{x1} .

Due to the fact that our interest is on AEW with an average period of 3-5 days (Diedhiou, Diedhiou, A et al., 1999; Reed et al., 1977), we will apply a 3-5 days band-pass filter to the zonal and the meridional winds, in order to remove the variability not related to AEW.

Panels a of Figs 2-2 to 2-4 show longitude-time Hovmöller diagrams of vertically integrated k_{x1} of band-pass filtered winds, for 1997, 1999 and 2006, respectively. The panels b of Fig. 2-4 show maps of the vertically integrated k_{x1} superimposed to 700-hPa filtered winds, at eight (8) selected times corresponding to most intense events identified using the Hovmöller diagram.

Fig. 2-2 shows that in 1997 (a dry year), the wave season starts later than other years, with the first AEW occurring at the end of June. The snapshot of the 24/06/1997 at 1pm (Fig. 2-2b) shows lower k_{x1} values associated with an important anticyclone on the Atlantic coast, suggesting a break in the seasonal monsoon activity. In general, maps shown in Fig. 2-2b exhibit lower k_{x1} values compared to other years, confirming once again the positive correlation between AEW's energetics and precipitation in West Africa.

In 1999, considered as the wet year (Fig. 2-3), the story is completely different. The first AEW occurs one month earlier than in the dry year and the bands on the Hovmöller diagram indicate a faster trajectory (crossing a long longitudinal band over a short period) and more intense (the red band is wider, which means a longer time, low slopes close to the horizontal). It is interesting to see the agreement between the wave detected in Hovmöller diagrams (Fig. 2-3a) and the snapshot chosen to highlight it in (fig. 2-3b). From August 1st to 9th, there is an important band from the western domain boundary until 10°W, which is highlighted by the system captured at 1 pm the 06/08/1999. Likewise, from August 24th to September 3rd, there is a large red band with a low slope from ~15°W until 30°E, which is highlighted at 7 am the 28/08/1999 by three consecutive maxima in the continent.

In 2006, considered as a near-normal year (Fig. 2-4), the overall pattern is closer to the wet year, with an exception in the shape of systems in the selected maps. At 7 am the 06/08/2006, there is a low-pressure system on the Atlantic, with a small horizontal extension compared to the wet year. This is also the case at 7 pm the 23/09/2006, with the storm's eye represented by the blue stain at the centre. At 7 am, the 12/09/2006 there is also a circular system leaving the West African coast to develop in the ocean, with the cyclone eye (representing the region of low winds at the center of the storm) represented by the blue stain.

After detecting the AEWs occurring in our simulations during three contrasting years, we will proceed to select a case study for the energetic study of an AEW using simulations of the CRCM6 and the regional transient-eddy budget equations. The selected wave must be intense, quite isolated and long-lived. The second step is to verify that the selected wave also exists in the reanalysis, in order to demonstrate the practical side of the study. The final step will consist in the analysis of time series of horizontal maps on different vertical levels, as well as vertical cross-sections of each term present in the energy budget.

2.2.2 Choice of the wave

Many authors have linked the origin of AEWs to the Eastern Africa. (Mekonnen *et al.*, 2006) indicated that convection triggered on the western side of the mountains over central and eastern Africa, near Darfur (western Sudan) and Ethiopia, plays a role in initiating AEWs to the west. (Berry et Thorncroft, 2005) showed the case of a strong AEW that seemed to be initiated by several mesoscale convective systems over the Darfur mountains. In this study, our first criterion for selecting an AEW will be the transient-eddy kinetic energy generated during its initiation phase in South Sudan, where Darfur mountains are located. We argue that the greatest is the energy generated during the initialization phase in the continent, the greatest is the chance to grow and develop towards the Atlantic.

To have an overview of the periods during which the waves are generated with an important kinetic energy, Fig. 2-5 shows the time evolution of the filtered winds k_{x1} , vertically and regionally averaged over southern Sudan. During the dry year (1997), the maximum energy generated during the whole season is three times smaller than during the wet year (1999).

According to this first criterion, two waves could be of interest: the one crossing the domain around the 28th of August 1999 and the other around the 5th of September 2006.

Another consideration for an efficient storm energy diagnostic, is the presence of only one system in the domain of interest, the West African Coast in our case. The wetter year (1999) exhibits 3 different peaks associated with 3 potential consecutive waves developing in the domain in a 7-day window. Hence in final analysis, we picked the wave that developed from September 5 to 10, 2006, a near-normal year. Many authors studied an AEW out of which hurricane Helene developed during the same period (Schwendike et Jones, 2010; Shen *et al.*, 2010).

2.2.3 Presence of the wave in the reanalysis dataset ERA5

To show the practical character of this study, we also made sure that the selected wave was also present in reanalyses. Fig. 2-6a shows the Hovmöller diagram of the k_{x1} during 2006 using ERA5. From the 5th to the 10th of September, the diagram shows an intense and long-lasting system, as in the model simulation. Fig. 2-6b shows the hourly time series of k_{x1} vertically integrated (1000-600 hPa) and horizontally averaged over the southern Sahara in 2006. The peak observed around the 5th of September is the same noted in Fig. 2-5 using CRCM6, but with a smaller amplitude. CRCM6 simulations have higher resolution and the advantage of providing physical terms not available in reanalysis dataset. That is why in the following sections, only CRCM6-simulated fields will be considered.

2.2.4 Transient-eddy energy cycle equations

For the study of the life cycle of an AEW, only the instantaneous energy reservoirs involving variables a_{x1} and k_{x1} need to be analysed. The components a_{x1} and k_{x1} are quadratic in temperature and wind perturbations, while the other components a_{x2} and k_{x2} are linear in temperature and wind perturbations.

In Chapter 1, the development of tendency equations of a_{x1} and k_{x1} are detailed as follows:

$$\frac{\partial a_{x1}}{\partial t} = (c_a + g_{x1}) - (f_{a_{x1}} + c_{x1a} + j_a) \quad (2.2)$$

where

$$\begin{aligned}
a_{x1} &= \frac{C_p}{T_r} \left(T'^2 - \langle T'^2 \rangle \right) \\
f_{a_{x1}} &= \vec{\nabla} \cdot \left\{ \vec{V} \left(\frac{C_p}{2T_r} T'^2 \right) - \left\langle \vec{V} \left(\frac{C_p}{2T_r} T'^2 \right) \right\rangle \right\} \\
c_a &= -\frac{C_p}{T_r} \left\{ \left(T' \vec{V}' \cdot \vec{\nabla} \right) \langle T \rangle - \left\langle \left(T' \vec{V}' \cdot \vec{\nabla} \right) \langle T \rangle \right\rangle \right\} \\
j_a &= -\frac{C_p}{T_r} T' \left\langle \left(\vec{V}' \cdot \vec{\nabla} \right) T' \right\rangle \\
c_{x1a} &= -\left\{ \omega' \alpha' - \langle \omega' \alpha' \rangle \right\} \\
g_{x1} &= \frac{1}{T_r} \left\{ T' Q' - \langle T' Q' \rangle \right\}
\end{aligned}$$

and

$$\begin{aligned}
\frac{\partial k_{x1}}{\partial t} &= \vec{V}_h' \cdot \frac{\partial \vec{V}_h'}{\partial t} - \left\langle \vec{V}_h' \cdot \frac{\partial \vec{V}_h'}{\partial t} \right\rangle \\
&= -\left(c_k + j_k - f_{k_{x1}} \right) + c_{x1k} - d_{x1}
\end{aligned} \tag{2.3}$$

where

$$\begin{aligned}
c_k &= -\left\{ \vec{V}_h' \cdot \left(\vec{V}' \cdot \vec{\nabla} \right) \cdot \left\langle \vec{V}_h' \right\rangle - \left\langle \vec{V}_h' \cdot \left(\vec{V}' \cdot \vec{\nabla} \right) \cdot \left\langle \vec{V}_h' \right\rangle \right\} \\
j_k &= -\vec{V}_h' \cdot \left\langle \left(\vec{V}' \cdot \vec{\nabla} \right) \cdot \vec{V}_h' \right\rangle \\
f_{k_{x1}} &= \vec{\nabla} \cdot \left\{ \vec{V} \left(\frac{1}{2} V_h'^2 \right) - \left\langle \vec{V} \left(\frac{1}{2} V_h'^2 \right) \right\rangle \right\} \\
c_{x1k} &= \left(\vec{V}_h' \cdot \vec{\nabla}_h \phi' - \left\langle \vec{V}_h' \cdot \vec{\nabla}_h \phi' \right\rangle \right) \\
d_{x1} &= -\left\{ \vec{V}_h' \cdot \vec{F}_h' - \left\langle \vec{V}_h' \cdot \vec{F}_h' \right\rangle \right\}
\end{aligned}$$

As noted in Chapter 1, the equations for a_{x1} (2.2) and k_{x1} (2.3) can be linked by making use of the continuity equation, hydrostatic equation and state law, to get:

$$f_{\phi x1} - c_{x1a} = c_{x1k}$$

where

$$f_{\phi x1} = \vec{\nabla} \cdot \left\{ \vec{V}' \phi' - \langle \vec{V}' \phi' \rangle \right\}$$

This set of transient-eddy energy equations is summarized in the diagram of Fig. 2-8. Boxes represent the time variation (tendency) of transient-eddy energy reservoirs (note that this differs from the case in Fig. 1-9 that indicated the time-mean energy). Arrows indicate conversions and sources/sinks of energy. Positive (negative) terms in Equations (2.3)-(2.4) are represented with inward (outward) arrows, but only the computation will inform us on their positive or negative contribution. At this stage, the direction of the arrows is arbitrary and only reflects the choice of sign used in writing the equations.

2.2.5 Wave energy budget computation and representation

It is important to note that the energy budget would not balance if meteorological variables were filtered before computing the terms present in Eqs. (2.2 and 2.3). On the other hand, the energetics of AEWs cannot be studied without filtering. The solution we have adopted in the following is to compute terms present in Eqs. (2.2 and 2.3) using original variables and apply the 3-5 days band-pass filter to the energy budget terms. As a result, the transient-eddy kinetic energy shown in previous sections will differ from the one in the following due to the application of the filter to the meteorological variables in the first case and to the energy terms from now on.

To study the energy budget of the selected wave, terms presented in Fig. 2-8 are time averaged from the 5th to the 10th of September and vertically integrated and horizontally averaged over the domain shown by the blue box on Fig. 2-7. As mentioned before, all the transient-eddy energies as defined vanish when averaged in time. According to Eqs. (2-2 and 2-3), the sum of positive and negative contributions to a reservoir (inward and outward arrows) must in theory be equal to the time tendency of the reservoir. However, in practice there is a residual (hopefully small) due to discretization errors.

The fact that each term describes a physical process allows us to understand how the energy is generated, converted and dissipated in a particular region as West Africa. The computation of the energy budget through the vertically integration, time and domain average of each term, is a powerful tool to evaluate their specific contributions.

Fig. 2-9a and b show respectively the vertically and domain averaged time series of the energy budget and standard deviations thereof. Thick lines represent terms present in the energy budget in Fig. 2-8, while dashed lines represent the residual obtained by computing the difference between the tendency terms and the sum of all energy fluxes acting on the energy reservoir. In the enthalpy energy budget, the conversion term c_{x1a} is almost balanced by the sum of the generation term g_{x1} and the other conversion term c_a . We see that c_{x1a} , c_a and g_{x1} are respectively the most prevailing terms, other terms having no quantitative impact on the net transient-eddy available enthalpy energy budget. On the other hand, almost all terms act meaningfully on the transient-eddy kinetic energy budget; only the third other term j_K seems negligible. The conversion of available enthalpy energy into kinetic energy c_{x1k} is on average more than twice as large as the other terms, and the tendency term $d(k_{x1})/dt$, the boundary flux term f_{Kx1} , the barotropic term c_k and the frictional dissipative term d_{x1} exhibit similar domain-averaged magnitude.

2.3 Results and analysis of the storm energy cycle terms

Three moments were chosen ($t_1=2006-09-06$, $t_2=2006-09-09$ and $t_3=2006-09-12$, all at 15h00 UTC) to highlight respectively, the generation, the growth and the wave's development over the Atlantic into tropical cyclone. In the following sections, we will analyse the evolution of energy reservoirs and fluxes through time. We recall that transient-eddy energy variables in this energy budget are filtered to focus the analysis on AEWs.

2.3.1 Energy reservoirs

k_{x1} is the kinetic energy of the quadratic time-varying component of the velocity field. With the passage of AEWs, wind fields change direction. Fig. 2-7a shows vertically integrated k_{x1} fields, superimposed on 700-hPa filtered winds. The wave originates in the neighbourhood of the

Southern Sudan at the exit of Ethiopian highlands, with a huge impact on the development of deep convective systems over West Africa. At t_1 , we see a dipole of positive and negative k_{x1} maximum values East and West of the northern Cameroon. This dipole is associated with the northern (southern) latitudinal shift of cool and humid (hot and dry) air in the Sahel characteristic of an AEW. Two days later, at t_2 , the positive maximum observed in the Tchad shifts westward to reach central Nigeria. We could estimate that the wave traveled almost 2000 km in 48 h, for an average speed of ~ 11.5 m/s. The slower an intense AEW move, the greater the risk of flooding due to long-lasting rains, given that they are strongly correlated with precipitation. At t_3 , the wave continues to travel a little bit faster with a great probability to reach the Atlantic and keep developing into an tropical depression. The fact that the wave speed increases, suggests an intensification of physical processes taking place during this phase. Fig. 2-10a shows the vertical longitude cross-section of k_{x1} , averaged between $5-15^{\circ}\text{N}$, which is the main latitudinal band containing AEWs. The average longitude of maxima and minima correspond to what we've seen in the vertically integrated maps, but here we can appreciate the vertical extend of the wave. At t_1 , the maximum energy in the troposphere is between 800 and 500 hPa, with a connection to another maximum around 200 hPa, where the Tropical Easterly Jet (TEJ) is observed. Many studies (ex (Nicholson, 2008)) have suggested a relationship between the TEJ and precipitation in the Sahel, but this remains unclear. The teleconnection between low and high troposphere indicates an unknown but existent role of the TEJ in the birth and development of AEWs. On the other hand, at this stage, the negative maximum is also located between 800 and 500 hPa, but exhibits no connection with upper levels. At t_2 , the wave shifts westward as described with the previous map. Both positive and negative maxima increase in magnitude and in longitudinal extent. This is also the case of the positive maximum in upper levels associated to the TEJ. There is a development of another minimum East of the positive maximum. It is obvious that this minimum develops in the previous 48 hours and is not coming from the East, due to the absence of teleconnection between low and high troposphere; as the minimum observed at t_1 is now (at t_2) connected with the TEJ. At t_3 , the wave keeps developing in longitudinal extent and magnitude. In the lower troposphere, previous maxima in minima confined between 500 and 800 hPa, extends now from the surface to 300 hPa. The new minimum is also connected to upper levels. This high vertical developing system suggests cumulonimbus clouds famous for their torrential rain.

a_{x1} is the available enthalpy energy of the quadratic time-varying component of the temperature field, with maximum values associated with either warm or cold anomalies. Fig. 2-7b shows vertically integrated a_{x1} fields, superimposed upon 850-hPa filtered temperature. (Thorncroft, Chris et Hodges, 2001) found a strong positive correlation between the frequency of 850-hPa wave activity at the West African coast based on 20 years of data. At t_1 , as it was the case for the kinetic energy, there is a dipole of positive and negative a_{x1} maximum values East and West of the northern Cameroon. These maxima are located slightly further north than k_{x1} maxima. According to filtered temperature arrows in the background, the positive maximum East of Northern Cameroon is associated with a drop in temperature due to northward shift of equatorial air, while the negative maximum West of Northern Cameroon is associated with a temperature increase due to southward incursion of Saharan air. At t_2 , the wave moves westward as described in the previous section. The most interesting feature at this stage is the northward shift in the position of maximum a_{x1} fields compared to k fields. We also note the presence of a negative maximum East the previous one, exactly at the same position as in than the kinetic energy. At t_3 , the a_{x1} maximum is associated with warm anomalies due to the incursion of continental and warmer Saharan air in the Atlantic. Fig. 2-10b shows the vertical longitude cross-section of a_{x1} . Maximum available enthalpy energy occurs in low levels in the shallow meridional overturning cell, as described in (Nicholson, 2009). At t_1 , maximum a_{x1} on the continent occurs exactly at the same position than k_{x1} . At t_2 and t_3 , maximum values shift westward exactly at the same position as k_{x1} . Finally, Transient-eddy available enthalpy maxima and minima have approximately the same positions and their intensity been proportional in our domain. This is confirmed by strong correlations between grid point time-series of a_{x1} and k_{x1} during the period of the storm (Annexe C in Supplementary material).

2.3.2 Conversion terms

The conversion of time-mean into transient-eddy available enthalpy (c_a) represents the instantaneous production of a_{x1} by the time-mean available enthalpy due to eddy heat fluxes along the time-mean temperature gradient. Fig. 2-12a shows vertically integrated c_a fields, superimposed upon 700-hPa filtered winds. At different moments, the pattern shows similarities with the representation of energy reservoirs; we see maximum positive (negative) conversions close to maximum positive (negative) energy reservoirs. This is not surprising because c_a is the

main contribution to the generation of a_{xI} , and c_{xIk} is the main contribution to the generation of k_{xI} ; in fact, c_{xIa} is closely related to c_a (see Appendix A1 for details). Another evidence is the strong correlation between k_{xI} and a_{xI} in West Africa, suggesting that the generation of available enthalpy will probably induces generation of kinetic energy. Finally, we understand that c_a fields during the passage of strong AEWs in the Sahel will probably exhibits similarities with a_{xI} , k_{xI} , c_{xIa} , and c_{xIk} patterns. Fig. 2-13a shows the vertical longitude cross-section of c_a . It is interesting to see the transition near the AEJ level. Positive (negative) conversions below the jet East of 15°W, in the continent, are sustained by negative (positive) conversions above. This suggests a cell of meridional overturning (Nicholson, 2009). At t_1 and t_2 , we see maximum conversion values exactly at the same position as maximum energy reservoirs with the corresponding signs. At these stages, there are no longitudinal lags between low- and high-level maximum in the continent. At t_3 , low-level maximum moves faster. This induces a longitudinal lag, highlighted by black dash lines added in the map, characteristic of baroclinic developments.

The term c_{xIa} represents the conversion of a_{xI} towards baroclinic production of k_{xI} . This field is quite similar to c_a , which should not be surprising given that it is proportional to c_a 's vertical component (see “Appendix B1” for details).

The term c_{xIk} represents the fraction of c_{xIa} convertible into k_{xI} . The fraction lost is represented by the boundary flux of geopotential height. Therefore, the subdomain of studies must be chosen in such a way that the system will develops inside its boundaries. It is also important to keep in mind that in a global energetic study, there is no boundary flux term and c_{xIa} will completely be convertible into k_{xI} .

The term c_k is the instantaneous conversion of time-mean into transient-eddy kinetic energy, commonly referred to as barotropic energy conversion. When c_k is positive, it is the barotropic growth, meaning that the mean state feeds the transient-eddy growth. Fig. 2-12d shows vertically integrated c_k fields, superimposed upon 700-hPa filtered winds. Among all conversion terms, c_k appears to be the weakest; this is why the values have been multiplied by three (3). In agreement with time series of vertically integrated, domain-averaged energy budget terms (Fig. 2-8), c_k growth is dominant during the first moments. Then, progressively, there is a baroclinic growth when the wave moves towards the coast. Figs 2-11b, shows grid points correlations map between

c_k and its components. The meridional component associated with the barotropy exhibits a strong correlation in the domain from the Sudan, where the waves are assumed to originate, to Ivory Coast (see dashed rectangle). This is coherent with positive values of c_k noted during the development of the wave. The vertical component associated with the baroclinicity exhibits also a strong correlation West of Ivory Coast when the system will reach the Atlantic and potentially develop into tropical cyclone. This result confirms that both baroclinic and barotropic energy conversions associated with the instability of the AEJ, contribute to the growth of AEWs (Albignat et Reed, 1980; Burpee, 1972). Fig. 2-13d shows the vertical longitude cross-section of c_k . Maximum conversions take place around 850 hPa, due to the AEJ instability, with the dominance of barotropic conversions on the continent during the first stage as mentioned above.

The third-order conversion terms j_k and j_a are most of the time rather small, although the j_k time-mean (shown in Fig. 2-8b,) seems to be non-negligible.

2.3.3 Generation, dissipation and boundary flux terms

g_{xI} is the diabatic generation of transient-eddy available enthalpy by the covariance of diabatic heating and temperature. Fig. 2-14a shows vertically integrated g_{xI} fields, superimposed upon 700-hPa filtered winds. The pattern is similar to energy reservoirs and conversion terms. This is not surprising according to time series of vertically integrated domain-averaged and standard deviations of the energy budget terms (Fig. 2-9). We can see g_{xI} standard deviation evolution following closely c_{xIa} and c_a with a lesser intensity. Fig. 2-15a shows the vertical longitude cross-section of g_{xI} . Maximum generation of available enthalpy takes place in the high troposphere. The high vertical extension confirms the presence of cumulonimbus. In the boundary layer, generation of available enthalpy takes place when humid air in the Gulf of Guinea is advected over the continent.

d_{xI} is the dissipation of transient-eddy kinetic energy by frictional forces. Fig. 2-14b shows its vertically integrated fields, superimposed upon 700-hPa filtered winds. Frictional dissipative forces tend to increase as the AEW winds intensify from t_1 to t_2 . At t_3 , d_{xI} maximum positive values follow the system while it is leaving the domain. Frictional forces counteract the storm's

energy growth. Fig. 2-15b shows the vertical longitude cross-section of d_{x1} . Frictional forces act near the surface in the atmospheric boundary layer.

Unlike the case in global energy cycle, boundary terms must be included in regional energy budget. They exist because on lateral boundaries of the regional model to ensure the continuity of equations. However, when the processes responsible for the growth and/or decay of the system occur within the limited domain, boundary terms could be neglected (Reed *et al.*, 1977). In this study, the transport of transient-eddy geopotential height $f_{\varphi x1}$ is an important term. In fact, the production of k_{x1} depends on it. Fig. 2-14d shows vertically integrated $f_{\varphi x1}$ fields, superimposed upon 700-hPa filtered winds. Negative values close to Chad and Sudan mean a contribution to the conversion of a_{x1} into k_{x1} , while high positive values mean an inhibition of AEW birth.

2.4 Summary and Conclusion

Based on a complete set of equations for the time-mean (K_M , K_E , A_M and A_E) and the time-variability (k_{x1} , k_{x2} , a_{x1} and a_{x2}) energy reservoirs, our main objective was to understand processes responsible of the growth and development of an intense African Easterly Wave. These summer disturbances develop in West Africa during the summer with a 3-5 days period, then only energy reservoirs of the time-mean will be pertinent. However, only a_{x1} and k_{x1} are quadratic in temperature and wind perturbations, while the other components a_{x2} and k_{x2} are linear in temperature and wind perturbations. That is why for study of the life cycle of an AEW, only the instantaneous energy reservoirs involving variables a_{x1} and k_{x1} need to be analysed.

Using the sixth-generation of the Canadian Regional Climate Model driven by ERA5 reanalysis, we performed simulations of three contrasting West African summers: dry (1997), humid (1999) and normal (2006). To detect all AEWs crossing the continent during these different summers, we used the Hovmöller diagram of the transient-eddy kinetic energy. This variable holds all the benefits of generally of both the meridional wind and the relative vorticity, which are commonly used in the literature to detect AEWs. This new method of detection allowed us to detect an excellent case study. The wave chosen is quite isolated, intense and long-lived AEW, which is ideal for limited area studies.

The computation of the energy budget of the selected wave is performed without applying the 3-5 days band pass filter on the variables, to avoid unbalancing the energy budget. Time variability are computed as the difference between the variable and its time-mean. The band-pass filter is applied to all the energy budget equations terms (2) and (3). The result is presented in Fig. 2-8b considered as the energy budget of our intense AEW. In this budget, the sum of all source term (inward arrows) minus the sum of all source terms (outward arrow) acting on an energy reservoir must be equal to the tendency of the reservoir in term of time-mean (value in black); standard deviations (red values) were given to indicate the variable variance. Variables are vertically-, time-, and domain-averaged. Results show that the diabatic generation of available enthalpy g_{xI} and the conversion of time mean into transient-eddy available enthalpy c_a are the main source of production of a_{xI} , which are dissipated mainly by c_{xIa} to allow the production of k_{xI} . This production is weakly influenced by the transport of transient-eddy geopotential height $f_{\varphi xI}$, and almost all the energy lost by the reservoir a_{xI} is converted into c_{xIk} , which is the main source of generation of k_{xI} . Finally, frictional dissipative, transport and conversion terms dissipate the kinetic energy to dampen the creation of AEW's.

Finally, the combination of the band-pass filtering and the transient eddy energy budget equations constitute a powerful tool to understand mechanisms responsible of the genesis and development of AEWs. Through the new variable k_{xI} , we detect AEWs crossing the West Africa in different configurations of West African Monsoon (dry, wet and moderate). We show that AEWs originate in South Sudan by generating both transient-eddy available enthalpy and kinetic energy. These energy reservoirs are strongly correlated in the Sahel from the Sudan until the West African coast in the trajectory of the wave. The low time-mean values of the geopotential height boundary flux term suggests that all energy dissipate by a_{xI} is converted into k_{xI} , and therefore explain the strong correlation between energy reservoirs. It emerges that the mechanism responsible of inhibiting AEWs is the transport of transient-eddy geopotential height $f_{\varphi xI}$. In our case, its negative time mean value contributes to improve the fraction of a_{xI} convertible into k_{xI} . In other cases, where $f_{\varphi xI}$ time-mean values are highly positive, the fraction of a_{xI} convertible into k_{xI} will be considerably reduced. We suggest a monitoring of $f_{\varphi xI}$ time-mean to evaluate the chance of AEW.

Acknowledgements: This research was funded by the Discovery Grant program of the Natural Sciences and Engineering Research Council of Canada (NSERC). Computations were made on the Calcul Québec-Compute Canada supercomputer, whose operation is funded by the Canada Foundation for Innovation (CFI), Québec’s Ministère de l’Économie et de l’Innovation and the Fonds de recherche du Québec-Nature et technologies (FRQ-NT). The authors are grateful for the ERA5 global reanalysis from ECMWF. The authors are deeply indebted to Katja Winger and François Roberge for their essential support in the use of the CRCM6/GEM5, as well as for downloading and preparing ERA5 reanalyses.

2.5 Appendix

2.5.1 Appendix A1: Link between c_a 's vertical component and c_{x1a}

The conversion of time-mean into transient-eddy available enthalpy (c_a) is written as follows:

$$c_a = -\frac{C_p}{T_r} \left\{ \begin{aligned} & \left(T' u' \left\langle \frac{\partial T}{\partial x} \right\rangle - \langle T' u' \rangle \left\langle \frac{\partial T}{\partial x} \right\rangle \right) + \\ & \left(T' v' \left\langle \frac{\partial T}{\partial y} \right\rangle - \langle T' v' \rangle \left\langle \frac{\partial T}{\partial y} \right\rangle \right) + \\ & \left(T' \omega' \left\langle \frac{\partial T}{\partial p} \right\rangle - \langle T' \omega' \rangle \left\langle \frac{\partial T}{\partial p} \right\rangle \right) \end{aligned} \right\} \quad (\text{B1.1})$$

While the conversion of a fraction of transient-eddy available enthalpy into kinetic energy is:

$$c_{x1a} = -(\omega' \alpha' - \langle \omega' \alpha' \rangle) \quad (\text{B1.2})$$

c_a 's vertical component can be rewritten as follows:

$$\begin{aligned} (c_a)_p &= -\frac{C_p}{T_r} \left\{ T' \omega' \left\langle \frac{\partial T}{\partial p} \right\rangle - \langle T' \omega' \rangle \left\langle \frac{\partial T}{\partial p} \right\rangle \right\} \\ &= -\frac{C_p}{T_r} \left\langle \frac{\partial T}{\partial p} \right\rangle \{ T' \omega' - \langle T' \omega' \rangle \} \\ &= -\frac{p C_p}{R T_r} \left\langle \frac{\partial T}{\partial p} \right\rangle \left\{ \frac{R}{p} T' \omega' - \left\langle \frac{R}{p} T' \omega' \right\rangle \right\} \\ &= -\left(\frac{p C_p}{R T_r} \left\langle \frac{\partial T}{\partial p} \right\rangle \right) * \{ -(\omega' \alpha' - \langle \omega' \alpha' \rangle) \} \end{aligned} \quad (\text{B1.3})$$

Finally,

$$(c_a)_p = \left(\frac{C_p}{\alpha_r} \left\langle \frac{\partial T}{\partial p} \right\rangle \right) c_{x1a} \quad (\text{B1.4})$$

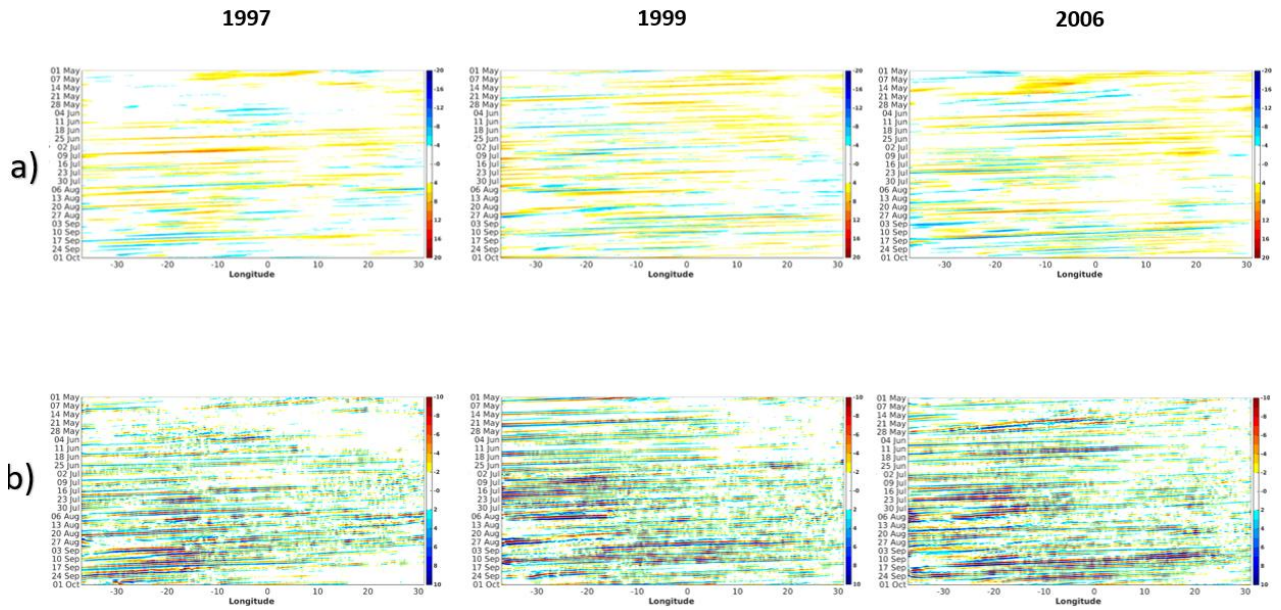


Figure 2-1: Hovmöller diagram of a) meridional wind (m.s^{-1}) and b) relative vorticity (10^6s^{-1}) at 700 hPa, for three contrasting years 1997-dry, 1999-humid and 2006-normal, from the CRCM6.

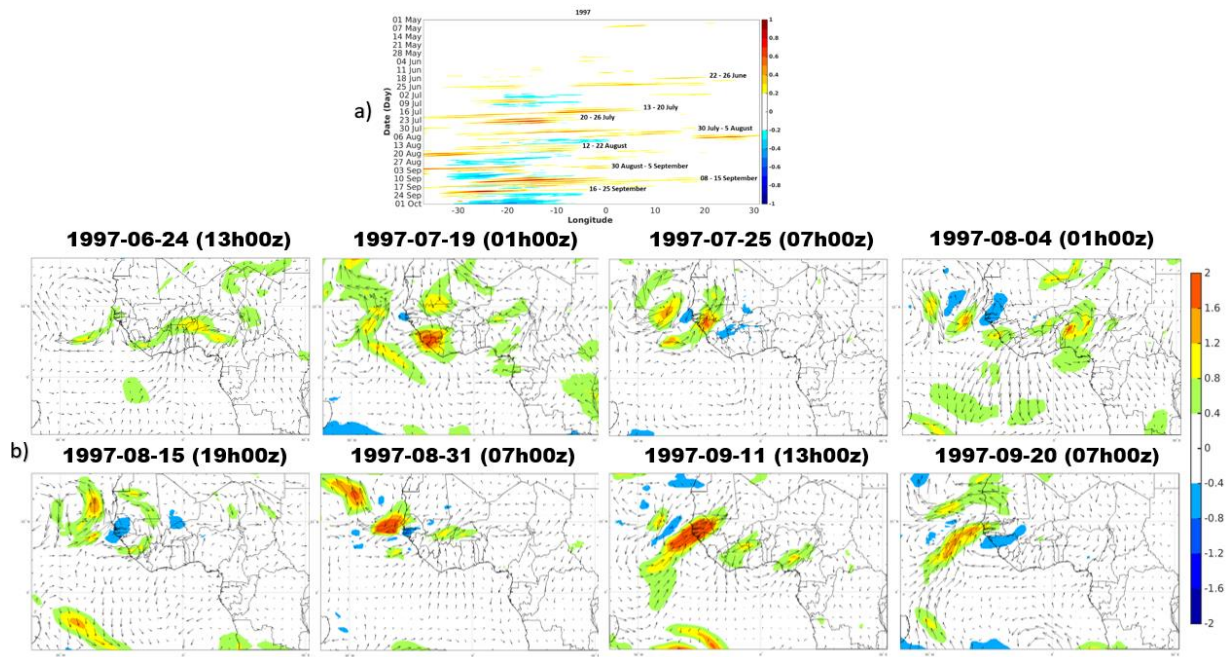


Figure 2-2: a) Hovmöller diagram of AX1 and b) vertically integrated (from 950 to 200 hPa) maps for a single date of the eight most important AEWs observed, in 10^4 J.m^2 , with superimposed 700 hPa filtered winds during the dry year (1997)

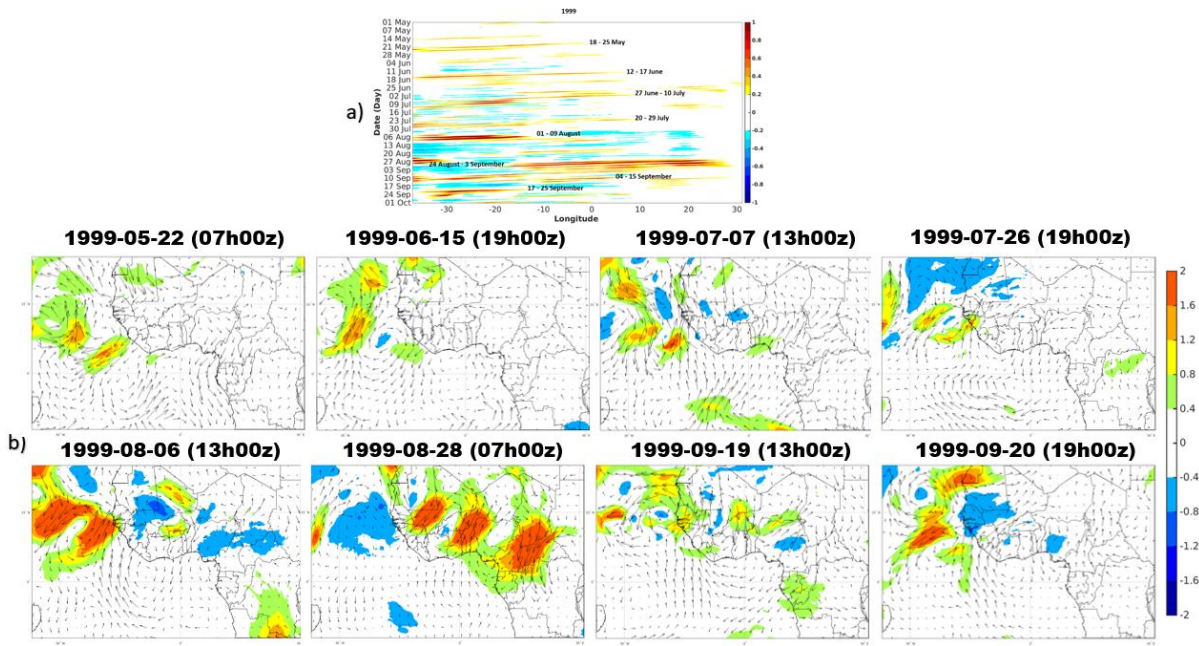


Figure 2-3: a) Hovmöller diagram of AX1 and b) vertically integrated (from 950 to 200 hPa) maps for a single date of the eight most important AEWs observed, in 10^4 J.m^2 , with superimposed 700 hPa filtered winds during the wet year (1999)

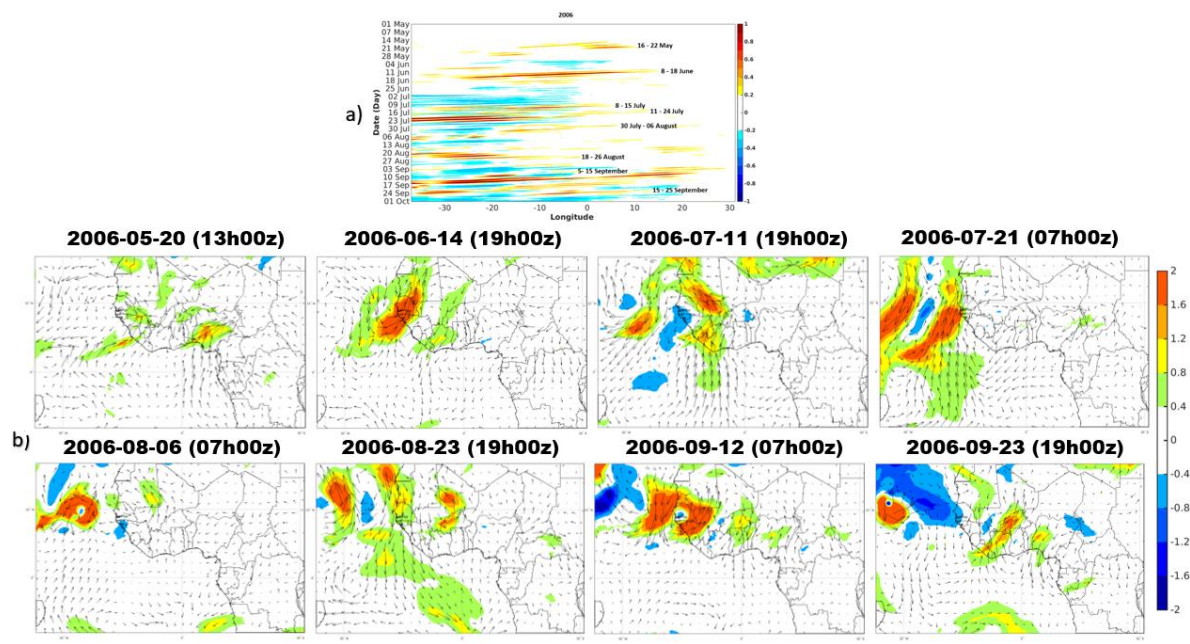


Figure 2-4: a) Hovmöller diagram of AX1 and b) vertically integrated (from 950 to 200 hPa) maps for a single date of the eight most important AEWs observed, in 10^4 J.m^2 , with superimposed 700 hPa filtered winds during the normal year (2006).

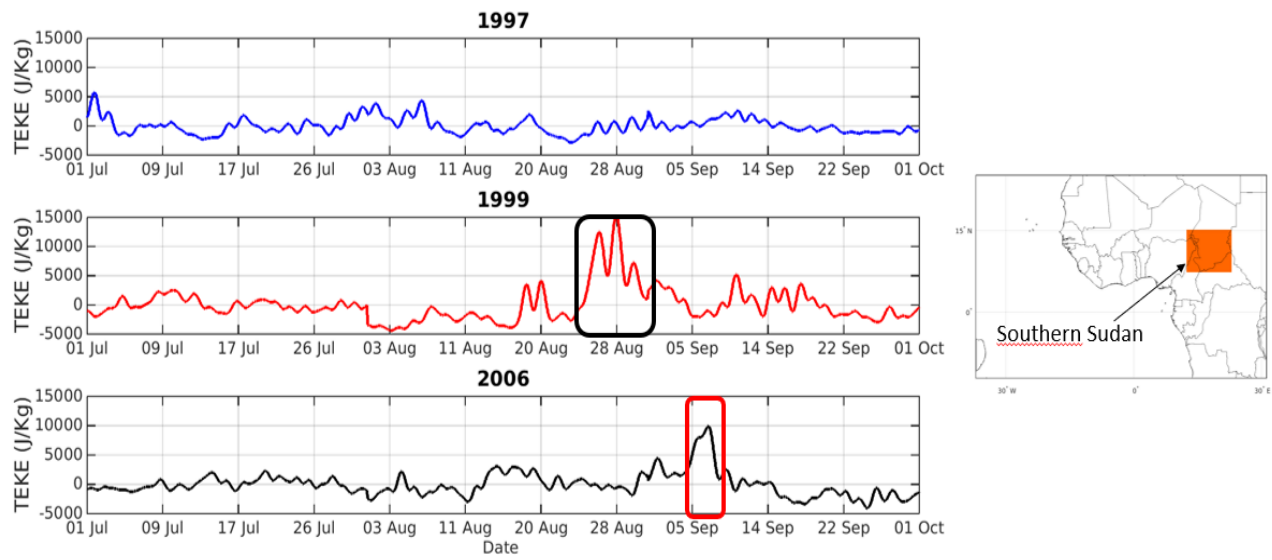


Figure 2-5: Transient eddy kinetic energy vertically (950-200 hPa) and horizontally (over south Sudan, represented to the right) averaged in $J.m^2$.

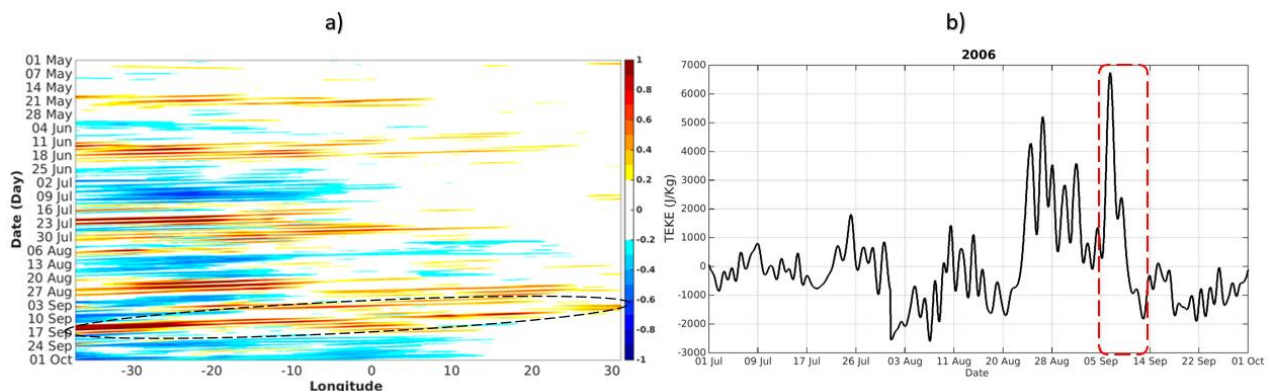


Figure 2-6: a) Hovmoller diagram of AX1 during the normal year (2006) in 10^4 J.m^2 and b) AX1 vertically integrated (from 950 to 200 hPa) and averaged over the southern Sudan in J.m^2 , using ERA5.

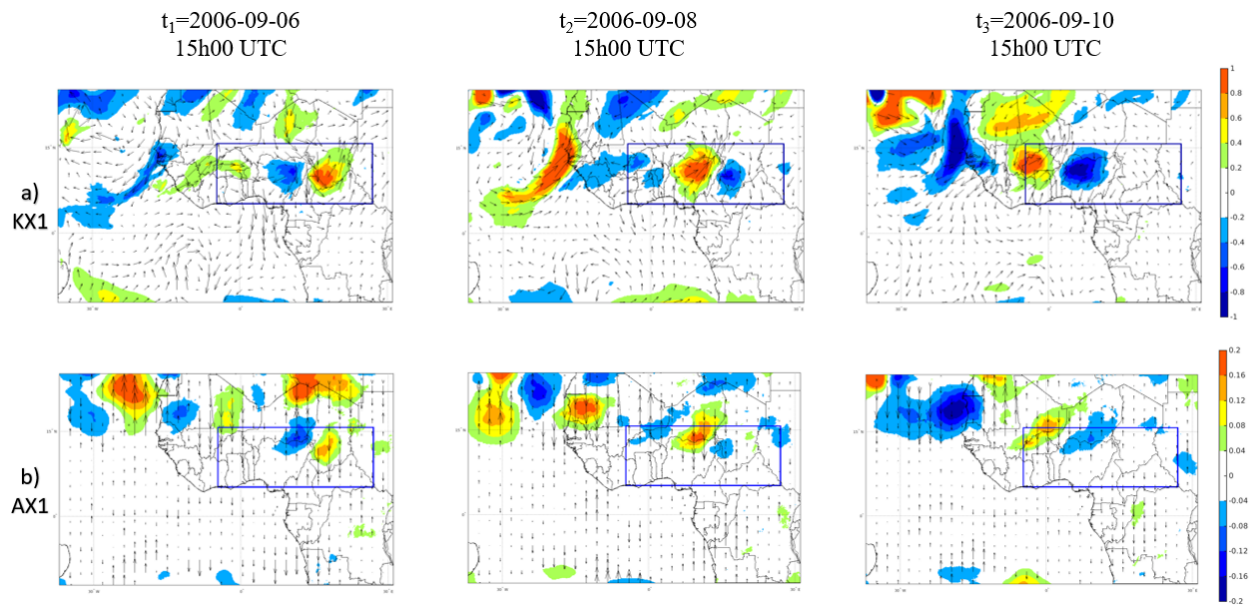


Figure 2-7: Maps of filtered vertically integrated instantaneous fields of three consecutive days of a) kx1 (with 700 hPa filtered winds as background, m.s^{-1}) and b) ax1 (with 850 hPa filtered temperature vertical arrows as background, $^{\circ}\text{K}$, in 10^5 J/m^2).

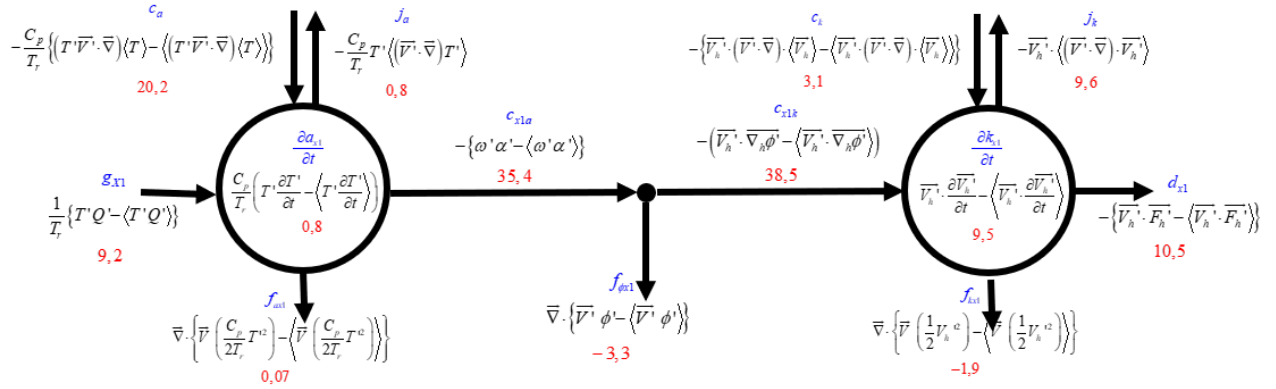


Figure 2-8: Vertically integrated (from 950 to 200 hPa) time- and domain-averaged storm energy cycle. Values are computed for the duration of the storm (September 05 to 10, 2006) and the units are in 10^{-3} W.m^{-2} .

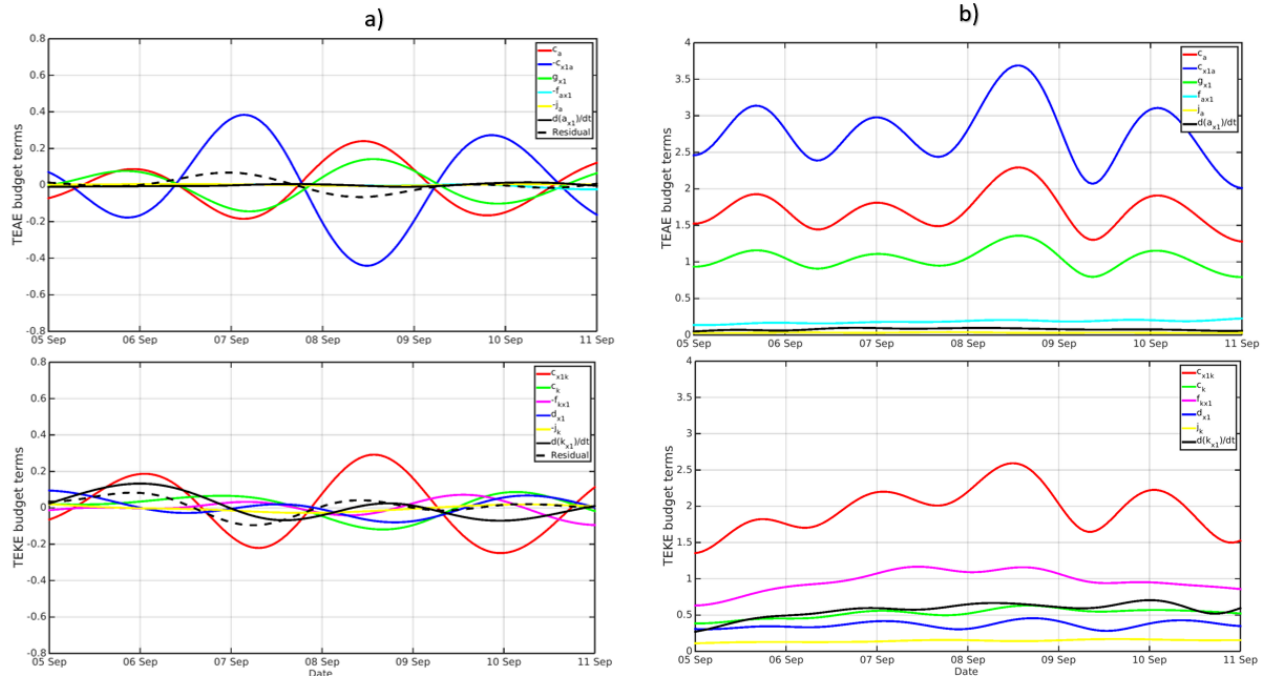


Figure 2-9: Time series of vertically integrated (from 950 to 200 hPa), a) domain-averaged and b) standard deviations terms of the energy budget in 10^4 W.m^{-2} .

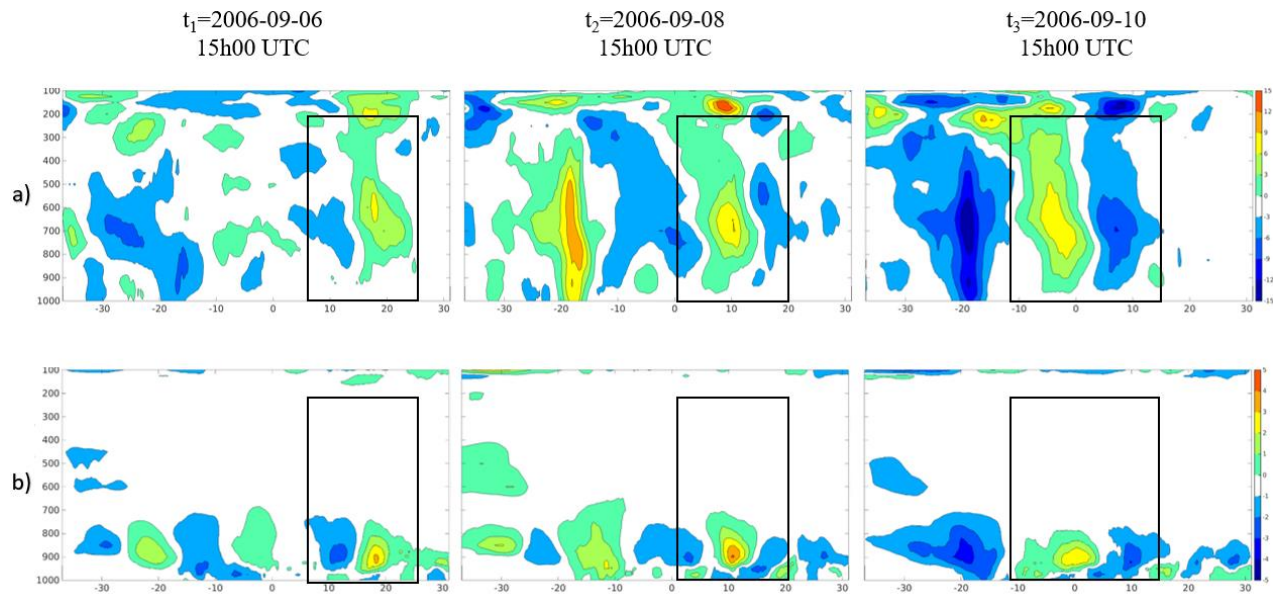


Figure 2-10 : Vertical longitude cross-section of instantaneous a) kx_1 and b) ax_1 , averaged in the latitude 5°N - 15°N . The abscissa is the longitude in degrees and the ordinate is the pressure in in hPa. Values are energy in $\text{J} \cdot \text{Kg}^{-1}$.

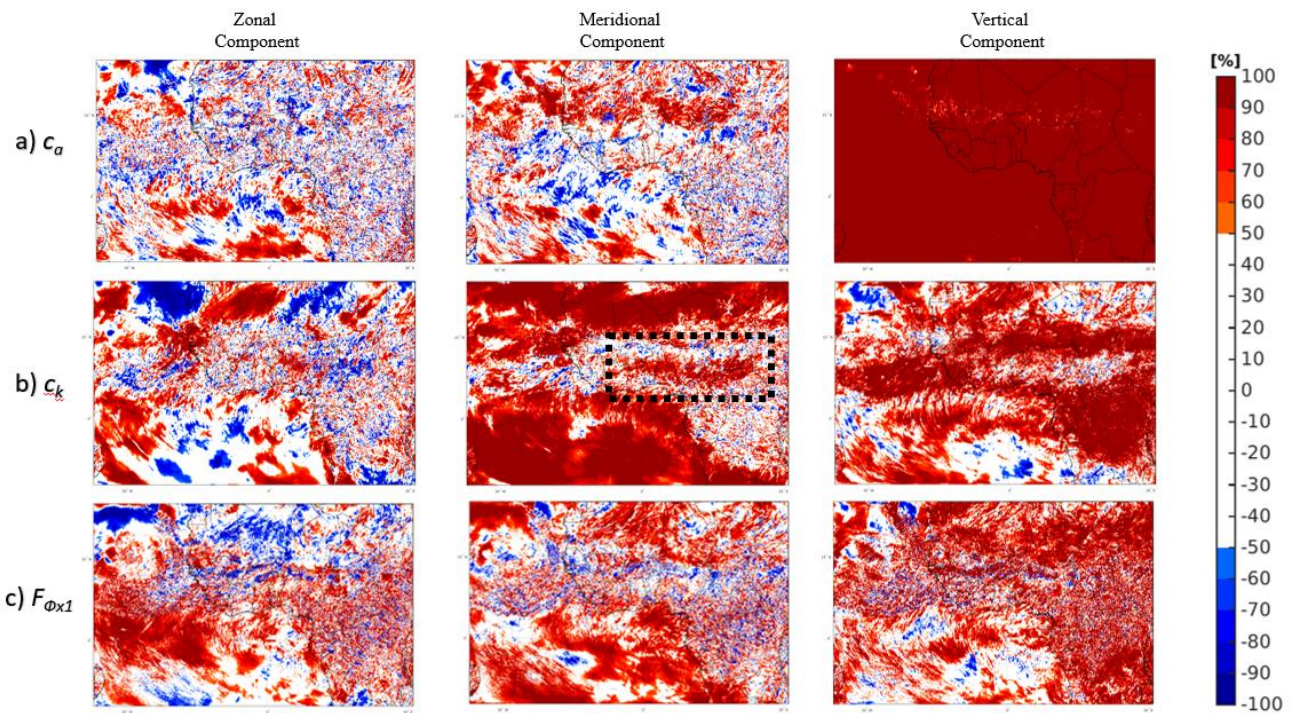


Figure 2-11: Maps of grid points time series correlation between different 3D components and the total a) c_a , b) c_k and c) $F_{\phi x1}$. Values are computed from September 05 to 15, 2006.

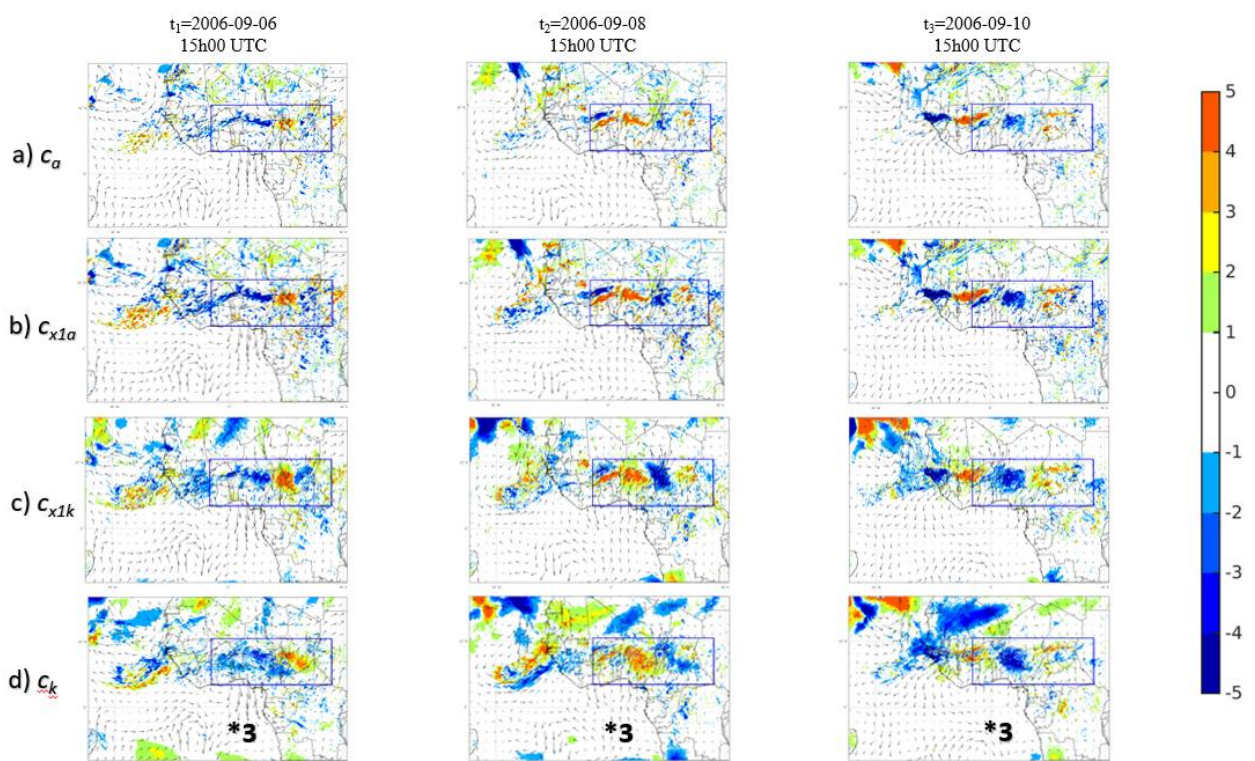


Figure 2-12: Maps of instantaneous vertically integrated (from 950 to 200 hPa) energy fluxes of a) c_a , b) c_{x1a} , c) c_{x1k} and d) c_k . Values are in W.Kg^{-1} with 700 hPa filtered horizontal wind (arrow, m.s^{-1}) as background.

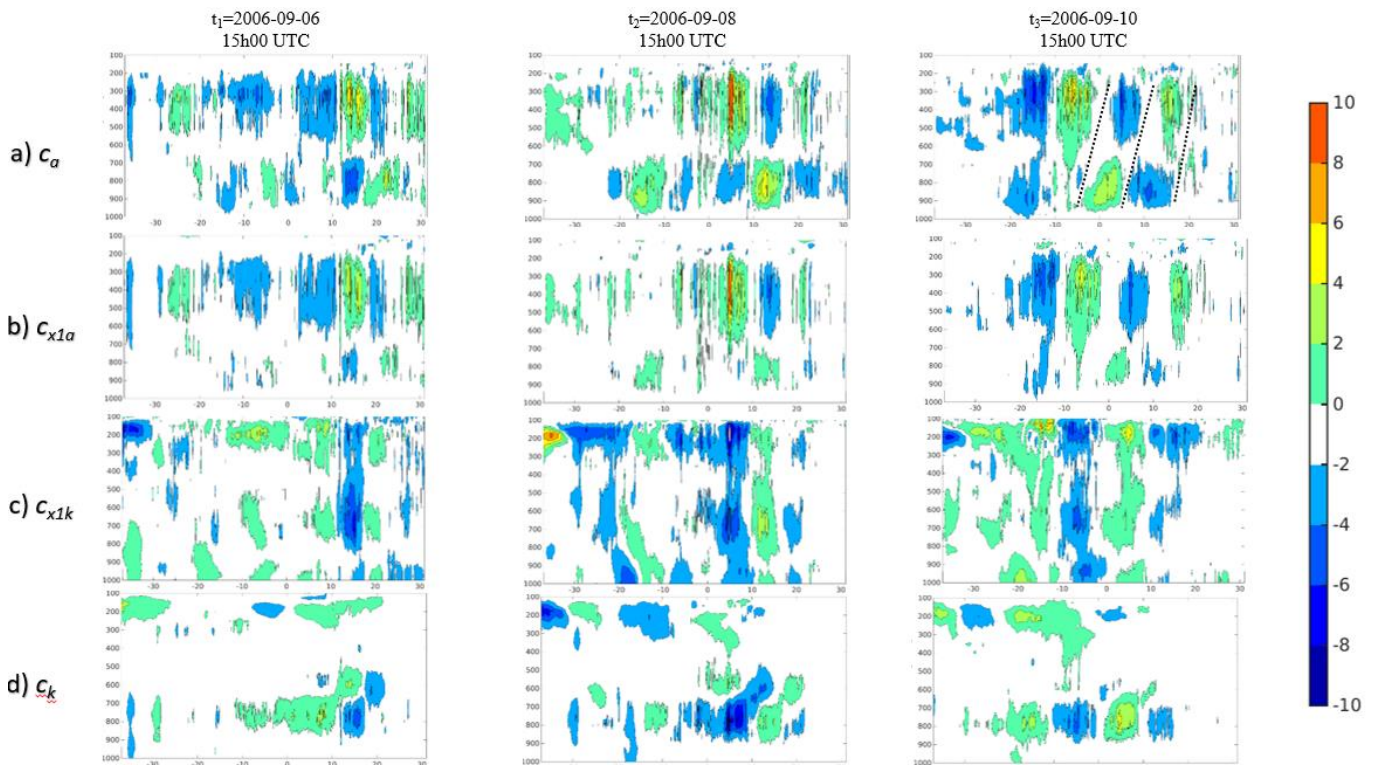


Figure 2-13: Vertical longitude cross-section of instantaneous a) c_a , b) c_{x1a} , c) c_{x1k} and d) c_k averaged in the latitude 5°N - 15°N . The abscissa is the longitude in degrees and the ordinate is the pressure in hPa. Values are energy in 10^4 W.Kg^{-1} .

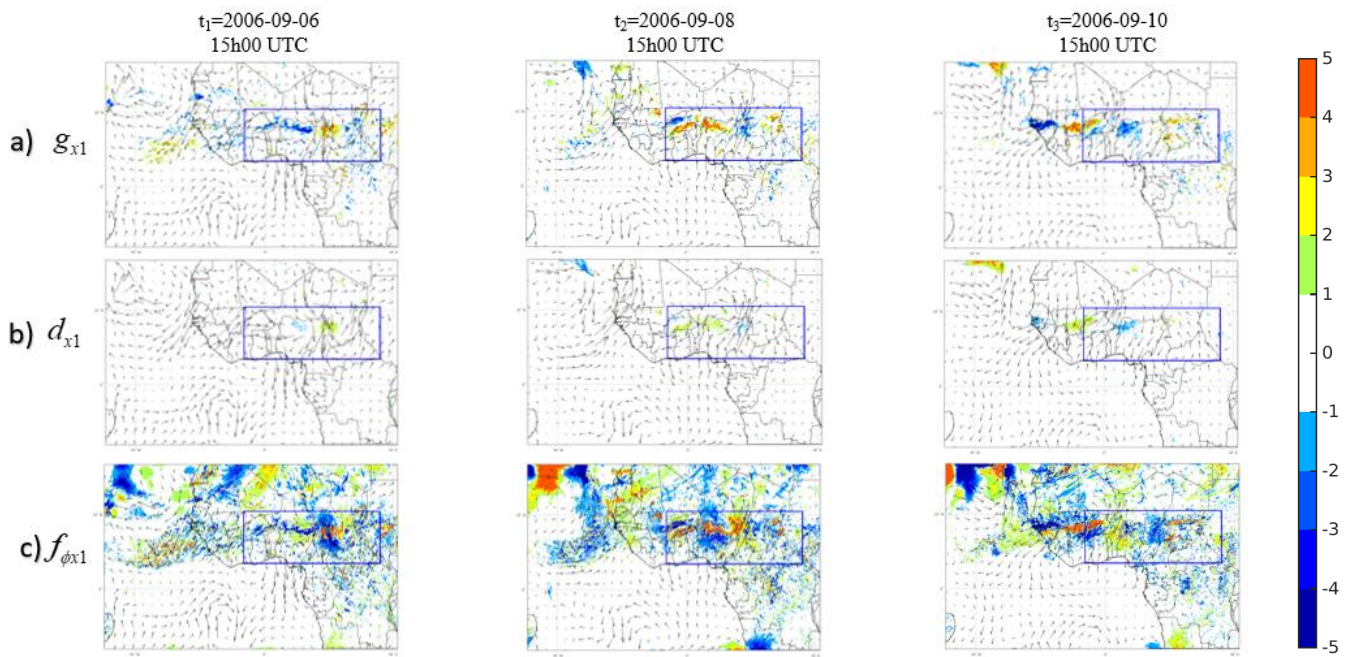


Figure 2-14: Maps of instantaneous vertically integrated (from 950 to 200 hPa) energy fluxes of a) g_{x1} , b) d_{x1} and c) $f_{\phi x1}$. Values are in W.m^{-2} with 700 hPa filtered horizontal wind (arrow, m.s^{-1}) as background.

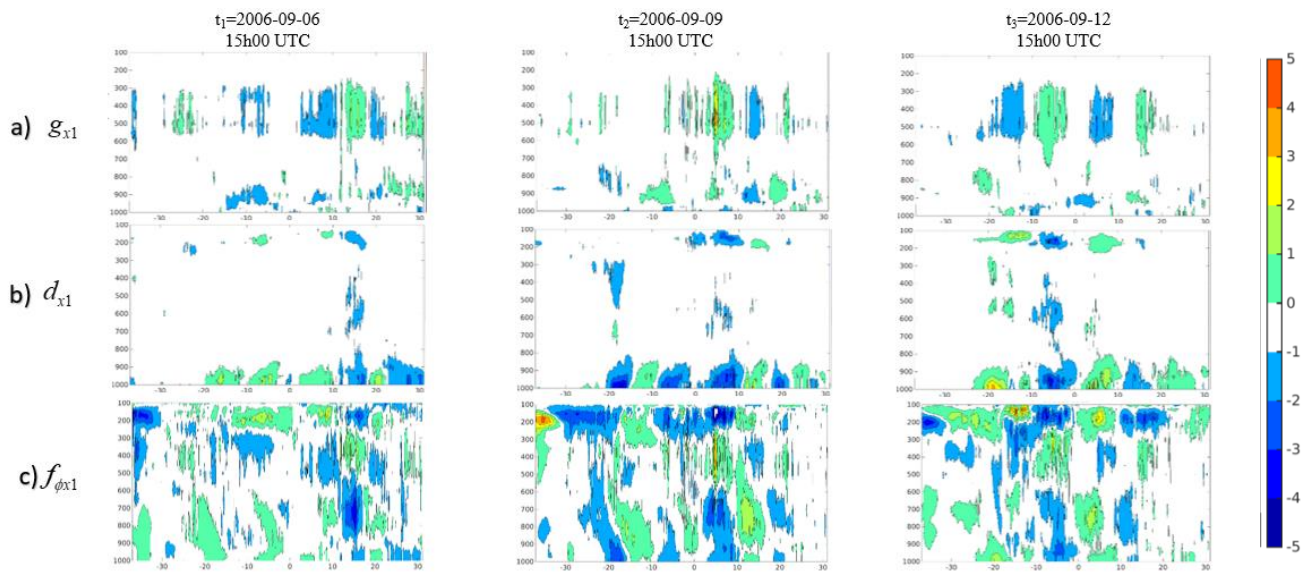


Figure 2-15: Vertical longitude cross-section of instantaneous a) g_{x1} , b) d_{x1} and c) $f_{\phi x1}$, averaged in the latitude 5°N-15°N. The abscissa is the longitude in degrees and the ordinate is the pressure in hPa. Values are in 10^4 W.Kg^{-1} .

CONCLUSION

1. Rappel de l'objectif et de l'approche empruntée

Les précipitations en Afrique de l'Ouest en général et au Sahel en particulier, constituent un enjeu majeur pour ces populations qui vivent majoritairement de l'agriculture pluviale (non irriguée). En effet, la disponibilité des ressources en eau, autant pour la consommation que pour l'agriculture, demeure un des principaux enjeux sociaux de cette partie du monde. À contrario, les événements météorologiques extrêmes avec des pluviométries importantes peuvent causer des inondations. Dès lors, les années autant anormalement sèches que pluvieuses doivent être identifiées à l'avance afin de permettre à ces populations de s'adapter. Cette prévision (sur quelques jours ou sur toute la saison comme dans cette étude) passe par l'identification des processus clés responsables de la variabilité des précipitations dans la région. L'objectif principal de cette thèse est d'étudier la Mousson de l'Afrique de l'Ouest à l'aide d'une approche énergétique régionale de l'atmosphère. Cette approche consiste à représenter les processus dynamiques de l'atmosphère par des termes physiques issus des lois de conservation de la masse, de l'énergie et de la quantité de mouvement. Dès lors, nous sommes en mesure de calculer au moyen d'un bilan d'énergie, toutes les contributions des différents processus au cours du temps et détecter ceux responsables de la variabilité à petite et grande échelle temporelle dans une région.

Dans le premier chapitre nous avons dans un premier temps établi les bilans d'énergie pour mettre un accent respectivement sur la variabilité intra saisonnière de la WAM et sur les événements de précipitations. Dans un deuxième temps, nous avons dans ce chapitre étudié le bilan d'énergie de trois saisons de mousson suivantes : une saison anormalement sèche (été 1997), une saison anormalement humide (été 1999) et une saison moyenne (été 2006) dans le but de comprendre les facteurs conduisant aux séquences sèches et humides.

Dans le dernier chapitre, nous avons appliqué le bilan d'énergie des tempêtes à un événement météorologique important associé à une onde d'Est intense. Nos critères de sélection nous ont permis de choisir une onde traversant le domaine entre le 5 et le 10 septembre 2006. De

nombreux auteurs ont également étudié une onde d'Est Africaine à partir de laquelle l'ouragan Hélène s'est développé sur la même période (Schwendike et Jones, 2010; Shen *et al.*, 2010).

2. Principaux résultats de la recherche empruntée

Dans le premier chapitre, il était premièrement question d'établir, au travers d'un bilan d'énergie régional, les contributions relatives des principaux processus physiques responsables de l'occurrence des séquences sèches et humides. L'établissement des bilans s'établit dans la continuité des travaux de (Marquet, 1991, 1994, 2003a) et (Nikiéma et Laprise, 2013) sur l'énergétique des domaines à aire limitée. Notre bilan présente l'avantage de mettre en évidence le principal terme responsable de la conversion d'enthalpie disponible en énergie cinétique, à travers l'introduction de nœuds. Ce terme avait déjà été mentionné par (Cook, 1999) comme le terme de circulation agéostrophique et par (Arnault et Roux, 2009) comme le travail des forces de pression à l'horizontale. L'introduction des nœuds nous permet aussi d'éliminer du bilan du réservoir d'énergie cinétique de moyenne temporelle K_M , des termes non physiquement significatifs (C_{MA} et $F_{\phi M}$), mais qui ont des valeurs très grandes à cause de la stratification verticale de l'atmosphère. Dès lors, l'intensité des processus physiques des trois autres réservoirs (A_E , K_M et K_E) est simplement proportionnelle à la valeur absolue des termes du bilan d'énergie calculés. D'autre part, si l'on extrapole notre domaine régional au domaine global, les termes de flux aux frontières latérales n'existeront plus (car le système terre-atmosphère sera considéré comme fermé) et on retrouve le bilan d'énergie du climat de (Lorenz, 1955) qui est la référence. Dans ce chapitre, nous avons aussi calculé le bilan d'énergie sur notre domaine durant trois saisons de moussons contrastées comme mentionné plus haut. Il en ressort que, si on ne regarde pas les termes importants qui sont associés à la stratification verticale de l'atmosphère, le terme de génération diabatique G_M est le plus important et sa valeur calculée à l'aide des simulations du MRCC6 lors de l'année moyenne 2006 peut être considérée comme une référence pour les années modérées. En effet, durant les années sèches (humides) cette valeur est moins (plus) importante. C'est encore plus flagrant pour ce qui est de la production des ondes d'Est africaines via le du réservoir K_E ; en regardant les valeurs absolues de tous les processus agissant sur K_E , ils sont plus petits l'année sèche, plus grands l'année humide et moyens l'année modérée. C'est par conséquent aussi le cas du réservoir K_E lui-même qui produit plus d'ondes l'année humide comme on peut le voir dans les résultats du chapitre 2. Sans l'introduction des nœuds, il aurait été

établi que le terme de conversion barocline C_{EA} qui agissait directement sur K_E est le principal terme de production des ondes, mais l'introduction des nœuds nous montre que ce terme est majoré par le flux aux frontières latérales des variations des hauteurs géopotentielles $F_{\phi E}$ pour obtenir C_{EK} . C'est ce dernier terme qui est la principale source de production des ondes d'Est Africaines. La seconde source de production est le terme de conversion barotrope issu de la conversion de l'énergie cinétique de moyenne temporelle en énergie cinétique des tempêtes. Les forces de friction qui agissent principalement en surface, constituent le seul puits d'énergie de K_E et permettent d'amortir la production des AEWs.

Dans le dernier chapitre, nous avons, à l'aide des équations du bilan du climat, étudié les mécanismes responsables de la croissance et du développement d'importantes ondes de l'Est durant la saison de mousson en Afrique de l'Ouest. Dans un premier temps, il était question de détecter dans nos trois simulations du chapitre précédent, toutes les ondes de l'Est qui ont traversé notre domaine. Dans la littérature, cette détection se faisait à l'aide du diagramme de Hovmöller du vent méridien ou du tourbillon relatif. Dans cette thèse, nous avons démontré que la variable K_{x1} , issue du bilan d'énergie des tempêtes, possédait les propriétés recherchées à la fois dans le vent méridien et le tourbillon relatif. Cette variable nous a permis de trouver une onde intense traversant le domaine l'année de pluviométrie modérée (2006) entre le 5 et le 10 septembre. Ce résultat confirme les travaux d'autres auteurs (Schwendike et Jones, 2010; Shen *et al.*, 2010) qui ont étudié une AEW sur la même période qui serait à l'origine de l'ouragan Hélène. Dès lors, nous avons pu calculer le bilan d'énergie de cette onde comme le montre la figure 2-8. Il en ressort que la réserve d'enthalpie disponible est dix fois inférieure à celle de l'énergie cinétique dans la région à cause de la faible fluctuation des températures près de l'équateur comparativement aux hautes latitudes. Cette réserve d'enthalpie est générée principalement par la conversion d'enthalpie disponible de moyenne temporelle en enthalpie disponible des tempêtes par le terme c_a et par le terme de génération diabatique g_{x1} . Comme ce fut le cas dans le bilan d'énergie du climat, la production principale des ondes par le terme de circulation agéostrophique c_{x1k} est issue de la combinaison de la dissipation de la réserve d'enthalpie disponible par les conversions baroclines c_{x1a} et du flux aux frontières latérales des variations des hauteurs du géopotentiel $f_{\phi x1}$. On remarque aussi en la forte corrélation entre l'enthalpie disponible et l'énergie cinétique sur la bande latitudinale comprise entre 10 et 15°N (voir Annexe C). Cette bande qui a un gradient méridien important de température (voir Fig. 0-3) est le trajet préférentiel

des AEWs. Ceci démontre une fois de plus la large prédominance sur le continent des processus baroclines par rapport aux processus barotropes pour le développement des AEWs.

En résumé, les résultats obtenus dans cette recherche ont démontré la pertinence des outils de l'énergétique de l'atmosphère pour l'étude des systèmes climatiques et météorologiques complexes. Ces outils nous permettent d'améliorer les connaissances actuelles de la mousson de l'Afrique de l'Afrique de l'Ouest et offre de nouvelles pistes d'identification et d'évaluation quant aux processus responsables de la variabilité des précipitations en Afrique de l'Ouest.

3. Limitations et nouvelles pistes de recherche

En réalisant ce projet de doctorat, nous avons démontré théoriquement que l'ensemble des équations des énergies mises ensemble nous ramenait à la formulation des équations de l'énergie cinétique et de l'enthalpie disponible originale. Ce qui signifie qu'aucune pièce d'information n'a été perdue et que nos bilans sont fiables. Cependant, pour appliquer ce bilan, il faut faire des choix qui peuvent être discutables. Premièrement, le choix du domaine d'étude. Le bilan d'énergie des systèmes régionaux a l'inconvénient d'avoir des contributions appelées termes de flux aux frontières dont les valeurs dépendent du choix du domaine. Dans ce projet, il a été mentionné que le terme de flux des variations des hauteurs de géopotentiel $F_{\phi E}$ ($f_{\phi xl}$) majore le terme conversion barocline pour donner le terme de circulation agéostrophique. Ceci est vrai pour le choix de notre domaine mais pourrait varier si un autre domaine était choisi. Cependant, nous avons choisi un domaine assez grand pour s'assurer que la majorité des processus dominant se déroulent à l'intérieur de celui-ci, permettant ainsi de limiter l'influence des conditions aux frontières. Dans un projet futur, il serait intéressant de faire le bilan du climat courant et de le comparer au climat futur dans une perspective de changement climatique. Cette étude permettrait de comparer l'intensité des processus physiques dans le climat courant à ceux du climat futur. Le résultat montrera clairement l'influence du scénario choisi sur l'atmosphère future.

La seconde difficulté est l'absence des termes physiques de friction et de chauffage diabatique dans les réanalyses atmosphériques pour valider les résultats issus du modèle. Le fait d'utiliser un seul modèle avec des variables de réanalyses qui ont été calculées de manière diagnostique est une limite pour notre recherche. À défaut de pouvoir obtenir une base de données des réanalyses pour ces termes, il faudrait au moins faire des simulations avec plusieurs autres modèles pour

confirmer définitivement nos résultats. Ainsi, il serait intéressant d'utiliser plusieurs modèles pour bénéficier des termes physiques qui sont difficilement mesurables afin de confirmer, par exemple, que le terme de chauffage diabatique de moyenne temporelle GM est beaucoup plus important les années humides que les années sèches, et qu'il en est de même du terme d'amortissement des ondes d'Est, D_E.

La troisième limitation est l'étude du bilan du climat sur des saisons au lieu de périodes d'au moins trente années. Seulement, bien que les données soient disponibles pour faire une étude sur une période complète, cette étude n'aurait pas répondu à une de nos principales questions de recherche à savoir la raison de la variabilité des précipitations depuis la fin des années 70. Ce choix qui pourrait sembler discutable nous a permis de voir l'origine des contrastes entre les années humides et les années sèches. Il en est de même du choix d'une tempête pour notre étude de cas. Pour appuyer fortement nos résultats, on pourrait refaire le même bilan sur plusieurs tempêtes. Cette difficulté aurait pu être résolue durant la thèse si le cadre théorique avait été rapidement mis en place. Malheureusement, la mise en place des équations du bilan et leur validation ont occupé un temps considérable dans la première partie de la thèse.

Pour finir, ma suggestion personnelle pour un projet futur serait de mettre en place un logiciel qui permettrait à tout utilisateur qui a des simulations ou des réanalyses avec tous les champs requis, de produire l'ensemble des résultats ici présentés. Ceci permettrait d'utiliser tout le temps que nous avons alloué à cette section à une analyse plus profonde des résultats pour une meilleure interprétation.

4. Retombées scientifiques

L'établissement d'un bilan d'énergie pourrait sembler être une tâche difficile et décourager certains de ce champ de recherche; pourtant le bilan d'énergie est une des seules approches quantitatives permettant d'évaluer les processus physiques dans le temps et l'espace.

Même si originellement le bilan d'énergie du climat a été conçu pour des périodes climatiques (d'au moins trente ans), il a été adapté dans cette étude aux saisons de Mousson d'Afrique de l'Ouest. Nous recommandons d'ailleurs le bilan d'énergie du climat pour l'étude des phénomènes qui durent au-delà de 30 jours pour deux principales raisons :

- La partie supérieure du bilan d'énergie du climat contenant les réservoirs A_M et K_M , donne un aperçu de l'état moyen de l'atmosphère, ce qui permet d'avoir une vision globale de l'état de l'atmosphère.
- En revanche la partie inférieure du bilan d'énergie du climat contenant les réservoirs A_E et K_E , permet d'analyser la variabilité à l'intérieur des périodes d'études (intra saisonnière, interannuelle, etc...). Les valeurs des termes ici sont relativement importantes (faibles) si d'importantes perturbations sont (ne sont pas) générées à l'intérieur des périodes d'études.

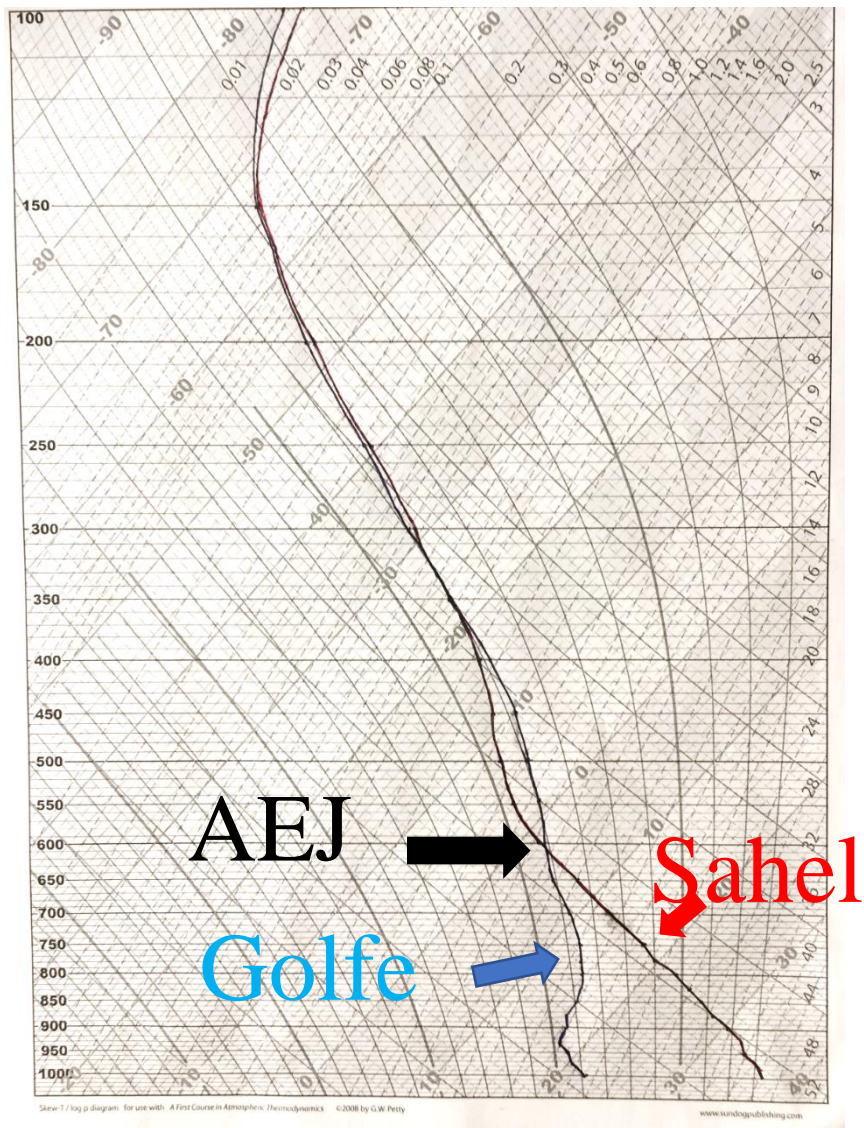
Pour l'étude des tempêtes, les termes du bilan d'énergie ne pas moyennés totalement, ce qui permet d'obtenir des baleurs du bilan d'énergie à chaque instant où les données de sortie sont disponibles. On peut donc suivre l'évolution temporelle des systèmes et de tous les processus qui y contribuent. Nous recommandons l'étude du bilan des tempêtes pour l'étude des :

- Perturbations transitoires à courte échelle temporelle à l'aide de la partie inférieure du bilan contenant les réservoirs k_{x1} et a_{x1} . En effet, dans cette partie, tous les termes ne sont quasiment composés que de produits de termes de déviation par rapport à la moyenne. Cette partie du bilan est idéale pour suivre la naissance, la croissance et l'extinction des perturbations atmosphériques.
- Perturbations transitoires à moyenne échelle temporelle à l'aide de la partie supérieure du bilan d'énergie des tempêtes contenant les réservoirs k_{x2} et a_{x2} . En effet, dans cette partie, tous les termes sont quasiment composés de produits entre les termes de moyenne temporelle et de déviations par rapport à celle-ci. Ce produit croisé est idéal pour étudier des cyclones / anticyclones semi-permanents. Ce sont des phénomènes mixtes qui influencent à la fois la climatologie et la météorologie.

Nous remarquons au terme de cette étude que, dépendamment de l'échelle temporelle associée au système que nous étudions, une approche énergétique de l'atmosphère différente peut être employée.

ANNEXE A

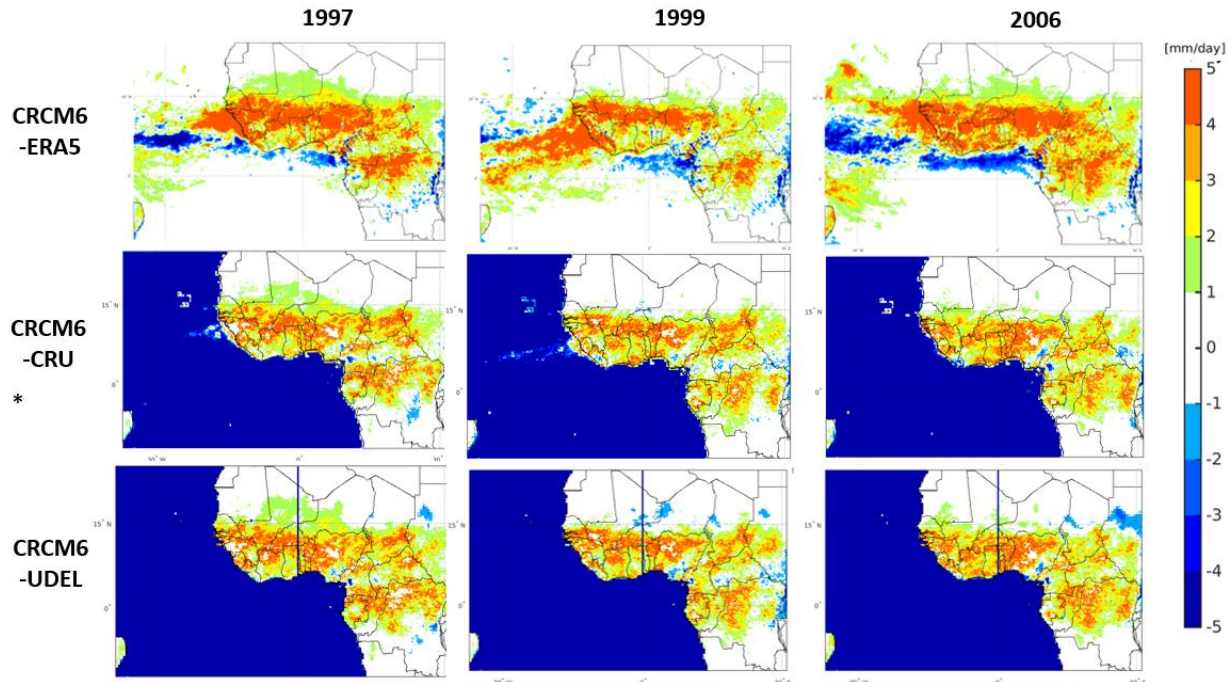
Résultats complémentaire de l'introduction



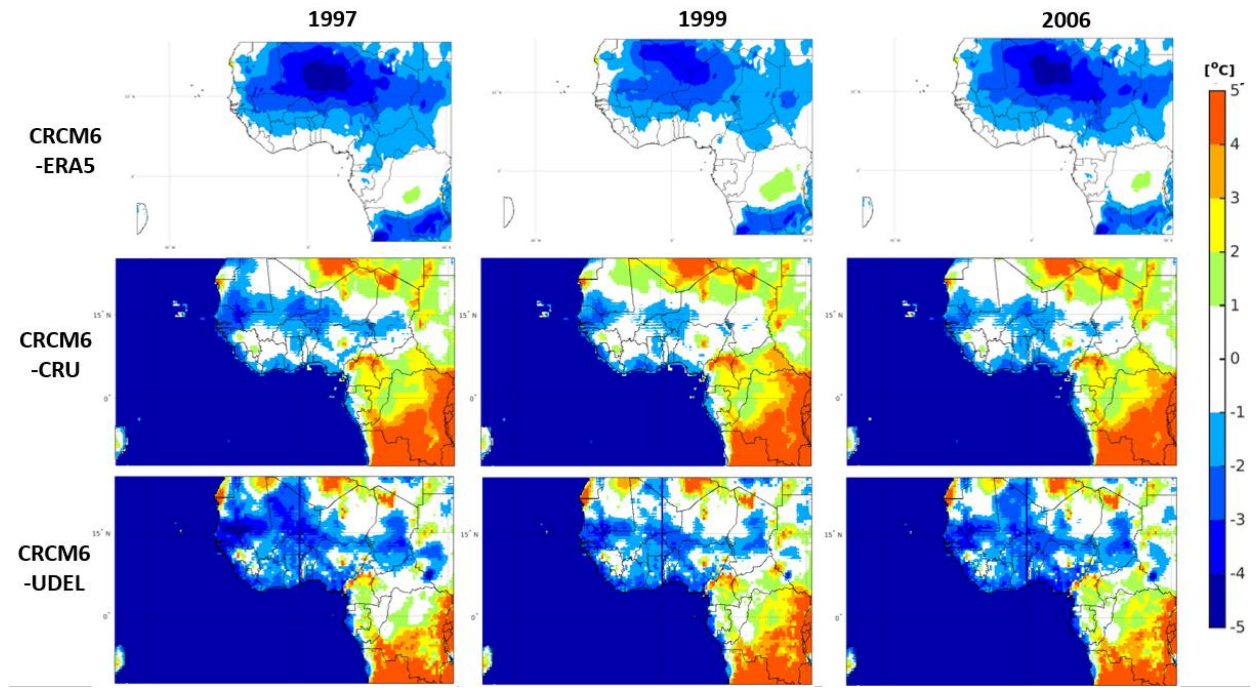
Annexe A 1: Téphigramme montrant les profils de température dans le golfe de Guinée (en bleu) et sur le Sahel (en rouge) des températures moyennées entre Juillet et septembre 2009.

ANNEXE B

Matériel supplémentaire du chapitre 1



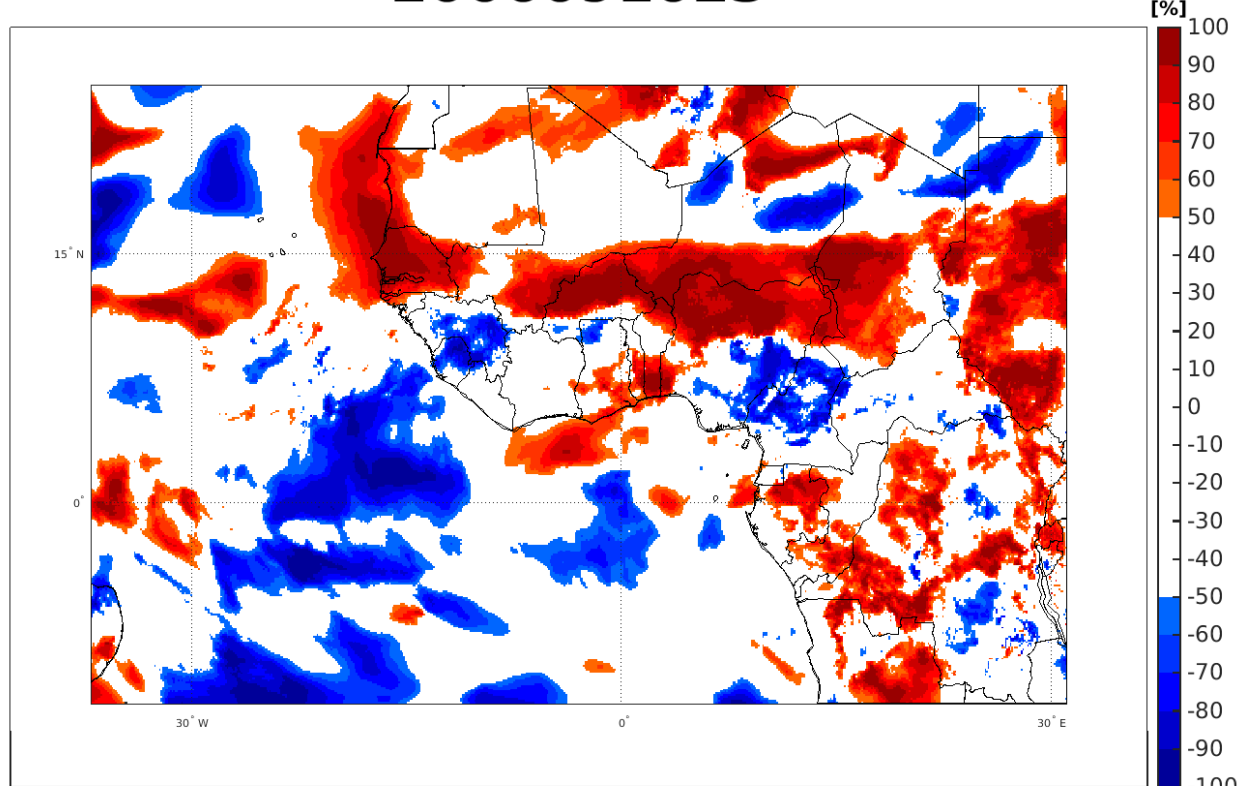
Annexe B 1: Precipitation bias between the CRCM6 and ERA5, CRU and UDEL in mm/day. Blue values in the Atlantic are due to lack of data in IN SITU datasets.



Annexe B 2: Temperature bias between the CRCM6 and ERA5, CRU and UDEL in Celsius. Blue values in the Atlantic are due to lack of data in IN SITU datasets.

ANNEXE C
Matériel supplémentaire du chapitre 2

2006091023



Annexe C 1: correlation between the time-series at each grid point between ax1 and kx1 from the 06th to the 11th of September 2006.

BIBLIOGRAPHIE

- Albignat, J. P. et Reed, R. J. (1980). The origin of African wave disturbances during Phase III of GATE. *Monthly Weather Review*, 108(11), 1827-1839.
- Arnault, J. et Roux, F. (2009). Case study of a developing African easterly wave during NAMMA: An energetic point of view. *Journal of the Atmospheric Sciences*, 66(10), 2991-3020.
- Avila, L. A. et Pasch, R. J. (1995). Atlantic tropical systems of 1993. *Monthly Weather Review*, 123(3), 887-896.
- Berry, G. J. et Thorncroft, C. (2005). Case study of an intense African easterly wave. *Monthly Weather Review*, 133(4), 752-766.
- Berry, G. J. et Thorncroft, C. D. (2012). African easterly wave dynamics in a mesoscale numerical model: The upscale role of convection. *Journal of the Atmospheric Sciences*, 69(4), 1267-1283.
- Boone, A., De Rosnay, P., Balsamo, G., Beljaars, A., Chopin, F., Decharme, B., Delire, C., Ducharme, A., Gascoin, S. et Grippo, M. (2009). The AMMA land surface model intercomparison project (ALMIP). *Bulletin of the American Meteorological Society*, 90(12), 1865-1880.
- Brammer, A. et Thorncroft, C. D. (2015). Variability and evolution of African easterly wave structures and their relationship with tropical cyclogenesis over the eastern Atlantic. *Monthly Weather Review*, 143(12), 4975-4995.
- Burpee, R. W. (1972). The origin and structure of easterly waves in the lower troposphere of North Africa. *Journal of the Atmospheric Sciences*, 29(1), 77-90.
- Carlson, T. N. (1969). Synoptic histories of three African disturbances that developed into Atlantic hurricanes. *Monthly Weather Review*, 97(3), 256-276.
- Clément, M., Nikiéma, O. et Laprise, R. (2017). Limited-area atmospheric energetics: illustration on a simulation of the CRCM5 over eastern North America for December 2004. *Climate Dynamics*, 48(9), 2797-2818.
- Cook, K. H. (1999). Generation of the African easterly jet and its role in determining West African precipitation. *Journal of Climate*, 12(5), 1165-1184.
- Cook, K. H. et Vizy, E. K. (2006). Coupled model simulations of the West African monsoon system: Twentieth-and twenty-first-century simulations. *Journal of Climate*, 19(15), 3681-3703.
- Cornforth, R. J., Hoskins, B. J. et Thorncroft, C. D. (2009). The impact of moist processes on the African easterly jet–African easterly wave system. *Quarterly Journal of the Royal Meteorological Society: A journal of the atmospheric sciences, applied meteorology and physical oceanography*, 135(641), 894-913.
- Diedhiou, A., Janicot, S., Viltard, A. et de Felice, P. (1998). Evidence of two regimes of easterly waves over West Africa and the tropical Atlantic. *Geophysical Research Letters*, 25(15), 2805-2808.
- Diedhiou, A., Janicot, S., Viltard, A., De Felice, P. et Laurent, H. (1999). Easterly wave regimes and associated convection over West Africa and tropical Atlantic: Results from the NCEP/NCAR and ECMWF reanalyses. *Climate Dynamics*, 15(11), 795-822.
- Evan, A. T., Flamant, C., Lavaysse, C., Kocha, C. et Saci, A. (2015). Water vapor-forced greenhouse warming over the Sahara Desert and the recent recovery from the Sahelian drought. *Journal of Climate*, 28(1), 108-123.
- Fink, A. H. (2012). To the 75th anniversary of the discovery of African Easterly Waves. 30th Conference on Hurricanes and Tropical Meteorology,
- Gowing, J. W. (2003). Food security for sub-Saharan Africa: does water scarcity limit the options? *Land Use and Water Resources Research*, 3(1732-2016-140279).

- Hall, N. M., Kiladis, G. N. et Thorncroft, C. D. (2006). Three-dimensional structure and dynamics of African easterly waves. Part II: Dynamical modes. *Journal of the Atmospheric Sciences*, 63(9), 2231-2245.
- Hernández-Díaz, L., Laprise, R., Nikiéma, O. et Winger, K. (2017). 3-Step dynamical downscaling with empirical correction of sea-surface conditions: application to a CORDEX Africa simulation. *Climate Dynamics*, 48(7), 2215-2233.
- Hernández-Díaz, L., Laprise, R., Sushama, L., Martynov, A., Winger, K. et Dugas, B. (2013). Climate simulation over CORDEX Africa domain using the fifth-generation Canadian Regional Climate Model (CRCM5). *Climate Dynamics*, 40(5), 1415-1433.
- Hersbach, H., Bell, B., Berrisford, P., Hirahara, S., Horányi, A., Muñoz - Sabater, J., Nicolas, J., Peubey, C., Radu, R. et Schepers, D. (2020). The ERA5 global reanalysis. *Quarterly Journal of the Royal Meteorological Society*, 146(730), 1999-2049.
- Hourdin, F., Musat, I., Guichard, F. s., Ruti, P. M., Favot, F., Filiberti, M.-A., Pham, M., Grandpeix, J.-Y., Polcher, J. et Marquet, P. (2010). AMMA-model intercomparison project. *Bulletin of the American Meteorological Society*, 91(1), 95-104.
- Hsieh, J.-S. et Cook, K. H. (2007). A study of the energetics of African easterly waves using a regional climate model. *Journal of the Atmospheric Sciences*, 64(2), 421-440.
- Kiladis, G. N., Thorncroft, C. D. et Hall, N. M. (2006). Three-dimensional structure and dynamics of African easterly waves. Part I: Observations. *Journal of Atmospheric Sciences*, 63(9), 2212-2230.
- Knippertz, P. et Fink, A. H. (2008). Dry-season precipitation in tropical West Africa and its relation to forcing from the extratropics. *Monthly Weather Review*, 136(9), 3579-3596.
- Kuo, T.-H. B. (1998). *On the scale interaction between African easterly waves and convection* [Massachusetts Institute of Technology].
- Lafore, J. P., Flamant, C., Guichard, F., Parker, D., Bouniol, D., Fink, A., Giraud, V., Gosset, M., Hall, N. et Höller, H. (2011). Progress in understanding of weather systems in West Africa. *Atmospheric Science Letters*, 12(1), 7-12.
- Laprise, R. (1992). The Euler equations of motion with hydrostatic pressure as an independent variable. *Monthly Weather Review*, 120(1), 197-207.
- Laux, P., Kunstmann, H. et Bárdossy, A. (2008). Predicting the regional onset of the rainy season in West Africa. *International Journal of Climatology: A Journal of the Royal Meteorological Society*, 28(3), 329-342.
- Lavaysse, C., Flamant, C., Evan, A., Janicot, S. et Gaetani, M. (2016). Recent climatological trend of the Saharan heat low and its impact on the West African climate. *Climate Dynamics*, 47(11), 3479-3498.
- Lavaysse, C., Flamant, C., Janicot, S. et Knippertz, P. (2010). Links between African easterly waves, midlatitude circulation and intraseasonal pulsations of the West African heat low. *Quarterly Journal of the Royal Meteorological Society*, 136(S1), 141-158.
- Lavaysse, C., Flamant, C., Janicot, S., Parker, D. J., Lafore, J.-P., Sultan, B. et Pelon, J. (2009). Seasonal evolution of the West African heat low: a climatological perspective. *Climate Dynamics*, 33(2), 313-330.
- Lawrence, M. B., Avila, L. A., Beven, J. L., Franklin, J. L., Guiney, J. L. et Pasch, R. J. (2001). Atlantic hurricane season of 1999. *Monthly Weather Review*, 129(12), 3057-3084.
- Lebel, T., Parker, D. J., Flamant, C., Bourlès, B., Marticorena, B., Mougin, E., Peugeot, C., Diedhiou, A., Haywood, J. et Ngamini, J.-B. (2010). The AMMA field campaigns: Multiscale and multidisciplinary observations in the West African region. *Quarterly Journal of the Royal Meteorological Society*, 136(S1), 8-33.
- Lemburg, A., Bader, J. et Claussen, M. (2019). Sahel rainfall-tropical easterly jet relationship on synoptic to intraseasonal time scales. *Monthly Weather Review*, 147(5), 1733-1752.

- Li, L., Ingersoll, A. P., Jiang, X., Feldman, D. et Yung, Y. L. (2007). Lorenz energy cycle of the global atmosphere based on reanalysis datasets. *Geophysical Research Letters*, 34(16).
- Lin, Y.-L., Liu, L., Tang, G., Spinks, J. et Jones, W. (2013). Origin of the pre-tropical storm Debby (2006) African easterly wave-mesoscale convective system. *Meteorology and Atmospheric Physics*, 120(3), 123-144.
- Lorenz, E. N. (1955). Available potential energy and the maintenance of the general circulation. *Tellus*, 7(2), 157-167.
- Lorenz, E. N. (1957). *Static stability and atmospheric energy*. Massachusetts Institute of Technology, Department of Meteorology.
- Margules, M. (1903). Über die Energie der Stürme. *Jahrb. kk Zent. Anst. für Meteorol. und Erdmagnet*, 48, 1-26.
- Marquet, P. (1990). La notion d'enthalpie utilisable: application à l'énergétique atmosphérique. *Comptes rendus de l'Académie des sciences. Série IIb, Mécanique, physique, astronomie*, 310, 1387-1392.
- Marquet, P. (1991). On the concept of exergy and available enthalpy: Application to atmospheric energetics. *Quarterly Journal of the Royal Meteorological Society*, 117(499), 449-475.
- Marquet, P. (1994). *Applications du concept d'Exergie à l'énergétique de l'atmosphère. Les notions d'enthalpies utilisables sèche et humide* Université Paul Sabatier-Toulouse III].
- Marquet, P. (2003a). The available - enthalpy cycle. I: Introduction and basic equations. *Quarterly Journal of the Royal Meteorological Society: A journal of the atmospheric sciences, applied meteorology and physical oceanography*, 129(593), 2445-2466.
- Marquet, P. (2003b). The available - enthalpy cycle. II: Applications to idealized baroclinic waves. *Quarterly Journal of the Royal Meteorological Society: A journal of the atmospheric sciences, applied meteorology and physical oceanography*, 129(593), 2467-2494.
- Mass, C. (1979). A linear primitive equation model of African wave disturbances. *Journal of Atmospheric Sciences*, 36(11), 2075-2092.
- McTaggart - Cowan, R., Vaillancourt, P., Zadra, A., Chamberland, S., Charron, M., Corvec, S., Milbrandt, J., Paquin - Ricard, D., Patoine, A. et Roch, M. (2019). Modernization of atmospheric physics parameterization in Canadian NWP. *Journal of Advances in Modeling Earth Systems*, 11(11), 3593-3635.
- Mekonnen, A., Thorncroft, C. D. et Aiyyer, A. R. (2006). Analysis of convection and its association with African easterly waves. *Journal of Climate*, 19(20), 5405-5421.
- Milbrandt, J. et Morrison, H. (2016). Parameterization of cloud microphysics based on the prediction of bulk ice particle properties. Part III: Introduction of multiple free categories. *Journal of the Atmospheric Sciences*, 73(3), 975-995.
- Mishra, S. et Tandon, M. (1983). A combined barotropic-baroclinic instability study of the upper tropospheric tropical easterly jet. *Journal of Atmospheric Sciences*, 40(11), 2708-2723.
- Mohr, K. I., Famiglietti, J. S. et Zipser, E. J. (1999). The Contribution to Tropical Rainfall with respect to Convective System Type, Size, and Intensity.
- Nicholson, S. E. (2008). The intensity, location and structure of the tropical rainbelt over west Africa as factors in interannual variability. *International Journal of Climatology: A Journal of the Royal Meteorological Society*, 28(13), 1775-1785.
- Nicholson, S. E. (2009). A revised picture of the structure of the "monsoon" and land ITCZ over West Africa. *Climate Dynamics*, 32(7), 1155-1171.
- Nicholson, S. E. et Klotter, D. (2021). The Tropical Easterly Jet over Africa, its representation in six reanalysis products, and its association with Sahel rainfall. *International Journal of Climatology*, 41(1), 328-347.
- Nikiéma, O. et Laprise, R. (2013). An approximate energy cycle for inter-member variability in ensemble simulations of a regional climate model. *Climate Dynamics*, 41(3), 831-852.

- Nikiéma, O., Laprise, R. et Dugas, B. (2018). Energetics of transient-eddy and inter-member variabilities in global and regional climate model simulations. *Climate Dynamics*, 51(1), 249-268.
- Olanian, E., Afiesimama, E., Oni, F. et Lawal, K. A. (2015). Simulating the daily evolution of West African monsoon using high resolution regional COSMO-model: A case study of the first half of 2015 over Nigeria. *Journal of Climatology & Weather Forecasting*, 1-8.
- Oort, A. H. (1964). On estimates of the atmospheric energy cycle. *Monthly Weather Review*, 92(11), 483-493.
- Pan, Y., Li, L., Jiang, X., Li, G., Zhang, W., Wang, X. et Ingersoll, A. P. (2017). Earth's changing global atmospheric energy cycle in response to climate change. *Nature communications*, 8(1), 1-8.
- Paradis, D., Lafore, J., Redelsperger, J. et Balaji, V. (1995). African easterly waves and convection. Part I: Linear simulations. *Journal of Atmospheric Sciences*, 52(10), 1657-1679.
- Parker, D., Burton, R., Diongue - Niang, A., Ellis, R., Felton, M., Taylor, C., Thorncroft, C., Bessemoulin, P. et Tompkins, A. (2005). The diurnal cycle of the West African monsoon circulation. *Quarterly Journal of the Royal Meteorological Society: A journal of the atmospheric sciences, applied meteorology and physical oceanography*, 131(611), 2839-2860.
- Parker, D. J., Thorncroft, C. D., Burton, R. R. et Diongue - Niang, A. (2005). Analysis of the African easterly jet, using aircraft observations from the JET2000 experiment. *Quarterly Journal of the Royal Meteorological Society: A journal of the atmospheric sciences, applied meteorology and physical oceanography*, 131(608), 1461-1482.
- Patricola, C. M., Saravanan, R. et Chang, P. (2018). The response of Atlantic tropical cyclones to suppression of African easterly waves. *Geophysical Research Letters*, 45(1), 471-479.
- Pearce, R. (1978). On the concept of available potential energy. *Quarterly Journal of the Royal Meteorological Society*, 104(441), 737-755.
- Peyrillé, P., Lafore, J.-P. et Redelsperger, J.-L. (2007). An idealized two-dimensional framework to study the West African monsoon. Part I: Validation and key controlling factors. *Journal of the Atmospheric Sciences*, 64(8), 2765-2782.
- Piersig, W. (1944). The cyclonic disturbances of the sub-tropical eastern North Atlantic. *Bull. Amer. Meteor. Soc*, 25, 2-16.
- Poan, D. E., Lafore, J. P., Roehrig, R. et Couvreux, F. (2015). Internal processes within the African Easterly Wave system. *Quarterly Journal of the Royal Meteorological Society*, 141(689), 1121-1136.
- Poan, D. E., Roehrig, R., Couvreux, F. et Lafore, J.-P. (2013). West African monsoon intraseasonal variability: A precipitable water perspective. *Journal of the Atmospheric Sciences*, 70(4), 1035-1052.
- Redelsperger, J.-L., Thorncroft, C. D., Diedhiou, A., Lebel, T., Parker, D. J. et Polcher, J. (2006). African Monsoon Multidisciplinary Analysis: An international research project and field campaign. *Bulletin of the American Meteorological Society*, 87(12), 1739-1746.
- Reed, R. J., Norquist, D. C. et Recker, E. E. (1977). The structure and properties of African wave disturbances as observed during phase III of GATE. *Monthly Weather Review*, 105(3), 317-333.
- Regula, H. (1943). Pressure changes and "tornadoes"(squalls) on the West coast of Africa. *Bulletin of the American Meteorological Society*, 24(8), 311-317.
- Rennick, M. A. (1976). The generation of African waves. *Journal of Atmospheric Sciences*, 33(10), 1955-1969.
- Roberts, A. J., Marsham, J. H. et Knippertz, P. (2015). Disagreements in low-level moisture between (re) analyses over summertime West Africa. *Monthly Weather Review*, 143(4), 1193-1211.
- Russell, J. O., Aiyer, A. et Dylan White, J. (2020). African Easterly Wave Dynamics in Convection - Permitting Simulations: Rotational Stratiform Instability as a Conceptual Model. *Journal of Advances in Modeling Earth Systems*, 12(1), e2019MS001706.

- Schwendike, J. et Jones, S. C. (2010). Convection in an African Easterly Wave over West Africa and the eastern Atlantic: A model case study of Helene (2006). *Quarterly Journal of the Royal Meteorological Society*, 136(S1), 364-396.
- Shekhar, R. et Boos, W. R. (2017). Weakening and shifting of the Saharan shallow meridional circulation during wet years of the West African monsoon. *Journal of Climate*, 30(18), 7399-7422.
- Shen, B. W., Tao, W. K. et Wu, M. L. C. (2010). African easterly waves in 30 - day high - resolution global simulations: A case study during the 2006 NAMMA period. *Geophysical Research Letters*, 37(18).
- Simmons, A. (1977). A note on the instability of the African easterly jet. *Journal of Atmospheric Sciences*, 34(10), 1670-1674.
- Smith, P. J. (1973). The kinetic energy budget over North America during a period of major cyclone development. *Tellus*, 25(5), 411-423.
- Spar, J. (1949). Energy changes in the mean atmosphere. *Journal of Atmospheric Sciences*, 6(6), 411-415.
- Sultan, B. et Janicot, S. (2000). Abrupt shift of the ITCZ over West Africa and intra - seasonal variability. *Geophysical Research Letters*, 27(20), 3353-3356.
- Sultan, B. et Janicot, S. (2003). The West African monsoon dynamics. Part II: The “preonset” and “onset” of the summer monsoon. *Journal of Climate*, 16(21), 3407-3427.
- Sultan, B., Janicot, S. et Diedhiou, A. (2003). The West African monsoon dynamics. Part I: Documentation of intraseasonal variability. *Journal of Climate*, 16(21), 3389-3406.
- Tarhule, A. (2005). Damaging rainfall and flooding: the other Sahel hazards. *Climatic change*, 72(3), 355-377.
- Taylor, K. E., Stouffer, R. J. et Meehl, G. A. (2012). An overview of CMIP5 and the experiment design. *Bulletin of the American Meteorological Society*, 93(4), 485-498.
- Thorncroft, C. et Blackburn, M. (1999). Maintenance of the African easterly jet. *Quarterly Journal of the Royal Meteorological Society*, 125(555), 763-786.
- Thorncroft, C. et Hodges, K. (2001). African easterly wave variability and its relationship to Atlantic tropical cyclone activity. *Journal of Climate*, 14(6), 1166-1179.
- Thorncroft, C. et Hoskins, B. (1994a). An idealized study of African easterly waves. I: A linear view. *Quarterly Journal of the Royal Meteorological Society*, 120(518), 953-982.
- Thorncroft, C. et Hoskins, B. (1994b). An idealized study of African easterly waves. II: A nonlinear view. *Quarterly Journal of the Royal Meteorological Society*, 120(518), 983-1015.
- Thorncroft, C. D., Hall, N. M. et Kiladis, G. N. (2008). Three-dimensional structure and dynamics of African easterly waves. Part III: Genesis. *Journal of Atmospheric Sciences*, 65(11), 3596-3607.
- Thorncroft, C. D., Nguyen, H., Zhang, C. et Peyrillé, P. (2011). Annual cycle of the West African monsoon: regional circulations and associated water vapour transport. *Quarterly Journal of the Royal Meteorological Society*, 137(654), 129-147.
- Tomassini, L., Parker, D. J., Stirling, A., Bain, C., Senior, C. et Milton, S. (2017). The interaction between moist diabatic processes and the atmospheric circulation in African easterly wave propagation. *Quarterly Journal of the Royal Meteorological Society*, 143(709), 3207-3227.
- Xue, Y., De Sales, F., Lau, W.-M., Boone, A., Feng, J., Dirmeyer, P., Guo, Z., Kim, K.-M., Kitoh, A. et Kumar, V. (2010). Intercomparison and analyses of the climatology of the West African Monsoon in the West African Monsoon Modeling and Evaluation project (WAMME) first model intercomparison experiment. *Climate Dynamics*, 35(1), 3-27.